A novel, ataxic mouse model of Ataxia Telangiectasia caused by a clinically relevant nonsense mutation

Perez, Harvey [¥1]; Abdallah, May, F.[¥1]; Chavira, Jose, I. [¥1]; Egeland, Martin, T. [1]; Vo, Karen, L. [1]; Buechsenschuetz, Callan, L. [1]; Sanghez, Valentina [1]; Kim, Jeannie, L. [1]; Pind, Molly [2], Nakamura, Kotoka [3], Hicks, Geoffrey, G. [2]; Gatti, Richard, A. [3]; Madrenas, Joaquin [1,5]; Iacovino, Michelina [1,4]; McKinnon, Peter, J. [6]; Mathews, Paul, J. [*1,7]

1. *The Lundquist Institute for Biomedical Innovation, Harbor-UCLA Medical Center, Torrance, CA*
2. *Department of Biochemistry & Medical Genetics, Max Rady College of Medicine, University of Manitoba*
3. *Department of Pathology & Laboratory Medicine, David Geffen School of Medicine, University of California, Los Angeles, CA*
4. *Department of Pediatrics, Harbor-UCLA Medical Center, Torrance, CA*
5. *Department of Medicine, Harbor-UCLA Medical Center, Torrance, CA*
6. *Center for Pediatric Neurological Disease Research, St. Jude Translational Neuroscience, St. Jude Children's Research Hospital, Memphis, TN, USA*
7. *Department of Neurology, Harbor-UCLA Medical Center, Torrance, CA*

¥Contributed equally

**Corresponding Author*

Abstract

Ataxia Telangiectasia (A-T) and ataxia with ocular apraxia type 1 (AOA1) are devastating neurological disorders caused by null mutations in the genome stability genes, A-T mutated (*ATM*) and aprataxin (*APTX*), respectively. Our mechanistic understanding and therapeutic repertoire for treating these disorders is severely lacking, in large part due to the failure of prior animal models with similar null mutations recapitulating the characteristic loss of motor coordination (i.e., ataxia) and associated cerebellar defects. By increasing genotoxic stress, through the insertion of null mutations in both the *Atm* (nonsense) and *Aptx* (knockout) genes in the same animal, we have generated a novel mouse model that for the first time progressively develops a severe ataxic phenotype associated with atrophy of the cerebellar molecular layer. We find biophysical properties of cerebellar Purkinje neurons are significantly perturbed (e.g., reduced membrane capacitance, lower action potential thresholds, etc.), while properties of synaptic inputs remain largely unchanged. These perturbations significantly alter Purkinje neuron

31 neural activity, including a progressive reduction in spontaneous action potential firing frequency that
32 correlates with both cerebellar atrophy and ataxia over the animal's first year of life. Double mutant mice
33 also exhibit a high predisposition to developing cancer (thymomas) and immune abnormalities (impaired
34 early thymocyte development and T-cell maturation), symptoms characteristic of the disorder A-T. Lastly,
35 by inserting a clinically relevant nonsense type null mutation in *Atm*, we demonstrate that small molecule
36 readthrough (SMRT) compounds can restore ATM production, indicating their potential as a future A-T
37 therapeutic.

38 1.0 Introduction

39 Ataxia Telangiectasia (A-T) is a rare (1 in ~100,000) (Swift et al. 1986), autosomal recessive genetic
40 disorder characterized by cancer predisposition, immune deficiency, and a highly penetrant progressive
41 and severe ataxia linked to cerebellar atrophy (Rothblum-Oviatt et al. 2016; Boder and Sedgwick 1958;
42 Levy and Lang 2018). A-T patients typically die in their second and third decade of life (Crawford et al.
43 2006) from lymphatic cancers, respiratory infections, or debilitating ataxia—unfortunately, survivability
44 has not dramatically changed since the 1950s (Micol et al. 2011; Rothblum-Oviatt et al. 2016). While
45 disease progression and cause of death vary widely across patients, the highly penetrant progressive
46 decline in motor coordination is reported as having the greatest negative impact on a patient's quality of
47 life (Jackson et al. 2016). Care is generally palliative, directed at reducing, limiting, or eliminating cancers
48 or infections. No long-term therapies are available for treating the ataxia and associated cerebellar
49 dysfunction and atrophy.

50 A-T is caused by deficiency or dysfunction of the ATM (A-T mutated) protein (Savitsky et al. 1995).
51 Premature termination codon (PTC) causing nonsense mutations account for up to a half of known cases
52 with missense and deletions also contributing (Concannon and Gatti 1997; Sandoval et al. 1999). ATM
53 is a serine/threonine PIKK family kinase that is an important regulator of gene stability, in particular, as a
54 regulator of the DNA damage response (DDR) to the tens of thousands of DNA lesions cells incur each
55 day (Lindahl and Barnes 2000; Kastan and Bartek 2004; Shiloh and Ziv 2013). In the active monomeric
56 form, ATM phosphorylates several key proteins halting the production of new DNA (cell cycle arrest)

57 (Ando et al. 2012), and then, depending on severity of the damage, initiating DNA repair or programmed
58 cell death (i.e., apoptosis) (Ando et al. 2012; Rashi-Elkeles et al. 2006). Several downstream DDR
59 pathway targets of ATM have been identified, including p53, CHK2, BRCA1, SMC1, and NBS1 (Matsuoka
60 et al. 2007). ATM's role in DNA repair is also implicated in normal immune system development, where
61 it is proposed to contribute to the recombination of natural DNA splicing that occurs during gene
62 rearrangement in T- and B-lymphocyte maturation (Chao, Yang, and Xu 2000; Matei, Guidos, and
63 Danska 2006; Vacchio et al. 2007; Schubert, Reichenbach, and Zielen 2002). Although its roles are still
64 emerging, ATM has also been implicated in oxidative stress homeostasis (Guo et al. 2010) and mitophagy
65 (Valentin-Vega and Kastan 2012; Pizzamiglio, Focchi, and Antonucci 2020).

66 A mechanistic understanding of why ATM deficiency causes ataxia is still under debate, but it is far from
67 the only DDR protein linked to ataxia, as aprataxin (APTX) (Aicardi et al. 1988), meiotic recombination
68 11 homolog 1 (MRE11) (Sedghi et al. 2018), nibrin (NBS1) (van der Burgt et al. 1996), senataxin (SETX)
69 (Moreira et al. 2004), and tyrosyl-DNA phosphodiesterase 1 (TDP1) (Takashima et al. 2002) when absent
70 or dysfunctional can cause cerebellar-related ataxia. This suggests that the neurological features of
71 genome instability syndromes have a common underlying cause, although this idea is still to be
72 mechanistically demonstrated (McKinnon 2009; Rass, Ahel, and West 2007).

73 A major factor limiting our ability to define why loss of DDR proteins, like ATM, selectively impacts the
74 cerebellum and causes progressive ataxia is the lack of an animal model that recapitulates these
75 neurological symptoms (Lavin 2013). Several A-T rodent models have been created over the past several
76 years by inserting gene mutations that cause protein dysfunction (lack kinase activity) or complete
77 deficiency (Herzog et al. 1998; Xu and Baltimore 1996; Elson et al. 1996; Spring et al. 2001; Campbell
78 et al. 2015; Quek et al. 2016; Tal et al. 2018; Lavin 2013); a minipig was also recently reported (Beraldi
79 et al. 2017). Unfortunately, none acquire an overt, progressive ataxia with cerebellar dysfunction and
80 atrophy that recapitulates the human disease, even though other aspects of the disorder like thyroid
81 cancers, infertility, and immune abnormalities do develop. It remains unclear why these prior animal
82 models fail to display the progressive ataxic phenotype (Lavin 2013). It is possible that species specific

83 molecular compensations in mice provide redundancies or alternative pathways minimizing the effects of
84 ATM deficiency in the brain (El-Brolosy and Stainier 2017). It is also possible that the shortened lifespan
85 of prior models (Barlow et al. 1996) is too brief for the stochastic mechanisms driving cerebellar
86 dysfunction and atrophy to accumulate and impact motor behavior. Other challenges include potentially
87 leaky genetic manipulations that result in low levels of ATM protein or active fragments with residual
88 kinase activity, thus limiting neuropathology (Li et al. 2011). The impact of missing such a crucial animal
89 model has been significant, severely limiting not only experimental studies from identifying the cellular
90 and molecular mechanisms but hampering pre-clinical development and testing of therapeutics.

91 We test here whether increasing the genotoxic stress on cells of the murine nervous system through
92 knocking out expression of ATM and an additional DDR protein leads to a more representative model of
93 A-T that displays cerebellar dysfunction, atrophy, and the development of progressive ataxia. We chose
94 to additionally knock-out APTX because its deficiency in humans causes an A-T like disorder called ataxia
95 with ocular apraxia type 1 (AOA1), but without A-T's other system defects that could increase the potential
96 for prenatal lethality or early death (e.g., immunodeficiency and cancer predisposition) (Coutinho P 2002).
97 Moreover, APTX is a phosphodiesterase involved in DNA reassembly after double and single stranded
98 repair, having a function downstream of, but not directly regulated or related to ATM (Gueven et al. 2004;
99 Schellenberg, Tumbale, and Williams 2015; Ahel et al. 2006). We therefore reasoned that deficiency of
100 both proteins would have an additive effect, increasing the amount of genotoxic stress that arises from
101 either protein alone to induce neurological dysfunction. Our results demonstrated that mice deficient in
102 ATM and APTX developed cerebellar dysfunction, atrophy, and a progressive and profound ataxia, while
103 deficiency in either protein alone did not. Additionally, double mutants acquired several additional
104 characteristic symptoms of A-T, including defects in immune maturation and a high incidence of cancer
105 (thymomas).

106 Finally, to improve the clinical and translational relevance of this new mouse model, we inserted a point
107 mutation (103C>T) in the *Atm* gene common to a large family North African A-T patients. This mutation
108 results in a premature termination codon (PTC) at what would normally be amino acid 35 resulting in loss

109 of ATM production. As a result of this genotypic mutation, we were then able to conduct proof-of-principle
110 experiments demonstrating the ability of so-called PTC readthrough therapeutics to restore production of
111 ATM protein. This includes the Small Molecule Readthrough (SMRT) compound we are developing (Du
112 et al. 2013).

113 2.0 Results

114 **2.1 Creation of a new A-T mutant mouse model expressing a clinically relevant nonsense mutation**

115 To create a more clinically relevant mouse model of A-T we used a gateway recombination cloning and
116 site-directed mutagenesis method to recapitulate a c.103C>T (p.R35X) mutation in the *ATM* gene found
117 in a large population of North African A-T patients (**Fig. 1A and Methods**) (Gilad et al. 1996). The
118 insertion of thymine in place of cytosine at this site in exon 3 results in a premature termination codon
119 (PTC) causing nonsense mutation in the ATM gene. Since the c.103C>T mutation results in different
120 PTCs in the human compared to the mouse *Atm* gene, TGA *vs.* TAG respectively, we created two
121 different mice by exchanging the mouse *Atm* exon 3 with either a human or mouse exon 3 variant with
122 the c.103C>T mutation (**Fig. 1B**). In the human variant, a 103C>T mutation of the mouse codon, where
123 the arginine (R) encoding codon (CGA) becomes a TGA stop codon, results in a mouse we denote as
124 Atm^{R35X}. In the mouse variant, the c.103C>T mutation transforms a glutamine (Q) encoding CAG codon
125 into a TAG stop codon and is denoted Atm^{Q35X}. The presence of the PTC results in a loss of ATM
126 expression, either partially in the heterozygote, or completely in the homozygote (**Fig. 1C**).

127 $Atm^{R35X/R35X}$; $Aptx^{-/-}$ mice were created by first crossing single mutant $Atm^{R35X/R35X}$ (congenic on the
128 C57BL/6J background) and $Aptx^{-/-}$ (mixed C57BL/6J and 129 background) mice to generate double
129 mutant heterozygote $Atm^{R35X/Wt}$; $Aptx^{-/+}$ mice. F1-5 littermate $Atm^{R35X/Wt}$; $Aptx^{-/+}$ mice were then crossed
130 within litters to create sufficient numbers of the desired experimental and control genotypes to determine
131 how loss of different amounts of ATM and APTX affect the animal's phenotype (**Fig. 1D**). Like prior ATM
132 deficient A-T mouse models, ATM or APTX deficiency alone did not result in mice with ataxia (**Video S1
133 and S2**). However, deficiency in both proteins ($Atm^{R35X/R35X}$; $Aptx^{-/-}$) results in the development of a severe
134 and progressively ataxic phenotype (**Fig. 1E**, **Video S3 and S4**).

135 **2.2 ATM deficient mice have lowered survivability and a high incidence of thymomas**

136 We assessed the general health and development of control and experimental mice expressing different
137 levels of ATM and APTX (**Fig. 2**). We found that *Atm*$^{R35X/R35X}$; *Aptx*$^{-/-}$ mice grew ~55% slower and reached
138 estimated plateau weights that were ~35% less than control genotypes (log-rank, $n = 21$ to 40, $p<0.0001$;
139 **Fig. 2A**). These differences in weight were a postnatal phenomenon, as no significant weight differences
140 were detected just after birth (P8) across all genotypes (1-way ANOVA, $n = 5$ to 23, $p>0.23$). Adolescent
141 double mutant mice at postnatal day 45 (P45) weighed on average 30% less in males double mutant:
142 14.4 ± 1.0 g ($n = 13$) *vs.* wildtype: 20.2 ± 0.5 g ($n = 16$), *t*-test, $p<0.0001$] and 25% less in females [double
143 mutant: 12.7 ± 0.6 g ($n = 17$) *vs.* wildtype: 17.0 ± 0.2 g ($n = 15$), *t*-test, $p<0.0001$; **Fig. 1A**]. Differences
144 across the control genotypes were observed, but they were small and not consistent across time points
145 or sex and therefore judged to not be physiologically relevant (**Fig. 2A**). Survivability of the *Atm*$^{R35X/R35X}$;
146 *Aptx*$^{-/-}$ mice was significantly reduced compared to *Atm*$^{Wt/Wt}$; *Aptx*$^{+/+}$ mice, with 53% of mice still alive at
147 400 days of age, compared to 97% of *Atm*$^{Wt/Wt}$; *Aptx*$^{+/+}$ mice at the same time point (**Fig. 2B**). ATM
148 deficiency alone was sufficient to reduce survivability, as compared to *Atm*$^{Wt/Wt}$; *Aptx*$^{+/+}$ mice, both
149 *Atm*$^{R35X/R35X}$; *Aptx*$^{+/+}$ and *Atm*$^{R35X/R35X}$; *Aptx*$^{-/+}$ mice had significantly reduced survivability rates [42%, log-
150 rank, $\chi^2_{(1, 56)} = 13.49$, $p=0.0002$ and 52%, log-rank, $\chi^2_{(1, 53)} = 19.54$, $p<0.0001$, respectively]. No significant
151 difference between ATM deficient mice with partial or complete APTX deficiency was detected [log-rank,
152 $\chi^2_{(2, 85)} = 1.01$, $p=0.6$]. Conversely, mice harboring at least one functional copy of the *Atm* gene had normal
153 survivability rates, regardless of whether they expressed APTX or not [log-rank, $\chi^2_{(3, 131)} = 3.08$, $p=0.4$].
154 No significant difference between male and female mice was observed and thus data were pooled [log-
155 rank, $p>0.4$ for all pairwise comparisons; **Fig. 2-fig. S1B**]. Generally, a third of mice with ATM deficiency
156 died from complications related to large thymic cancers (thymoma) found in the thoracic cavity (**Fig. 2C**).
157 The presence or absence of APTX did not impact cancer prevalence, and mice with at least one *Atm*
158 transcript were cancer free up until at least P400. Overall, ATM, but not APTX deficiency had severe
159 effects on the health and survivability of mice.

160 **2.3 Both ATM and APTX deficiency are necessary to produce progressive motor dysfunction**

161 The progressive development of severe ataxia is a hallmark characteristic of A-T that is recapitulated in
162 the *Atm*$^{R35X/R35X}$; *Aptx*$^{-/-}$ mice but none of the other control genotypes we tested. Overall, we find motor
163 coordination deficits emerge between 210 and 400 days after birth in *Atm*$^{R35X/R35X}$; *Aptx*$^{-/-}$ mice and find
164 no evidence of ataxia in mice with at least one copy of the *Atm* or *Aptx* gene (**Fig. 3A, B**). For the vertical
165 pole test, *Atm*$^{R35X/R35X}$; *Aptx*$^{-/-}$ mice took twice as long to descend at P400 compared to *Atm*$^{Wt/Wt}$; *Aptx*$^{+/+}$,
166 *Atm*$^{Wt/Wt}$; *Aptx*$^{-/-}$, *Atm*$^{R35X/R35X}$; *Aptx*$^{+/+}$, or *Atm*$^{Wt/R35X}$; *Aptx*$^{-/-}$ mice [Male: 29.1 ± 0.9 s (n = 3) *vs.* 7.5 ± 0.4 s
167 (n = 12), 12.5 ± 2.5 s (n = 9), 9.2 ± 0.9 s (n = 10), 8.6 ± 0.9 s (n = 11), 1-way ANOVA, $F_{(4, 40)} = 19.9$,
168 $p<0.0001$; Female: 19.0 ± 4.0 s (n = 4) *vs.* 7.5 ± 0.4 s (n = 12), 7.8 ± 0.4 s (n = 10), 10.5 ± 1.2 s (n = 6), 8.2
169 ± 0.5 s (n = 8), 1-way ANOVA, $F_{(4, 35)} = 13.9$, $p<0.0001$]. An examination of gait indicated that *Atm*$^{R35X/R35X}$;
170 *Aptx*$^{-/-}$ mice at P400, but not P210 need additional stabilization during ambulation, as they spend twice
171 as much time with 3 paws, rather than the normal 2 in contact with the ground as they walk across the
172 gait analysis platform [Male: 56.2 *vs.* 26.4 to 32.2 %, 1-way ANOVA, $F_{(4, 54)} = 14.3$, $p<0.0001$; Female:
173 58.4 *vs.* 18.9 to 28.8 %, 1-way ANOVA, $F_{(3, 178)} = 95.5$, $p<0.0001$; **Fig. 3B**]. *Atm*$^{R35X/R35X}$; *Aptx*$^{-/-}$ also display
174 a slower cadence and average speed across the platform compared to all other genotypes at P400
175 [cadence, Male: 9.5 *vs.* 13.3 to 15.9 steps/s, 1-way ANOVA, $F_{(3, 204)} = 36.8$, $p<0.0001$; Female: 9.1 *vs.* 14.2
176 to 15.9 steps/s, 1-way ANOVA, $F_{(3, 204)} = 39.7$, $p<0.0001$; speed, Male: 8.8 *vs.* 22 to 26 cm/s, 1-way
177 ANOVA, $F_{(4, 50)} = 28.3$, $p<0.0001$; Female: 58.4 *vs.* 18.9 to 28.8 cm/s, 1-way ANOVA, $F_{(3, 178)} = 39.7$,
178 $p<0.0001$; **Fig. 3B; Fig. 3-fig. S1**]. This difference in speed and cadence is unlikely due to animal size,
179 as there are no significant differences in these parameters at earlier time points when the difference in
180 size is significant (**Fig. 2A**). These observations across the two behavioral tests were found in both male
181 and female mice at each of their respective time points, consistent with the lack of sex differences
182 observed in A-T patients.

183 We further examined behavioral differences between the *Atm*$^{R35X/R35X}$; *Aptx*$^{-/-}$ and *Atm*$^{Wt/Wt}$; *Aptx*$^{+/+}$ mice
184 using a standardized set of experimental procedures used to phenotype genetically modified mice (i.e.,
185 SHIRPA; **Fig. 3C**; **Fig. 3-fig. S1**) (Rogers et al. 1997). We first detected differences in motor function at
186 P8, where *Atm*$^{R35X/R35X}$; *Aptx*$^{-/-}$ mice took 3-4 times longer on average to right themselves compared to

Atm$^{Wt/Wt}$; *Aptx*$^{+/+}$ mice [Male: 6.4 ± 1.1 s (n = 24) *vs.* 1.5 ± 0.1 s (n = 23), *t*-test, p<0.0002; Female: 11.1 ± 1.9 s (n = 21) *vs.* 2.4 ± 0.3 s (n = 17), *t*-test, p<0.0002; **Fig. 3C bottom**]. At 30-days of age, we detected significant differences between *Atm*$^{R35X/R35X}$; *Aptx*$^{-/-}$ and *Atm*$^{Wt/Wt}$; *Aptx*$^{+/+}$ mice in behavioral tests that qualitatively measure body position and spontaneous activity (**Fig. 3C**). Striking differences in *Atm*$^{R35X/R35X}$; *Aptx*$^{-/-}$ compared to *Atm*$^{Wt/Wt}$; *Aptx*$^{+/+}$ mice were observed at P400, especially for behaviors related to movement, including locomotor activity, body position, and gait (**Fig. 3C**). The results from this battery of tests demonstrates that *Atm*$^{R35X/R35X}$; *Aptx*$^{-/-}$ mice develop a severe change in behavior by P400, consistent with purely visual observations of significant motor coordination deficits in the mice up to this time point. Importantly, we do not find any significant differences between the other control genotypes, including *Atm*$^{Wt/R35X}$; *Aptx*$^{-/-}$ mice that express at least some ATM but no APTX protein (**Fig. 3-fig. S1**).

2.4 The membrane and synaptic properties are perturbed in ATM and APTX deficient neurons of the cerebellum

Purkinje neurons (PN) are a key neuronal subtype located in the cerebellar cortex. They display considerable intrinsic excitability, firing action potentials spontaneously at rates >1,000 % higher than other neurons in the brain. Their activity shapes cerebellar output via tonic inhibition of neurons of the cerebellar nuclei, which project to motor coordination centers in the forebrain, brainstem, and spinal cord. Dysfunction of cerebellar PNs is associated with several forms of ataxia and implicated in A-T (Hoxha et al. 2018; Cook, Fields, and Watt 2020; Shiloh 2020). We therefore examined if the electrophysiological properties of PNs in the *Atm*$^{R35X/R35X}$; *Aptx*$^{-/-}$ cerebellum were abnormal.

Since PN baseline activity and responsivity to input is mediated by a baseline set of passive and active membrane properties (**Fig. 4**), we directly recorded from and compared the membrane properties of PNs in acute cerebellar slices harvested from *Atm*$^{R35X/R35X}$; *Aptx*$^{-/-}$ and *Atm*$^{Wt/Wt}$; *Aptx*$^{+/+}$ mice (P350 to 400). PNs recorded from *Atm*$^{R35X/R35X}$; *Aptx*$^{-/-}$ mice had significantly "tighter" membranes, displaying higher membrane input resistances (R_m) than those from *Atm*$^{Wt/Wt}$; *Aptx*$^{+/+}$ mice [47.7 ± 5.6 (n = 15) *vs.* 30.2 ± 1.47 (n = 23) MΩ, *t*-test, p=0.008; **Fig. 4B**]. They also displayed a faster membrane time constant (τ) [3.6 ± 0.4 (n = 15) *vs.* 5.1 ± 0.3 (n = 23) ms, t-test, p=0.009; **Fig. 4B**]. These results indicate that the total

membrane capacitance ($C_m = \tau/R_m$) of the *Atm*$^{R35X/R35X}$; *Aptx*$^{-/-}$ PNs is significantly reduced [98.25 ± 19.23 (n = 15) *vs.* 175.6 ± 12.67 (n = 23) pF, *t*-test, p=0.0025; **Fig. 4B**]. At the cellular level, this suggests that the ATM and APTX deficient PNs have less (i.e., smaller in size) or thinner membranes than that of wildtype PNs; a result suggestive of a developmental deficit or neurodegenerative process (Dell'Orco et al. 2015). We next assessed the intrinsic excitability of PNs in *Atm*$^{R35X/R35X}$; *Aptx*$^{-/-}$ and *Atm*$^{Wt/Wt}$; *Aptx*$^{+/+}$ mice by examining PN action potential (AP) generation and dynamics. Significant deficits in the ability of PNs to fire continuously in response to current injection were observed in *Atm*$^{R35X/R35X}$; *Aptx*$^{-/-}$ mice (**Fig. 4C**). These deficits were associated with significant perturbations to the amplitude, threshold, and area of evoked action potentials [amplitude: 66.2 ± 0.7 (n = 14) *vs.* 72.1 ± 1.4 (n = 13) ΔmV, *t*-test, p = 0.003; threshold: -55.2 ± 1.5 *vs.* -48.61 ± 1.9 mV, *t*-test, p=0.0196; area: 17.96 ± 0.6 *vs.* 20.63 ± 1.0 mV*ms, *t*-test, p=0.048; **Fig. 4C**]. Together, these experiments demonstrate significant perturbations of PN physiological properties that likely perturb their ability to function normally in the cerebellum of *Atm*$^{R35X/R35X}$; *Aptx*$^{-/-}$ mice.

We next tested whether extrinsic and/or synaptic PN properties were also impacted in *Atm*$^{R35X/R35X}$; *Aptx*$^{-/-}$ mice. We first examined spontaneous mini excitatory post synaptic currents (mEPSC) generated by granule cell-to-PN synapses (i.e., parallel fiber inputs). No difference in mEPSC size was detected, indicating the function of granule cell axon terminals (i.e. parallel fibers) was relatively normal in the *Atm*$^{R35X/R35X}$; *Aptx*$^{-/-}$ cerebellum [18.92 ± 1.3 (n = 11) *vs.* 23.4 ± 3.3 (n = 11) pA, *t*-test, p=0.477; **Fig. 4D**] (Yamasaki, Hashimoto, and Kano 2006). mEPSC frequency however, was found to be significantly increased, a phenomenon that could be attributed to either an increase in the total number of synapses, an increase in the size of the readily releasable pool of synaptic vesicles, or an increase in the probability of neurotransmitter release in PNs of *Atm*$^{R35X/R35X}$; *Aptx*$^{-/-}$ mice [18.75 ± 2.8 Hz (n = 11) *vs.* 11.4 ± 1.0 Hz (n = 11), *t*-test, p=0.047; **Fig. 4D**]. We next explored evoked synaptic release and short-term plasticity by simultaneously recording from PNs and electrically stimulating either granule cell (i.e., parallel fibers) or inferior olivary (i.e., climbing fiber) axons with a paired-pulse burst (2-pulses, 50 ms apart). The synaptic properties of parallel fibers were found to be normal, displaying no significant differences in the expected

239 short-term facilitation (Atluri and Regehr 1996) or halfwidth and decay time constant of the evoked EPSC
240 [PPR: 1.3 ± 0.03 (n = 10) *vs.* 1.4 ± 0.05 (n = 13), *t*-test, p=0.162; halfwidth: 3.9 ± 0.6 *vs.* 4.9 ± 0.4 ms, *t*-
241 test, p=0.175; time constant: 3.5 ± 0.5 *vs.* 4.7 ± 0.4 ms, *t*-test, p=0.054; **Fig. 4E**]. In comparison, we found
242 climbing fiber-to-PN synaptic responses, which normally displays pair-pulse depression (Hansel and
243 Linden 2000), to depress at significantly greater magnitudes in *Atm*$^{R35X/R35X}$; *Aptx*$^{-/-}$ mice [PPR: 0.6 ± 0.03
244 (n = 6) *vs.* 0.7 ± 0.02 (n = 9), *t*-test, p=0.03; **Fig. 4F**]. The overall width and decay time constant of the
245 evoked currents were also smaller [halfwidth: 2.3 ± 0.6 (n = 6) *vs.* 3.0 ± 0.2 (n = 9) ms, *t*-test, p=0.004;
246 time constant (fast): 1.1 ± 0.14 *vs.* 2.9 ± 0.4 ms, t-test, p=0.001]. While these results could be caused by
247 a presynaptic deficit, such as reduced vesicle stores in the climbing fiber axon terminal, the fact that the
248 initial magnitude of the EPSC is unaffected [23.5 ± 3.6 (n = 6) *vs.* 19.1 ± 1.9 (n = 9), *t*-test, p=0.3], points
249 to a more intrinsic deficit, such as a reduced Ca^{2+} influx from the endoplasmic reticulum, which could
250 significantly impact long term synaptic plasticity critical to cerebellar function (Hoxha et al. 2018; Kano
251 and Watanabe 2017). Overall, the perturbations we observed here to the passive and active PN
252 properties likely give rise to significant cerebellar dysfunction in the *Atm*$^{R35X/R35X}$; *Aptx*$^{-/-}$ mice.

253 **2.5 ATM and APTX deficiency causes a progressive perturbation of PN neural activity that is**
254 **associated with dendritic shrinking and overall cerebellar atrophy.**

255 Decreased rates of spontaneous PN action potential firing, which can be indicative of PN dysfunction,
256 have been observed in several mouse models of ataxia, including SCAs 2, 3, 5, 6, 13, 27, several models
257 of episodic ataxia (e.g., leaner, ducky, and tottering), and autosomal-recessive spastic ataxia of the
258 Charlevoix-Saguenay ((Hourez et al. 2011; Hansen et al. 2013; Dell'Orco, Pulst, and Shakkottai 2017;
259 Kasumu and Bezprozvanny 2012; Liu et al. 2009; Perkins et al. 2010; Shakkottai et al. 2011a; Jayabal
260 et al. 2016; Stoyas et al. 2020; Hurlock, McMahon, and Joho 2008; Shakkottai et al. 2009; Bosch et al.
261 2015; Walter et al. 2006; Alviña and Khodakhah 2010; Ady et al. 2018; Larivière et al. 2019; Cook, Fields,
262 and Watt 2020). We therefore used this biomarker to characterize the progression of PN perturbation in
263 *Atm*$^{R35X/R35X}$; *Aptx*$^{-/-}$ mice and assess whether deficits were restricted to ATM and APTX deficient mice,
264 consistent with the behavioral results (**Fig. 2,3**). We additionally examined whether decreased PN activity

265 differed across the cerebellum, as anecdotal clinical pathology reports suggest degeneration may occur
266 asymmetrically across the cerebellum, with the anterior and posterior vermis and middle cerebellar
267 hemispheres affected the most, although no systematic analysis has been performed and the consistency
268 of results across patients is highly variable (Verhagen et al. 2012; De Leon, Grover, and Huff 1976;
269 Amromin, Boder, and Teplitz 1979; Monaco et al. 1988; Terplan and Krauss 1969; Strich 1966; Solitare
270 1968; Solitare and Lopez 1967; Aguilar et al. 1968a; Paula-Barbosa et al. 1983).

271 Using extracellular recording methods in the acute slice, we recorded spontaneous action potentials from
272 3,300 PNs (**Fig. 5A**), across 188 animals, encompassing *Atm*$^{R35X/R35X}$; *Aptx*$^{-/-}$ and 3 other genotypes at 4
273 different time points (P45, 120, 210, and 400). We visually selected "healthy" cells (see Methods), deeper
274 in the slice, that consistently fired during the extent of the 60 second recording period. Qualitatively, tissue
275 and cell quality did not visually differ across genotypes under DIC microscopy. Cells were sampled in a
276 distributed fashion across the lateral, intermediate and medial (vermis) cerebellum of each mouse to
277 assess whether changes in PN firing activity was ubiquitous or anatomically restricted. Regions were
278 segregated based on gross anatomical domains in the mouse defined by natural anatomical boundaries
279 (e.g., foliation) and their general connectivity with different regions of the nervous system (e.g., forebrain,
280 brainstem, etc.) (Voogd and Glickstein 1998).

281 We found that complete deficiency of both ATM and APTX, consistent with the behavioral results, was
282 necessary to produce a significantly reduced spontaneous PN firing frequency (**Fig. 5A, B)**. Although the
283 trend of slower PN firing rates was observed across most regions of the cerebellum, some subregions
284 appeared to be less or minimally impacted, including several areas of the lateral cerebellum, including
285 the paraflocculus, paramedian, and crus I and II (**Fig. 5-fig. S1**). Significant age dependent changes in
286 firing frequency were also only observed in *Atm*$^{R35X/R35X}$; *Aptx*$^{-/-}$ mice (**Fig. 5B**). The most significant
287 decline occurring between P120 and 210 [medial: 50.3 ± 2.4 Hz ($n = 61$) *vs*. 36.9 ± 2.2 Hz ($n = 31$), *t*-test,
288 $p=0.0006$]. No significant difference in PN firing frequency was detected between male and female mice
289 within each genotype, thus the data were pooled (2-way ANOVA, $p>0.3$ across all pairwise comparisons;
290 **Fig. 5-fig. S2**). Previous studies across several mouse models of heritable ataxia, including episodic

291 ataxia and several variants of spinocerebellar ataxia find that physiological disruption in PN firing not only
292 changes its frequency, but also its regularity (Kasumu and Bezprozvanny 2012; Jayabal et al. 2016;
293 Stoyas et al. 2020; Cook, Fields, and Watt 2020). We compared both the coefficient of variation (CV) and
294 variability in adjacent intervals (CV2) between *Atm*$^{R35X/R35X}$; *Aptx*$^{-/-}$ and control mice (**Fig. 5-figs. S3, S4**).
295 No difference in these parameters across sex, age, or genotype was detected. Consistent with the
296 behavioral results, cerebellar dysfunction was found only in the *Atm*$^{R35X/R35X}$; *Aptx*$^{-/-}$ mice that developed
297 ataxia and not in mice with at least some expression of ATM or APTX.

298 **2.5 ATM and APTX deficiency induces cerebellar atrophy**

299 Ataxia in A-T patients is usually detected between 1 to 2-years of age and is associated with mild to no
300 cerebellar atrophy (Tavani et al. 2003; Taylor et al. 2015). Significant structural changes are usually
301 apparent via neuroimaging between 5 to 10-years of age (Demaerel, Kendall, and Kingsley 1992; Tavani
302 et al. 2003). Comprehensive characterization of the progression of cerebellar atrophy is however severely
303 lacking in large part due challenges in imaging young patients (<2-years) and the rarity of the disorder.
304 We therefore assessed the gross developmental progression of cerebellar size and pathohistology in
305 mice deficient in both ATM and APTX that progressively develop a severe ataxia and perturbations in
306 cerebellar function. Structural changes in the overall size of the cerebellum were examined in
307 *Atm*$^{R35X/R35X}$; *Aptx*$^{-/-}$ and several different control mice over 5 time points (P45, 120, 210, 400, 460; **Fig.**
308 **5C**). Cerebellar size was defined within each animal by the ratio of 2-dimensional surface area of the
309 dorsal cerebellum to the forebrain (i.e., cerebellum area divided by forebrain area). The cerebellar size
310 of control mice slightly increased during adolescence and early adulthood (P45-P210), was generally
311 stable through adulthood (P210-400), and then declined slightly in older age (P400-460). In stark
312 contrast, relative cerebellar size in *Atm*$^{R35X/R35X}$; *Aptx*$^{-/-}$ mice progressively declined after P120. No
313 cerebellar atrophy was observed in mice with at least one copy of the *Atm* gene [i.e., *Atm*$^{Wt/R35X}$; *Aptx*$^{-/-}$;
314 1-way ANOVA, $F_{(3,44)}= 1.2$, $p=0.32$; **Fig. 5C**]. To rule out the possibility that reduced cerebellar size was
315 related to the smaller stature of *Atm*$^{R35X/R35X}$; *Aptx*$^{-/-}$ mice, we examined, but did not find a correlation
316 between animal weight and actual cerebellar size [Pearson's correlation, $p>0.3$ for all 4 genotypes at

317 P460, n = 10 to 20]. Furthermore, we found that cerebellar size did not differ between male and the on
318 average 22% smaller female mice across genotypes at this age [2-way ANOVA, $F_{(2, 153)}= 1.9$, p=0.2].
319 Therefore, cerebellar neurodegeneration in the *Atm*$^{R35X/R35X}$; *Aptx*$^{-/-}$ mice, which begins after P120, is
320 correlated with ATM and APTX deficiency.

321 In humans, cerebellar atrophy is associated with a variety of changes in the macro-structure of the
322 cerebellar cortex, this includes various reports of abnormalities in the density and distribution of granule
323 cells (GC) and PNs (Verhagen et al. 2012; De Leon, Grover, and Huff 1976; Amromin, Boder, and Teplitz
324 1979; Monaco et al. 1988; Terplan and Krauss 1969; Strich 1966; Solitare 1968; Solitare and Lopez
325 1967; Aguilar et al. 1968a; Paula-Barbosa et al. 1983; Gatti and Vinters 1985). In the *Atm*$^{R35X/R35X}$; *Aptx*$^{-}$
326 $^{/-}$ mice we do not qualitatively observe severe pathological changes in the anatomy of their cerebellum
327 (**Fig. 5-fig. S5B**). To then understand the anatomical basis of the gross atrophy, we measured the width
328 of the cortical layer of the cerebellum that contains the massive dendritic arbors of PNs called the
329 molecular layer (ML). Consistent with the temporal changes in gross cerebellar size, PN firing frequency,
330 and behavior, ML width in *Atm*$^{R35X/R35X}$; *Aptx*$^{-/-}$ mice was reduced and declined in size from P120 to P400
331 [P400: 120.2 ± 2.1 μm (n = 5) *vs.* 140.2 ± 4.8 μm (n = 5), Sidak test, p=0.0004; **Fig. 5D**]. In contrast, the
332 width of the GC layer did not change with age or differ significantly between *Atm*$^{R35X/R35X}$; *Aptx*$^{-/-}$ and
333 *Atm*$^{Wt/Wt}$; *Aptx*$^{+/+}$ mice [P400: 135.5 ± 2.4 μm (n = 6) *vs.* 127.5 ± 4.3 μm (n = 5), Sidak test, p=0.5; **Fig. 5D**].
334 These results, along with the finding that PN density did not significantly differ between *Atm*$^{R35X/R35X}$; *Aptx*$^{-}$
335 $^{/-}$ and *Atm*$^{Wt/Wt}$; *Aptx*$^{+/+}$ mice [P400: 3.9 ± 0.3 (n = 4) *vs.* 4.4 ± 0.3 (n = 5) PNs/4000 μm^2, Welch's test, p=0.3;
336 **Fig. 5-fig. S5B**] indicate that cerebellar atrophy is in large part due to a reduction in the extent of PN
337 dendrites. At the anatomical level, we were able to qualitatively observe a few other PN abnormalities.
338 This includes abnormally large diameter primary dendrites and axonal swellings in the *Atm*$^{R35X/R35X}$; *Aptx*$^{-}$
339 $^{/-}$ mice (**Fig. 5-fig. S5C**). Overall, we find a good correlation between the abnormal structural and
340 electrophysiological properties and the progression of motor behavioral deficits.

341 **2.6 Differential disruption of thymocyte development in ATM-deficient vs. APTX-deficient mice**

342 Chronic sinopulmonary infections associated with immunodeficiency are one of the leading causes of
343 death in A-T patients (Morrell, Cromartie, and Swift 1986; Bhatt and Bush 2014). Immunodeficiency is
344 linked to deficits in the generation of B- and T-lymphocytes that have been linked to defects in the antigen
345 receptor gene rearrangement processes during the generation of these cells in bone marrow and thymus,
346 respectively (Staples et al. 2008). The resulting defects in mature lymphocyte numbers include decreases
347 in $CD4^+$ helper T-cells and killer $CD8^+$ T-cells (Schubert, Reichenbach, and Zielen 2002). We therefore
348 examined the percentages of T-cells in peripheral blood and of different subpopulations in the thymus of
349 $Atm^{R35X/R35X}$; $Aptx^{-/-}$ mice using T-cell antigen receptor (TCR) and CD4/CD8 co-receptor expression.

350 In the peripheral blood, we observed a significant reduction in the total fraction of $CD3^+$ T-cells in mice
351 with reduced or absent ATM expression compared to wildtype mice (**Fig. 6**). This reduction was further
352 compounded by concomitant deficiency of APTX. ATM and APTX deficiencies reduced T-cells in
353 peripheral blood by over 65% decrease compared to wild type controls. The effect of APTX deficiency
354 was additive to that of ATM deficiency suggesting a different mechanism of action for each of these two
355 proteins on T-cell generation. The reduction in the percentage of T-cells in peripheral blood was mostly
356 associated with reduction in the CD4+ helper T-cell population (**Fig. 6B**). Of interest, the proportion of
357 CD8+ T-cells was increased only in $Atm^{R35X/R35X}$; $Aptx^{-/-}$ mice (**Fig. 6B**). Again, we observed a differential
358 effect of ATM and APTX deficiencies as seen for the effects of these mutations on the total T-cell fraction.

359 Given the reduction in T-cell populations in the blood, we next assessed T-cell development in the
360 thymus. In this organ, bone marrow-derived T-cell progenitors undergo TCR gene rearrangement
361 followed by positive selection for MHC restriction and negative selection of autoreactive clones. The
362 phases of thymocyte development can be followed by monitoring expression of CD4 and CD8 expression
363 in thymocytes. The progression of this developmental program goes from double negative ($CD4^-CD8^-$)
364 thymocytes, to double positive ($CD4^+CD8^+$) thymocytes and then to single positive ($CD4^+$ or $CD8^+$)
365 thymocytes. In addition, within the double negative stage, four different subpopulations can be identified,
366 based on expression of CD25 and CD44, known as DN1 ($CD44^+CD25^-$), DN2 ($CD44^+CD25^+$), DN3
367 ($CD25^+CD44^-$) and DN4 ($CD44^-CD25^-$) (Germain 2002).

368 Gene rearrangement during thymocyte development occurs twice, once at the double negative thymocyte
369 stage in the $CD25^+CD44^-$ stage (Krangel 2009) and then again in double positive thymocyte stage before
370 progressing into separate $CD4^+$ and $CD8^+$ single positive populations (Livák et al. 1999). ATM deficiency
371 has been linked to defects in both bouts of rearrangement in mice (Vachio 2007, Hathcock 2013).
372 Therefore, we compared the proportion of cells in the thymus expressing these different developmental
373 cell surface markers in our ATM deficient and control mice (**Fig. 7**). *Atm*$^{R35X/R35X}$*; Aptx*$^{-/-}$ and *Atm*$^{Wt/R35X}$*;*
374 *Aptx*$^{-/-}$, but not *Atm*$^{R35X/R35X}$*; Aptx*$^{+/+}$ mice had significantly elevated proportions of $CD44^+CD25^-$,
375 $CD44^+CD25^+$, and $CD44^-CD25^+$ cells compared to wildtype (**Fig. 7A**). These increased proportions
376 appear to be due in part to an impediment of $CD44^-CD25^+$ cells maturing into $CD44^-CD25^-$ double
377 negative cells, as the fraction of cells from *Atm*$^{R35X/R35X}$*; Aptx*$^{-/-}$ and *Atm*$^{Wt/R35X}$*; Aptx*$^{-/-}$ mice is significantly
378 lower than wildtype (**Fig. 7A**). Of interest, APTX deficiency by itself had the greatest effect on the loss of
379 DN4 cells suggesting that APTX deficiency, rather than ATM deficiency, is responsible for this effect. To
380 our knowledge, this finding implicates for the first time APTX in gene rearrangement during the process
381 of TCRβ recombination.

382 Next, we looked at the proportions of $CD4^+CD8^+$ thymocytes compared to $CD4^+CD8^-$ and $CD4^-CD8^+$
383 single positive thymocytes in these four different strains. In agreement with our results in the blood and
384 prior studies, we found that ATM-deficient mice but not control mice displayed decreased expression of
385 $CD4^+CD8^-$ and $CD4^-CD8^+$ single positive thymocytes (**Fig. 7B**). These results support the role of ATM in
386 TCR α/δ gene rearrangement during thymocyte development (Bredemeyer et al. 2006), a role that is
387 independent of the role played by APTX in early thymocyte maturation.

388 **2.7 Readthrough molecules overcome PTC to restore ATM expression**

389 Our primary rationale for inserting a clinically relevant nonsense mutation in the *Atm* gene was to
390 generate a mouse amenable to critical pre-clinical testing of a novel set of small molecule readthrough
391 (SMRT) compounds. We previously demonstrated SMRT compounds recover production of ATM protein
392 in A-T patient derived lymphoblastoid cell lines by overcoming premature termination codons (PTC)
393 caused by nonsense mutations (Du et al. 2013). To demonstrate suitability of this new A-T animal model

394 for SMRT compound testing we chose to directly examine their ability to restore ATM expression using
395 an explant approach that circumvents challenges related to *in vivo* delivery (e.g., bioavailability, route of
396 delivery, etc.). ATM expression was measured in samples from the spleen, where ATM is normally
397 expressed at high levels, and the cerebellum, a key target tissue for the disorder. We exposed these
398 explant tissues, harvested from both ATM^{R35X} and ATM^{Q35X} mice with either a candidate SMRT compound
399 (GJ103), or an aminoglycoside previously known to have readthrough properties (G418) for 72 hrs. and
400 then measured ATM expression by immunoblot to assess restoration. In both types of ATM deficient
401 mice, ATM expression was consistently restored in the spleen and cerebellum by both G418, GJ103 (**Fig.**
402 **8**). These results demonstrate that our SMRT compounds can enable readthrough of at least 2 of the 3
403 possible nonsense mutation causing PTCs and provide the rationale for *in vivo* efficacy testing in follow-
404 on studies.

405 3.0 Discussion

406 By increasing genotoxic stress through the addition of a secondary hit to the DDR pathway, we generated
407 a novel mouse model that displays the most comprehensive set of A-T symptoms of any model to date.
408 This includes a severe and progressive ataxia associated with cerebellar atrophy and perturbations of
409 PN properties along with a high incidence of cancer and defects in immune cell development. Together,
410 these comorbidities encompass the three leading causes of premature death in A-T — each contributing
411 to roughly a third. Of these, the incapacitating effect of ataxia is the most penetrant and is reported by
412 patients and caregivers as having the greatest impact on their quality of life. For this reason, the presence
413 of ataxia and cerebellar atrophy in this new mouse model is of great significance as it provides for the
414 very first time a resource to not only elucidate the mechanisms of neurological dysfunction, but also a
415 critically needed *in vivo* model to test severely needed A-T therapeutics like the readthrough compounds
416 we describe here.

417 We found several similarities between the overall progression of ataxia in the $Atm^{R35X/R35X}$; $Aptx^{-/-}$ mice
418 and A-T patients. In clinical A-T, motor deficits are observable by roughly 2-years of age, when parents
419 and doctors detect a lowered ability to transition from toddling to a smooth, reflexively coordinated gate—

420 unfortunately, little is known about motor defects at earlier stages due to the diseases low prevalence
421 and current lack of early diagnostic testing (Rothblum-Oviatt et al. 2016). Patients usually learn to walk
422 without assistance and neurological symptoms tend to remain stable through the first 4 to 5 years of life
423 (Rothblum-Oviatt et al. 2016). We found a similar early progression of motor deficits in *Atm*$^{R35X/R35X}$; *Aptx*$^{-}$
424 $^{/-}$ mice, detecting mild motor deficits early at P8 (righting reflex deficit), followed by a period of relative
425 stability, prior to onset of a progressive and severe ataxia developing after p210 that included changes
426 in gait, startle reflex, tremor, and locomotor activity. Several important questions arise out of these
427 findings, including whether ATM and/or APTX have a neurodevelopmental role in the cerebellum. Future
428 studies focused on the early phase of the disorder will be critical in understanding if the cerebellum
429 develops normally prior to dysfunction or whether developmental defects are an initial cause. We also
430 found, similar to A-T patients, that the severity of the late developing ataxia was variable with some mice
431 ambulating with a clumsy, high stepping rear gate (**Video S3**) and others moving almost entirely via
432 contortion of the rear trunk (**Fig. 1E** and **Video S4**) (Rothblum-Oviatt et al. 2016; Levy and Lang 2018;
433 Boder and Sedgwick 1958). Overall, we found that *Atm*$^{R35X/R35X}$; *Aptx*$^{-/-}$ mice developed a visually profound
434 and measurable progressive loss in motor coordination that was similar to that observed in A-T patients
435 and that was rescued by expression of at least one copy of the *Atm* or *Aptx* gene.

436 The loss of motor coordination in A-T has been attributed to cerebellar degeneration due to its relatively
437 selective neuropathology across the brain and its causal role in several different forms of ataxia (Hoche
438 et al. 2012). Consistent with A-T patient neuroimaging studies (Wallis et al. 2007; Sahama et al. 2015;
439 Sahama et al. 2014; Dineen et al. 2020; Tavani et al. 2003; Quarantelli et al. 2013), we find that cerebellar
440 size in *Atm*$^{R35X/R35X}$; *Aptx*$^{-/-}$ mice is initially normal, but progressively atrophies in line with changes in
441 neurological function. While loss of cerebellar tissue has been considered a main cause of ataxia in
442 humans, it is unclear from clinical data if ataxia severity is a good predictor of the extent of cerebellar
443 degeneration found postmortem (Aguilar et al. 1968b; Crawford et al. 2006; Dineen et al. 2020). In the
444 *Atm*$^{R35X/R35X}$; *Aptx*$^{-/-}$ mice, we find clear atrophy associated with thinning of the Purkinje neuron dendrite
445 layer that precedes the late, severe behavioral deficits. However, since the neuropathology observed in
446 the *Atm*$^{R35X/R35X}$; *Aptx*$^{-/-}$ mice is not severe, our findings suggest that like several SCAs (e.g.,1 AND 3),

447 changes in cerebellar function itself, rather than profound loss of cerebellar tissue, is likely sufficient to
448 cause the ataxic phenotype (Shakkottai et al. 2011b; Lorenzetti et al. 2000; Clark et al. 1997).

449 Why ATM and APTX deficiency is required to generate ataxia in mice, when loss of either is sufficient to
450 cause ataxia in humans, remains an open question. It is possible that the rodent brain may more flexibly
451 utilize compensatory pathways or redundant proteins to reduce the impact of impaired DNA repair as it
452 responds to the 10-20k DNA lesions that assault it per day (Lindahl and Barnes 2000). Several forms of
453 DNA repair exist to potentially meet this challenge, including base excision repair (BER), nucleotide
454 excision repair (NER), as well as homologous and non-homologous end joining (HEJ and NHEJ,
455 respectively), all of which ATM and APTX have been implicated in (Chou et al. 2015; Çaglayan et al.
456 2017; Wakasugi et al. 2014; Tumbale et al. 2018; Chatterjee and Walker 2017). Alternatively, it may be
457 the case that deficiency in ATM or APTX alone does not adequately impact cell health during the mouse's
458 comparatively short lifespan. The use of various DDR pathways depends on the extent and form of DNA
459 damage (e.g., radiation, genotoxic agents, metabolism, etc.), and in cases like double stranded breaks,
460 multiple pathways are necessary to fully address the damage. Thus, loss or reduced efficiency of repair
461 caused by missing DDR pathway proteins could have a graded impact on the severity and/or accrual rate
462 of deleterious damage sites. This possibility is strengthened by the fact that ATM and APTX have distinct
463 biochemical properties and functional roles in the DNA damage response, and thus deficiency in both
464 would be predicted to cause a broader hit to genome stability (i.e., increased genotoxic stress). This may
465 also account for why we find Purkinje neuron dysfunction and atrophy in 12 to 14-month-old mice, but
466 not more severe degeneration and cell death as is characteristic of human patients near their second
467 decade of life (Demaerel, Kendall, and Kingsley 1992; Tavani et al. 2003).

468 Our finding, that two genome stability pathway proteins are required to induce neurological defects in
469 mice strongly suggests that it is the loss of ATM's role in DNA repair, rather than potential functions in
470 oxidative stress signaling, mitophagy, or mitochondrial function that cause the cerebellar defects (Shiloh
471 2020). Alternatives however, cannot be completely ruled out, as APTX, like ATM has been observed
472 within the mitochondria of brain cells, where it has been proposed to be important in the processing of

473 mitochondrial DNA (Meagher and Lightowlers 2014; Sykora et al. 2011). Future experiments, enabled by
474 this new mouse model, will need to be conducted to mechanistically link ATM and ATPX deficiency
475 directly to cerebellar dysfunction.

476 We find several similarities between the biophysical and neuronal response properties of PNs in
477 *Atm*$^{R35X/R35X}$; *Aptx*$^{-/-}$ mice and other mouse models of ataxia that support a role for PN dysfunction as a
478 significant contributing factor in the ataxic phenotype. The changes in PN membrane properties we
479 observed are similar to those found in several SCA mouse models, like 1, 3, and 7 (Stoyas et al. 2020;
480 Shakkottai et al. 2011b; Dell'Orco et al. 2015). Of note, is the significant reduction in membrane
481 capacitance that is consistent with the progressive shrinking of the PN dendritic layer we observed (i.e.,
482 ML). Moreover, changes in the active PN membrane properties were found to impact action potential
483 generation and properties (e.g., threshold, width, etc.). These intrinsic changes likely underlie the
484 progressive reduction in PN action potential firing frequency that we find well correlates with the
485 development of ataxia—a common finding across several other ataxic mouse model studies, including
486 those for spinocerebellar ataxias (SCA) 1, 2, 3, 5, 6, and 13 as well as a few episodic forms (see review
487 (Cook, Fields, and Watt 2020)). While it would be tempting to design experiments to simply increase the
488 spontaneous firing rate of PNs as a solution to all ataxias, it is likely that while this phenomenon serves
489 as a biomarker for PN defects, it only superficially highlights more distinct neural signaling defects across
490 the different cerebellar ataxias. Several key questions remain to be answered for not just A-T but
491 cerebellar ataxias as a whole, including whether disease-causing cerebellar defects primarily cause
492 ataxia through a loss of cerebellar function (e.g., loss of coordinating signals during movement), or a
493 dominant negative effect (e.g., disruptive signaling that prevents the normal function of downstream
494 neural circuits). While there is no doubt that a broad therapeutic strategy to address cerebellar related
495 ataxias, it is likely that a directed approach, that addressed the genetic and molecular causes of cellular
496 function will be required to have significant therapeutic success.

497 While the link between protein deficiency and neuronal dysfunction is straightforward for some types of
498 ataxia, like the loss of voltage gated ion channels that directly shape membrane excitability in SCA6 (i.e.,

499 $Ca_{v2.1}$) (Jayabal et al. 2016), the mechanistic link between deficiency in DNA stability proteins like ATM
500 and APTX and PN dysfunction is far less obvious. Our results suggest the effects of ATM and APTX loss
501 on PNs is intrinsic, as we don't find changes in the presynaptic properties of granule cells, nor evidence
502 of cellular loss (no change in GCL thickness). Moreover, while we observed differences in short term
503 plasticity of inferior olivary inputs in ATM and APTX deficient PNs and wildtype, these results likely point
504 to a disruption in Ca^{2+} homeostasis potentially via reductions in Inositol 1,4,5-triphosphate receptor 1
505 (*Itpr1*) expression, similar to those observed in SCAs 1, 2, and 3 mouse models as well as ATM-deficient
506 mice (Kim et al. 2020; Chen et al. 2008; Liu et al. 2009; Shakkottai et al. 2011b). While this provides a
507 promising avenue for future examination and comparison, it is as of yet unclear, even for the SCAs,
508 whether changes in Ca^{2+} homeostasis is the causal factor or just another symptom or even compensatory
509 response of diseased or disturbed PNs (Dell'Orco et al. 2015).

510 In the immune system, ATM is implicated in the repair of DNA breaks that naturally occur during gene
511 rearrangement of antigen receptor genes in B- and T-cell precursors, a phenomenon critical for antigen
512 receptor (Ig and TCR) diversity of these cells. Our finding that T-cell proportions in the blood are
513 significantly reduced is consistent with prior studies in humans and A-T knockout mice (Schubert,
514 Reichenbach, and Zielen 2002; Hathcock et al. 2013; Chao, Yang, and Xu 2000; Barlow et al. 1996).
515 This reduction of T-cells in the periphery likely correlates with a defect in both cellular and humoral
516 immunity. Importantly, we found that expression of at least one copy of the ATM gene is enough to restore
517 CD4+ deficits in the blood indicating that therapies able to restore at least some ATM expression would
518 have therapeutic efficacy. Although we have not assessed B-cell development in this paper, it is likely
519 that similar conclusions would apply to that process given their mechanistic similarities (Marshall et al.
520 2018).

521 As expected, the reduction of T-cells in peripheral blood correlated with defective thymocyte
522 development. In the thymus, we found two main defects. One, induced primarily by APTX deficiency,
523 manifests as a defect in the DN3 to DN4 transition coinciding with early rearrangement of TCR β locus.
524 The other defect, primarily caused by ATM deficiency, correlates with decreased progression of double

525 positive $CD4^+CD8^+$ to single positive cells, primarily $CD4^+$ thymocytes. While the APTX finding was
526 surprising, as its deficiency (AOA 1) is not associated with immune deficits, APTX is known to interact
527 with TCR β gene rearrangement proteins, including XRCC4 (Clements et al. 2004). Future studies aimed
528 at defining APTX's role in end-joining mechanisms during TCR gene rearrangement will be important,
529 and the possibility that alternative end-joining mechanisms, like the use of microhomologies account for
530 the lack of an immune deficit in its absence need further investigation (Bogue et al. 1997).

531 The survivability of *Atm*$^{R35X/R35X}$; *Aptx*$^{-/-}$ mice is considerably longer than prior A-T mouse models. In
532 comparison, the first A-T KO mouse model reported by Barlow et al. died from thymomas usually within
533 2-4 months after birth (Barlow et al. 1996). The increased severity of cancer survivability in this, and many
534 other knockout A-T mouse models is likely genetic, as the background strain harboring the mutation has
535 been shown to have significant effects on cancer prevalence and survivability, with A/J and C57BL/6
536 backgrounds having significantly increased survivability over the BALBC and 129S strains (Genik et al.
537 2014). The fact that our ATM deficient mice were created on a C57BL/6 background likely underlies their
538 comparatively long lifespan. Given that the *Atm*$^{R35X/R35X}$; *Aptx*$^{+/+}$ mice do not develop ataxia, it is unlikely
539 that the early death in A-T KO mice prevents observation of an ataxic phenotype that would otherwise
540 develop in these mice. On the other hand, it is unknown whether the C57BL/6 background confers a
541 resilience to developing ataxia, as it does for cancer. Defining the genetic or possibly epigenetic factors
542 that influence the severity of the disease could provide avenues for future therapeutic development.

543 Given the global nature of the ATM and ATPX knockout in our mouse model, we cannot entirely rule out
544 that extra-cerebellar defects may also contribute to the severe ataxic phenotype, and thus future
545 examination outside the cerebellum, in both the forebrain, brainstem, spinal cord, and even muscle will
546 need to be conducted. Within the cerebellum, while we found some anatomical differences in the PN
547 firing properties within different regions of the cerebellum, we didn't detect anatomical differences in ML
548 width or PN density. In general, there are significant challenges in using anatomy as a grouping factor in
549 the cerebellum, as the physical folds of the tissue do not necessarily correlate well with different
550 functional, molecular expression, or biophysical property domains that have been described (Apps and

551 Hawkes 2009; Tsutsumi et al. 2015; Gao, van Beugen, and De Zeeuw 2012; Zhou et al. 2014).
552 Experiments focused on examining the extent of cerebellar defects within these domains will be important
553 in future studies and compared to the anecdotal reports of anatomical differences in A-T patients
554 (Verhagen et al. 2012; De Leon, Grover, and Huff 1976; Amromin, Boder, and Teplitz 1979; Monaco et
555 al. 1988; Terplan and Krauss 1969; Strich 1966; Solitare 1968; Solitare and Lopez 1967; Aguilar et al.
556 1968a; Paula-Barbosa et al. 1983).

557 While we detect two potential stages in the progression of ataxia in the *Atm*$^{R35X/R35X}$; *Aptx*$^{+/+}$ mice, the
558 later stage of severe ataxia develops in adulthood in mice, compared to the childhood onset in humans.
559 This may limit its use in some neurodevelopmental based studies. Also, the interpretation of future
560 experiments must carefully factor in the fact that this new model expresses null mutations in two genome
561 stability genes at the same time, a situation that has not been detected in human patients with either A-
562 T or AOA1.

563 Finally, pinpointing where, when, and how ATM deficiency causes cerebellar pathology and ataxia has
564 been a challenge as prior ATM deficient mice generally lack the characteristic features needed to causally
565 link cellular and molecular deficits to the ataxic phenotype. Multiple promising avenues of investigation
566 have been defined, including those focused at the neuronal level where ATM is implicated in oxidative
567 stress signaling (Chen et al. 2003) and synaptic function (Li et al. 2009; Vail et al. 2016), as well as glial
568 function, where recent evidence suggests glial pathology may be a leading factor in cerebellar pathology
569 (Kaminsky et al. 2016; Campbell et al. 2016; Petersen, Rimkus, and Wassarman 2012; Weyemi et al.
570 2015). This novel animal model provides a new tool to test mechanistic hypotheses regarding how ATM
571 deficiency causes cerebellar pathology and ataxia. Additionally, this model may serve most importantly
572 as a critical preclinical tool for testing both previously proposed therapeutic candidates (Browne et al.
573 2004; Chen et al. 2003) and our own SMRT compounds (Du et al. 2013). The severe limitations of not
574 having a suitable preclinical model for therapeutic testing, especially for a rare disorder like A-T and
575 AOA1, cannot be overstated.

576 # 4.0 Materials and Methods

Key Resources Table				
Reagent type (species) or resource	**Designation**	**Source or reference**	**Identifiers**	**Additional information**
Strain, strain background (*Mus musculus*)	*Atm*^{R35X}	This paper	103C>T mutation, human exon replacement	Generated by Hicks laboratory. Has been backcrossed into C57b/6 9 times. Contact pmathews@lundquist.org
Strain, strain background (*Mus musculus*)	*Atm*^{Q35X}	This paper	103C>T mutation, targeted premature termination signal in the mouse codon	Generated by Hicks laboratory. Has been backcrossed into C57b/6 9 times. Contact pmathews@lundquist.org
Strain, strain background (*Mus musculus*)	*Aptx*$^{-/-}$	Ahel et al. 2006	Aptx^{tm1Pmc}; MGI:3686875	Contact peter.mckinnon@stjude.org
gene (*Mus musculus*)	*Atm*	MGI	MGI:107202; C030026E19Rik; ENSMUSG00000034218	
gene (*Homo Sapien*)	*ATM*	OMIM	OMIM: 607585 MGI: 107202 HomoloGene: 30952; ENSG00000149311	

sequence-based reagent	Atm gene	Transnetyx	PCR primers	F-5'-CCTTTGAGGCATAAGTTGCAACTTG-3'
sequence-based reagent	Atm gene	Transnetyx	PCR primers	R- 5'-GTACAGTGTATCAGGTTAGGCATGC-3'
Chemical compound/ drugs	GJ103 Formula: c16H14N403S	TargetMol	T3448	Treatment
antibody	anti-ATM (D2E2) (Rabbit-monoclonal)	Cell signalling	Cat#: mAb-2873	IF(1:1000), WB(1:500) WB(1:1000)
antibody	anti-GAPDH (14C10) (Rabbit-monoclonal)	Cell signalling	Cat#: mAb 2118	WB(1:4000)
antibody	Anti β-Actin (D6A8) (Rabbit-monoclonal)	Cell signalling	Cat#: mAb 8457	WB(1:5000)
antibody	Anti-rabbit IgG,HRP-linked Antibody (monoclonal -polyclonal)	Cell signalling	Cat#:7074	WB(1:5000)
antibody	Calbindin D-28k	Swant	Cat# CB-38a	IF (1:1000)
antibody	Goat Anti-Rabbit488	ThermoFisher Invitrogen	Cat# A11034	IF(1:1000)
antibody	Fluoromount -G with DAPI	Southern Biotech	Cat# 0100-20	

antibody	CD4	ThermoFisher Invitrogen	Cat# 50-0041-82	FACS (5 ul per test)
antibody	CD8	ThermoFisher Invitrogen	Cat# 53-0081-82)	FACS (5 ul per test)
antibody	CD3	ThermoFisher Invitrogen	Cat#12-0031-83	FACS (5 ul per test)
antibody	CD44	ThermoFisher Invitrogen	Cat# 25-0441-82	FACS (5 ul per test)
antibody	CD25	ThermoFisher Invitrogen	Cat# 47-0251- 82	FACS (5 ul per test)
commercial assay or kit	BCA Protein Assay Kit	ThermoFisher Pierce	Cat# 23225	Protein Assay
commercial assay or kit	SuperSignal West Pico Chemilumine scent Substrate	ThermoFisher Pierce	Cat# 34580	Chemilumine scent Substrate
commercial assay or kit	Radiance plus	Azure Biosystems	Cat# AC2103	Chemilumine scent Substrate
Software	FlowJo	https://www.flowjo.com/solutions/flowjo	RRID:SCR_008520	
Software	ImageJ software	ImageJ (http://imagej.nih.gov/ij/)	RRID:SCR_003070	
Software	IgorPro	http://www.wavemetrics.com/products/igorpro/igorpro.htm	RRID:SCR_000325	Version 7; Tarotools procedures
Software	Neuroexpress	https://www.researchgate.net/project/NeuroExpress-	https://www.researchgate.net/project/NeuroExpress-	Version 21.1.13; Used for

		Analysis-software-for-whole-cell-electrophysiological-data	Analysis-software-for-whole-cell-electrophysiological-data	mEPSC analyses
Software	GraphPad, Prism	GraphPad Prism (https://graphpad.com)	RRID:SCR_015807	Versions 8 and 9
Software	MBF, Stereo investigator	https://www.mbfbioscience.com/stereology	RRID:SCR_017667	Version 2021
Software	Microsoft Excel	https://www.microsoft.com/en-us/microsoft-365/excel	Mircosoft 365	
Software	Catwalk XT	https://www.noldus.com/applications/rodent-gait-analysis	N/A	Catwalk XT v10.6

577

578 **4.1 Ethics Statement**

579 This study was performed in strict accordance with the recommendations in the Guide for the Care and
580 Use of Laboratory Animals of the National Institutes of Health. All the animals were handled according to
581 approved institutional animal care and use committee (IACUC) protocols at The Lundquist Institute
582 (31374-03, 31773-02) and UCLA (ARC-2007-082, ARC-2013-068). The protocol was approved by the
583 Committee on the Ethics of Animal Experiments of the Lundquist Institute (Assurance Number: D16-
584 00213). Every effort was made to minimize pain and suffering by providing support when necessary and
585 choosing ethical endpoints.

586 **4.2 Mice**

587 All mice were group housed and kept under a 12-h day/night cycle with food and water available *ad libitum*.
588 Animals were housed within the general mouse house population, and not in specialized pathogen free
589 rooms. Older animals were made available wetted food or food gel packs on the ground of the cages as

590 ataxia developed. *Atm*^{R35X} and *Atm*^{Q35X} mice were created and provided by Dr. Hicks and colleagues at
591 the University of Manitoba.

592 These mice were created to contain the c.103C>T mutation found in a large population of North African
593 AT patients, using recombineering Gateway technology and site-directed mutagenesis. A C>T mutation
594 at this position in the mouse *Atm* gene creates a TAG G stop codon. The same mutation in the human
595 ATM gene produces a TGA G stop codon. In consideration of the use of these models for therapeutic
596 interventions, we chose to create a mouse model for each of the two PTC codons (**Fig. 1A**).

597 A modified Gateway R3-R4-destination vector was used to pull out the desired region of the mouse Atm
598 gene from a Bacterial Artificial Chromosome (BAC) and subsequently mutated to create either a TAG G
599 stop codon at codon 35 (M00001, position 103 (C>T)) or a TGA G stop codon (M00002, position 103
600 (CAG>TGA), replicating the human AT PTC). The genomic alleles were then cloned into a modified
601 version of the NorCOMM mammalian targeting vector using a 3-way Gateway Reaction (Bradley et al.
602 2012). The resulting targeting vectors were electroporated into C2 ES cells (C57Bl/6N, derived in A. Nagy
603 lab, Toronto, Canada) and successfully targeted clones were identified by selection with G418
604 (Gertsenstein et al. 2010). Integration of the mutated targeting cassette into the *Atm* gene locus was
605 confirmed by Southern blot, and by sequencing of PCR products to confirm the presence of the Atm PTC
606 mutation, error free targeting into the Atm locus and error free functional components of the vector (data
607 not shown). Positive ES clones were used for blastocyst injection to obtain the transgenic lines. The
608 transgenic allele contained a floxed human beta actin promoter - delta TK1- Neo cassette in the intron
609 upstream of the region containing the mutated exon. This floxed cassette was subsequently excised by
610 crossing with a Cre driver mouse (B6.C-Tg(CMV-cre)1Cgn/J) to generate *Atm*$^{R35X/Wt}$ and *Atm*$^{Q35X/Wt}$ (MGI
611 nomenclature: Atm$^{TM1(103CAG>TGA)MFGC}$ and Atm$^{TM1(103C>T)MFGC}$, respectively) mouse lines (**Fig. 1A**).
612 Genotyping of the two *Atm* lines was performed by using the following primers at Tm 62°C: Atm gene
613 forward (F) primer: 5'-CCTTTGAGGCATAAGTTGCAACTTG-3'; and Atm gene reverse (R) primer: 5'-
614 GTACAGTGTATCAGGTTAGGCATGC-3', creating a Wild-type allele product of 151bp or targeted allele
615 product of 241bp (**Figs. 1A, 1B**).

616 *Atm*^{R35X} and *Atm*^{Q35X} were backcrossed with C57Bl/6J mice for 9 generations (99.2% isogenic) prior to
617 cryopreservation and subsequent rederivation using C57Bl/6J surrogate mothers. *Atm*^{R35X} and *Atm*^{Q35X}
618 breeders were obtained from F1 sibling *Atm*$^{R35X/Wt}$ and *Atm*$^{Q35X/Wt}$ mice. *Atm*$^{R35X/R35X}$ and *Atm*$^{Q35X/Q35X}$ were
619 both found to be fertile. *Aptx* knockout (*Aptx*$^{-/-}$) mice were created and provided to Dr. Mathews as
620 embryos from Dr. McKinnon (Ahel et al. 2006), and subsequently rederived via C57Bl/6J surrogate
621 mothers. *Aptx*$^{-/-}$ mice are on a C57Bl/6 and 129 mixed background. *Atm*$^{R35/R35XX}$; *Aptx*$^{-/-}$ mice of various
622 Wt, heterozygous, and homozygous combinations were created from *Atm*$^{R35X/Wt}$; *Aptx*$^{-/+}$ breeders
623 generated by crossing *Atm*$^{R35X/R35X}$ and *Aptx*$^{-/-}$ mice. One cohort of double mutant and corresponding
624 control mice were used in the longitudinal behavioral study for gait analyses and SHIRPA testing (**Figs.**
625 **2**, **3**). Multiple additional cohorts of age matched double mutant and control mice were used for
626 electrophysiological, immunohistological, and Vertical Pole test experiments (**Figs. 4**, **7**). Immunological
627 and protein expression experiments were carried out using mice bred from the original *Atm*^{R35X} and
628 *Atm*^{Q35X} rederived mice (**Figs**. **5**, **6**, and **8**).

629 Genotyping was performed from ear tissue samples of P8-11 mice. Real-time PCR methods conducted
630 by Transnetyx Inc. were used to determine each animals' genotype. Animals were made identifiable via
631 toe tattoos given at the same time as ear biopsy. Unique primers for *Atm*^{R35X} and *Atm*^{Q35X} were quantified
632 and used to identify Wt, hetero- and homo-zygous mice (listed above). *Aptx*$^{-/-}$ and *Aptx*$^{Wt/Wt}$ primers were
633 used to assess their genotypes.

634 **4.3 Animal Health**

635 Animals were weighed via a digital scale at P8, 45, 120, 210, 400. Animal death was recorded as the day
636 found dead, or on the day of euthanization when the animals reached a humane endpoint (animal unable
637 to right itself within 60s, significant hair matting indicating lack of self-grooming, or excessive distress as
638 noted by the veterinary staff). Animal carcasses were immediately frozen upon death, and postmortem
639 necropsies were carried out in batch. Probable cause of death was determined to the best of our ability
640 in collaboration with the staff veterinarian (Dr. Catalina Guerra) by visual inspection of the internal organs.
641 Some mice were cannibalized or accidentally disposed of by vivarium staff and were therefore labelled

642 as “missing.” Mice with no discernable visual cause of death were labelled “indeterminable.” Mice that
643 were found with thoracic masses near where the thymus would normally be in young mice were listed as
644 “thymic cancer.” All other identified probable causes of death (e.g., enlarged livers, urinary blockage)
645 were labelled “other.”

646 **4.4 Behavior**

647 Before performing any behavioral test, mice were acclimated to the behavioral suite for ~20-minutes.
648 Mice were tested at varying times of the day, in line with their day cycle. A battery of behavioral tests was
649 performed on naïve double mutant mice of the indicated genotypes at various time points depending on
650 the behavior but in the same cohort of mice. The battery of tests included Catwalk Gait assessment (P45,
651 120, 210, 400) and a subset of the SmithKline-Beecham Harwell Imperial-College and Royal-London-
652 Hospital Phenotype Assessment (SHIRPA) tests (P30 and 400). These tests were conducted by the
653 UCLA Behavioral Core. Double mutant and control mice were additionally examined on the Vertical Pole
654 test. All behavioral apparatus was wiped down with ethanol (70%) between each testing each subject.

655 <u>Gait Analysis</u>

656 We used a Noldus Catwalk Gait analysis system designed to semi-automatically measure and analyze
657 the gait of mice during normal ambulation. Briefly, the movement of mice across a glass bottom corridor
658 is video recorded from a ventral position. Paw prints are highlighted in the video due to light illumination
659 across the glass walking platform. Each mouse step within a video is subsequently detected using
660 Catwalk XT (Noldus) in a semi-automated fashion. A run for each mouse consists of 3 trials of consistent
661 ambulation across the monitored platform. Only consistent trials are accepted, and mice may take up to
662 10 attempts to complete 3 compliant trials in either direction across the corridor. Compliant trials were
663 defined as those with movement across the platform under 5 s-long and with no more than 60% speed
664 variation. Once placed onto the platform, mice generally ran back and forth without any need for
665 experimenter prompting.

666 <u>Vertical Pole</u>

Mice are placed at the top of an 80 cm tall bolt with their nose faced down and hind paws as close to the top as possible. Mice are immediately released, and time started immediately upon placement. Time is stopped when the first forepaw touches the surface below the pole. A mouse's natural predilection is to immediately climb down the pole, and they are given up to 60 s to traverse the pole, otherwise they are helped off the pole. A non-completed trial is automatically given a time of 30 s, as 95% of mice that did not descend within 30 s were still on the pole at the 60 s mark.

<u>SHIRPA</u>

Behavioral tests were conducted by the University of California, Los Angeles Behavioral Core at P30 and P400. All parameters are scored to provide a quantitative assessment, which enables comparison of results both over time and between different laboratories. Each mouse was sequentially tested across all behaviors within ~20-min time span before moving onto the next mouse. The experimenter was blinded to animal genotype. The screen was performed as described previously (Rogers et al. 1997).

Behavioral Observation

The primary screen provides a behavioral observation profile and assessment of each animal begins by observing undisturbed behavior in a viewing jar (10 cm diameter) for 5-min In addition to the scored behaviors of **body position**, **spontaneous activity**, **respiration rate**, and **tremor**, the observer logs any instances of bizarre or stereotyped behavior and convulsions, compulsive licking, self-destructive biting, retropulsion (walking backwards) and indications of spatial disorientation.

Arena Behavior

Thereafter, the mouse is transferred to the arena (30 cm x 50 cm) for testing of transfer arousal and observation of normal behavior. The arena is marked into a grid of 10 cm^2 squares to measure locomotor activity within a 30 s-period. While the mouse is active in the arena, measures of **startle response**, **gait**, **pelvic elevation**, and **tail elevation** are recorded.

Supine Restraint

The animal is restrained in a supine position to record autonomic behaviors. During this assessment, **grip strength**, **body tone**, **pinna reflex**, **corneal reflex**, **toe pinch**, **wire maneuver**, and **heart rate**, were evaluated.

Balance and Orientation

Finally, several measures of vestibular system function were performed. The **righting reflex**, **contact righting reflex**, and **negative geotaxis** tests were performed. Throughout this procedure vocalization, urination and general fear, irritability, or aggression were recorded.

Equipment Used

1. Clear Plexiglas arena (approximate internal dimensions 55 x 33 x18 cm). On the floor of the arena is a Plexiglas sheet marked with 15 squares (11 cm). A rigid horizontal wire (3 mm diameter) is secured across the rear right corner such that the animals cannot touch the sides during the wire maneuver. A grid (40 x 20 cm) with 12 mm mesh (approximate) is secured across the width of the box for measuring tail suspension and grip strength behavior.
2. A clear Plexiglas cylinder (15 x 11 cm) was used as a viewing jar.
3. One grid floor (40 x 20 cm) with 12 mm meshes on which viewing jars stand.
4. Four cylindrical stainless-steel supports (3 cm high x 2.5 cm diameter) to raise grids off the bench.
5. One square (13 cm) stainless steel plate for transfer of animals to the arena.
6. Cut lengths of 3 / 0 Mersilk held in the forceps for corneal and pinna reflex tests
7. A plastic dowel rod sharpened to a pencil point to test salivation and biting.
8. A pair of dissecting equipment forceps, curved with fine points (125 mm forceps, Philip Harris Scientific, Cat. No. D46-174), for the toe pinch.
9. A stopwatch.
10. An IHR Click box is used for testing the startle responses. The Click Box generates a brief 20 KHz tone at 90dB SPL when held 30cm above the mouse. Contact Prof. K.P. Steel, MRC Institute of Hearing Research, University Park, Nottingham NG7 2RD.
11. A ruler.

12. A 30 cm clear Plexiglas tube with an internal diameter of 2.5 cm for the contact righting reflex.

4.5 Electrophysiology

Preparation of acute cerebellar slices

Acute parasagittal slices of 300 μm thickness were prepared from the cerebellum of experimental and control littermate mice by following published methods (Hansen et al., 2013). In brief, cerebella were quickly removed and immersed in an ice-cold extracellular solution with composition of (mM): 119 NaCl, 26 $NaHCO_3$, 11 glucose, 2.5 KCl, 2.5 $CaCl_2$, 1.3 $MgCl_2$ and 1 NaH_2PO_4, pH 7.4 when gassed with 5% CO_2/95% O_2. Cerebella were sectioned parasagittally using a vibratome (Leica VT-1000, Leica Biosystems, Nussloch, Germany) and initially incubated at 35°C for ~30 min, and then equilibrated and stored at room temperature until use.

Extracellular Electrophysiology

Extracellular and intracellular recordings were obtained from Purkinje neurons (PNs) in slices constantly perfused with carbogen-bubbled extracellular solution and maintained at either 37° C (extracellular) or 32° C (intracellular) ± 1° C (see above). Cells were visualized with DIC optics and a water-immersion 40× objective (NA 0.75) using a Zeiss Examiner microscope. Glass pipettes of ~3 MΩ resistance (Model P-1000, Sutter instruments, Novato, CA) were filled with either extracellular solution and positioned near PN axon hillocks in order to measure action potential-associated capacitive current transients in voltage clamp mode with the pipette potential held at 0 mV. For whole-cell patch clamp recordings, pipettes were filled with an intracellular solution (mM): 140 KMeth (CH3KO3S), 10 NaCl, 2 $MgCl_2$, 0.2 $CaCl_2$, 10 HEPES, 14 Phosphocreatine (tris salt), 1 EGTA, 4 Mg-ATP, 0.4 Na-GTP. 100 μM Picrotoxin (Sigma) was added to block inhibitory GABAegeric synaptic inputs. Data was acquired using a MultiClamp 700B amplifier at 20 or 100 kHz in voltage or current clamp mode, Digidata 1440 with pClamp10 (Molecular Devices, Sunnyvale, CA) and filtered at 2 to 4 kHz. The series resistance was usually between 10 and 15 MΩ. Series resistance was compensated at 80% for short term plasticity experiments only.

For extracellular recordings, a total of 20 to 45 PNs were recorded from for each animal across all genotypes, sexes, and age groups. Recordings were distributed across both the medial-lateral and

743 rostro-caudal axis of the cerebellum. Only cells with a "healthy" look (low contrast of cellular borders),
744 and regular, uninterrupted firing rate were examined. During analysis, a few cells were found to have
745 gaps in firing of greater than 2 second and these cells were eliminated from analysis, as this type of firing
746 is associated with being "unhealthy." Double mutant tissue did not qualitatively differ in appearance under
747 DIC microscopy prior to recordings, nor was the number of "unhealthy" cells greater than that of other
748 genotypes (7% vs 4 to 11% of all cells across control genotypes at P400). Spatial comparison of neural
749 activity was obtained by recording from serial sections in the flocculus, lateral (2nd or 3rd), intermediate
750 (6th or 7th), and medial (11th or 12th) slices. Lower number slices were used in the younger age groups
751 (P45 and 110) to roughly match the relative positioning of recordings across age groups. 0-3 recordings
752 were made from each lobule within each slice dependent on tissue quality and health. Each recording
753 lasted for 1-minute. 3 to 5 mice were used for each age group and the experimenter was blinded to the
754 genotype, age, and sex.

755 Intracellular recordings were obtained from PNs in either folia III or VIII of the vermis, no statistical
756 differences in properties were observed between folia.

757 <u>Analyses</u>

758 Spontaneous action potential interstimulus intervals detected and analyzed using standard and custom
759 routines in ClampFit (Molecular Device), IgorPro (Wavemetrics), and Excel (Microsoft). Specifically,
760 action potentials were threshold detected and spiking statistics (i.e., frequency and interval length),
761 determined using adapted IgorPro routines (Taro Tools; https://sites.google.com/site/tarotoolsregister/).
762 The coefficient of variation of the mean inter-spike interval (CV) and the median inter-spike interval
763 ($CV2=2\ |ISIn+1-ISIn|/(ISIn+1+ISIn)$) were calculated in Excel using custom macros.

764 Standard membrane properties were analyzed using IgorPro. R_M was determined by averaging 3 voltage
765 trace responses to a -5 mV step pulse from a -80 mV holding potential and measuring the resulting
766 current deflection between 900 and 1000 ms after onset. The membrane time constant was measured
767 by fitting a single exponential to the initial decay phase from 90 to 10% of the peak. C_M was calculated
768 by dividing the membrane time constant by the R_M. mEPSC events were recorded over a 1-minute epoch

769 and detected and measured using Neuroexpress (v21.1.13). Parallel and climbing fiber axons were
770 stimulated using theta-glass electrodes (W.P.I.) and a TTL controlled stimulus isolator (ISO-Flex,
771 A.M.P.I.). Evoked EPSC amplitudes and decay time constants (1 exp. for parallel and 2 exp. for climbing
772 fibers) were analyzed using custom routines in IgorPro. Action potentials were examined as part of a set
773 of 1 s current injections between -500 and 2250 pA (250 pA steps) with a holding current adjusted to
774 maintain an ~70 mV potential. Action potential waveforms were measured using custom routines in
775 IgorPro. Action potential threshold was defined as the first membrane voltage in which the first derivative
776 exceeded 30 mV/ms (Zhu et al. 2006).

777 **4.6 Examination of Cerebellar Atrophy**

778 Cerebellar size

779 Immediately after brain removal from the skull, a dorsal, whole mount image was obtained. Images were
780 then processed using Fiji (NIH). The forebrain and cerebellar sizes were assessed by outlining their 2-
781 dimensional space and then calculating area. We normalized for possible differences in overall brain size
782 by dividing the results of the cerebellum by forebrain size to produce a relative cerebellum to forebrain
783 ratio. Experimenters were blind to the genotype of the animal.

784 Immunohistochemistry

785 At the respective study endpoints (P45, 120, 210, 400), male and female mice of all genotypes
786 represented in this study were anesthetized with isoflurane and underwent transcardial perfusion with
787 phosphate-buffered saline followed by 4% (w/v) buffered paraformaldehyde (PFA) and then dissected
788 to extract the brain. Images of the whole brain were taken immediately after removing the brain from
789 the skull and the brains were then submerged in 4% PFA for 24-hours, followed by 72-hours in 30%
790 sucrose in Tris-buffered saline (TBS) with 0.05% azide, and then cryoprotected in TBS-AF and stored
791 at 4°C until further use. The cerebellum was separated from the forebrain and parasagittally sectioned
792 using a sliding microtome (Microm HM 430, Thermo Scientific) set to section at 40 μm thickness.
793 Cerebellum sections were collected in a series of six and stored in TBS-AF at 4° C until further use. For
794 immunofluorescent visualization of Purkinje neurons, cerebellum sections of both *Atm*$^{Wt/Wt}$; *Aptx*$^{+/+}$ and

795 *Atm*$^{R35X/R35X}$; *Aptx*$^{-/-}$ (n = 5 per genotype) were washed for 5 min in TBS three times, and then blocked in
796 15% normal goat serum at room temperature for 30 min followed by free floating incubation in rabbit
797 anti-calbindin D-28k (1:1000) for 1 hour at room temperature on an orbital shaker, then washed for 5
798 min with TBS three times, followed by free floating incubation in goat anti-rabbit Alexa Fluor 488
799 (1:1000) for 1 h in the dark at room temperature on an orbital shaker. Following secondary antibody
800 incubation, sections were washed for 5 min in TBS three times and stored in TBS until further use.
801 Sections were mounted and cover-slipped with Fluoromount-G with DAPI. Slides were scanned using
802 Stereo Investigator version 2020.1.3 64bit (MBF Bioscience) on a Zeiss Axio Imager.M2 microscope
803 (Carl Zeiss Microscopy) using a 20x objective (NA 0.5) and images captured with a Hamamatsu ORCA
804 Flash 4.0 LT C11440 digital camera (Hamamatsu Photonics). To quantify the number of calbindin-
805 reactive cells in each folia in the resulting images, we randomly drew 2 lines between 300 to 500 μm
806 long in each folia and manually counted the total number of PNs along the length within the 40 μm
807 thickness of the tissue slice. 2D density (# of PNs/(linear length * 40 um thickness)) of the two samples
808 per folia were then averaged for further between folia and subject comparison. Experimenter was
809 blinded to mouse genotype.

810 Molecular (Calbindin) and granule cell (DAPI) layer widths were assessed by taking two width
811 measurements at two predefined locations for each folia, roughly halfway along the long extent of each
812 folia. Experimenter was blinded to the mouse genotype in which slices were examined and the order of
813 examination was interleaved.

814 **4.7 Flow Cytometry Measurements**

815 Flow cytometry analysis of blood and thymus cells was performed by staining with specific anti-mouse
816 antibodies: CD4, CD8, CD3, CD44, and CD25. Briefly, whole-blood samples (50 μl) were stained using
817 fluorescent-labeled antibodies, then red-blood cells were lysed using BD lysing solution while live white-
818 blood cells were stained using a viability stain. Thymi were mechanically dissociated. 1 to 2 million
819 thymus cells were similarly stained using specific antibodies for CD4, CD8, CD44 and CD25. Analysis of

820 immuno-stained white blood cells or thymus samples was performed using FACS ARIA III and data
821 analyzed using FlowJo software as reported previously (Sanghez et al. 2017).

822 **4.8 Western Blots**

823 Protein extracts (cells/tissues) were homogenized in radioimmunoprecipitation assay (RIPA) lysis buffer
824 (150 mM NaCl, 1% Nonidet P-40 [NP-40], 0.5% deoxycholate, 0.1% SDS, 50 mM Tris, pH 8.0) with
825 protease inhibitors (10 ug/ml AEBSF, 10 ug/ml leupeptin, 5 ug/ml pepstatin, 5 ug/ml chymotrypsin, 10
826 ug/ml aprotinin). The protein extracts were sonicated then pelleted by centrifugation at 13,000 rpm for 15
827 min at 4°C. BCA protein assay was used to quantify protein concentrations. Samples containing equal
828 amounts of protein 50 to 100 μg per lane were separated using 4 to 12% gradient TGX precast gels
829 BioRad then transferred by TransBlot Semi-Dry BioRad system using Nitrocellulose transfer pack.
830 Transferred blots were stained by Ponceau S stain for equal protein loading then washed and blocked
831 with 5% nonfat dry milk in TBST for 60 min at room temp. Primary antibodies were incubated with shaking
832 overnight at 4°C. Blots were probed for the following antibodies: ATM (D2E2) Rabbit mAb Cell Signaling,
833 at 1:1000 dilution, β-Actin (D6A8) Rabbit mAb Cell Signaling, GAPDH (D16H11) Rabbit mAb Cell
834 Signaling followed by the appropriate horseradish peroxidase–conjugated (HRP) secondary Anti-rabbit,
835 Anti-mouse for 2 hours at room temperature. After multiple washes with TBST, Protein expression was
836 detected by Radiance Plus chemiluminescence substrate using the Azure c400 and the BioRad
837 ChemiDoc imaging systems. Densitometric analysis of the ATM was performed using ImageJ.
838 Experiments were performed with 2 technical and 2-3 biological replicates as indicated.

839 **4.9 Statistical Assessment**

840 The number of animals chosen for each group was based on a priori power analyses using GPower v3.1
841 based on an α size of 0.5, power of 0.8, and effect sizes estimated from preliminary data or prior studies.
842 We used both parametric (1- and 2-way ANOVA) for normally distributed and non-parametric (Kruskal
843 Wallace) statistical methods for interval data to test for differences between groups followed by pairwise
844 multiple comparisons tests as indicated in the text. Outliers for immune data in Figs. 6 and 7 were

excluded via the ROUT method (Q=2%). The specific analyses used for each data set is noted in each figure legend. For all figures: * $p \leq 0.05$, ** $p<0.01$, *** $p<0.001$, **** $p<0.0001$. Data are reported as mean ± SEM and box and whisker plots indicate the minimum, first quartile, median, third quartile, and maximum data values. All figures and statistical analyses were completed using Excel (Microsoft 360) or Prism v8 and 9 (Graphpad).

5.0 Acknowledgements

We would like to thank the UCLA Behavioral Core, especially Irina Zhuravka for her efforts assaying behavioral deficits in the mice. We would also like to thank Dr. Jennifer Fogel for comments and edits to the manuscript.

6.0 Competing interests

The authors declare that no competing interests exist.

7.0 Citations

Ady, Visou, Brenda Toscano-Márquez, Moushumi Nath, Philip K Chang, Jeanette Hui, Anna Cook, François Charron, Roxanne Larivière, Bernard Brais, and R Anne McKinney. 2018. 'Altered synaptic and firing properties of cerebellar Purkinje cells in a mouse model of ARSACS', *The Journal of physiology*, 596: 4253-67.

Aguilar, M. J., S. Kamoshita, B. H. Landing, E. Boder, and R. P. Sedgwick. 1968a. 'Pathological observations in ataxia-telangiectasia. A report of five cases', *Journal of Neuropathology and Experimental Neurology*, 27: 659-76.

Aguilar, Mary Jane, Shigehiko Kamoshita, Benjamin H. Landing, Elena Boder, and Robert P. Sedgwick. 1968b. 'Pathological Observations in Ataxia-Telangiectasia: A Report on Five Cases*', *Journal of Neuropathology and Experimental Neurology*, 27: 659-76.

Ahel, I., U. Rass, S. F. El-Khamisy, S. Katyal, P. M. Clements, P. J. McKinnon, K. W. Caldecott, and S. C. West. 2006. 'The neurodegenerative disease protein aprataxin resolves abortive DNA ligation intermediates', *Nature*, 443: 713-6.

Aicardi, J., C. Barbosa, E. Andermann, F. Andermann, R. Morcos, Q. Ghanem, Y. Fukuyama, Y. Awaya, and P. Moe. 1988. 'Ataxia-ocular motor apraxia: a syndrome mimicking ataxia-telangiectasia', *Annals of Neurology*, 24: 497-502.

Alviña, Karina, and Kamran Khodakhah. 2010. 'KCa channels as therapeutic targets in episodic ataxia type-2', *Journal of Neuroscience*, 30: 7249-57.

Amromin, George D, Elena Boder, and Raymond Teplitz. 1979. 'Ataxia-telangiectasia with a 32 year survival: a clinicopathological report', *Journal of Neuropathology and Experimental Neurology*, 38: 621-43.

878 Ando, K., J. L. Kernan, P. H. Liu, T. Sanda, E. Logette, J. Tschopp, A. T. Look, J. Wang, L. Bouchier-
879 Hayes, and S. Sidi. 2012. 'PIDD death-domain phosphorylation by ATM controls prodeath versus
880 prosurvival PIDDosome signaling', *Molecular Cell*, 47: 681-93.
881 Apps, R., and R. Hawkes. 2009. 'Cerebellar cortical organization: a one-map hypothesis', *Nature*
882 *Reviews: Neuroscience*, 10: 670-81.
883 Atluri, Pradeep P., and Wade G. Regehr. 1996. 'Determinants of the Time Course of Facilitation at the
884 Granule Cell to Purkinje Cell Synapse', *The Journal of Neuroscience*, 16: 5661-71.
885 Barlow, C., S. Hirotsune, R. Paylor, M. Liyanage, M. Eckhaus, F. Collins, Y. Shiloh, J. N. Crawley, T.
886 Ried, D. Tagle, and A. Wynshaw-Boris. 1996. 'Atm-deficient mice: a paradigm of ataxia
887 telangiectasia', *Cell*, 86: 159-71.
888 Beraldi, R., D. K. Meyerholz, A. Savinov, A. D. Kovacs, J. M. Weimer, J. A. Dykstra, R. D. Geraets, and
889 D. A. Pearce. 2017. 'Genetic ataxia telangiectasia porcine model phenocopies the multisystemic
890 features of the human disease', *Biochim Biophys Acta Mol Basis Dis*, 1863: 2862-70.
891 Bhatt, Jayesh M., and Andrew Bush. 2014. 'Microbiological surveillance in lung disease in ataxia
892 telangiectasia', *European Respiratory Journal*, 43: 1797-801.
893 Boder, Elena, and Robert P. Sedgwick. 1958. 'ATAXIA-TELANGIECTASIA', *A Familial Syndrome of*
894 *Progressive Cerebellar Ataxia, Oculocutaneous Telangiectasia and Frequent Pulmonary*
895 *Infection*, 21: 526-54.
896 Bogue, M. A., C. Wang, C. Zhu, and D. B. Roth. 1997. 'V(D)J recombination in Ku86-deficient mice:
897 distinct effects on coding, signal, and hybrid joint formation', *Immunity*, 7: 37-47.
898 Bosch, Marie K, Yarimar Carrasquillo, Joseph L Ransdell, Ajay Kanakamedala, David M Ornitz, and
899 Jeanne M Nerbonne. 2015. 'Intracellular FGF14 (iFGF14) is required for spontaneous and evoked
900 firing in cerebellar Purkinje neurons and for motor coordination and balance', *Journal of*
901 *Neuroscience*, 35: 6752-69.
902 Bradley, A., K. Anastassiadis, A. Ayadi, J. F. Battey, C. Bell, M. C. Birling, J. Bottomley, S. D. Brown, A.
903 Bürger, C. J. Bult, W. Bushell, F. S. Collins, C. Desaintes, B. Doe, A. Economides, J. T. Eppig, R.
904 H. Finnell, C. Fletcher, M. Fray, D. Frendewey, R. H. Friedel, F. G. Grosveld, J. Hansen, Y.
905 Hérault, G. Hicks, A. Hörlein, R. Houghton, M. Hrabé de Angelis, D. Huylebroeck, V. Iyer, P. J.
906 de Jong, J. A. Kadin, C. Kaloff, K. Kennedy, M. Koutsourakis, K. C. Lloyd, S. Marschall, J. Mason,
907 C. McKerlie, M. P. McLeod, H. von Melchner, M. Moore, A. O. Mujica, A. Nagy, M. Nefedov, L.
908 M. Nutter, G. Pavlovic, J. L. Peterson, J. Pollock, R. Ramirez-Solis, D. E. Rancourt, M. Raspa, J.
909 E. Remacle, M. Ringwald, B. Rosen, N. Rosenthal, J. Rossant, P. Ruiz Noppinger, E. Ryder, J.
910 Z. Schick, F. Schnütgen, P. Schofield, C. Seisenberger, M. Selloum, E. M. Simpson, W. C.
911 Skarnes, D. Smedley, W. L. Stanford, A. F. Stewart, K. Stone, K. Swan, H. Tadepally, L. Teboul,
912 G. P. Tocchini-Valentini, D. Valenzuela, A. P. West, K. Yamamura, Y. Yoshinaga, and W. Wurst.
913 2012. 'The mammalian gene function resource: the International Knockout Mouse Consortium',
914 *Mammalian Genome*, 23: 580-6.
915 Bredemeyer, Andrea L, Girdhar G Sharma, Ching-Yu Huang, Beth A Helmink, Laura M Walker, Katrina
916 C Khor, Beth Nuskey, Kathleen E Sullivan, Tej K Pandita, and Craig H Bassing. 2006. 'ATM
917 stabilizes DNA double-strand-break complexes during V (D) J recombination', *Nature*, 442: 466-
918 70.
919 Browne, Susan E., L. Jackson Roberts, Phyllis A. Dennery, Susan R. Doctrow, M. Flint Beal, Carrolee
920 Barlow, and Rodney L. Levine. 2004. 'Treatment with a catalytic antioxidant corrects the
921 neurobehavioral defect in ataxia–telangiectasia mice', *Free Radical Biology and Medicine*, 36:
922 938-42.
923 Çaglayan, Melike, Rajendra Prasad, Rachel Krasich, Matthew J. Longley, Kei Kadoda, Masataka Tsuda,
924 Hiroyuki Sasanuma, Shunichi Takeda, Keizo Tano, William C. Copeland, and Samuel H. Wilson.
925 2017. 'Complementation of aprataxin deficiency by base excision repair enzymes in mitochondrial
926 extracts', *Nucleic Acids Research*, 45: 10079-88.
927 Campbell, A., B. Krupp, J. Bushman, M. Noble, C. Pröschel, and M. Mayer-Pröschel. 2015. 'A novel
928 mouse model for ataxia-telangiectasia with a N-terminal mutation displays a behavioral defect
929 and a low incidence of lymphoma but no increased oxidative burden', *Human Molecular Genetics*,
930 24: 6331-49.

Campbell, Andrew, Jared Bushman, Joshua Munger, Mark Noble, Christoph Pröschel, and Margot Mayer-Pröschel. 2016. 'Mutation of ataxia–telangiectasia mutated is associated with dysfunctional glutathione homeostasis in cerebellar astroglia', *Glia*, 64: 227-39.

Chao, Connie, Eva Marie Yang, and Yang Xu. 2000. 'Rescue of Defective T Cell Development and Function in Atm^{−/−} Mice by a Functional TCRαβ Transgene', *The Journal of Immunology*, 164: 345-49.

Chatterjee, Nimrat, and Graham C. Walker. 2017. 'Mechanisms of DNA damage, repair, and mutagenesis', *Environmental and Molecular Mutagenesis*, 58: 235-63.

Chen, Philip, Cheng Peng, John Luff, Kevin Spring, Dianne Watters, Steven Bottle, Shigeki Furuya, and Martin F. Lavin. 2003. 'Oxidative Stress Is Responsible for Deficient Survival and Dendritogenesis in Purkinje Neurons from Ataxia-Telangiectasia Mutated Mutant Mice', *The Journal of Neuroscience*, 23: 11453-60.

Chen, Xi, Tie-Shan Tang, Huiping Tu, Omar Nelson, Mark Pook, Robert Hammer, Nobuyuki Nukina, and Ilya Bezprozvanny. 2008. 'Deranged calcium signaling and neurodegeneration in spinocerebellar ataxia type 3', *Journal of Neuroscience*, 28: 12713-24.

Chou, W. C., L. Y. Hu, C. N. Hsiung, and C. Y. Shen. 2015. 'Initiation of the ATM-Chk2 DNA damage response through the base excision repair pathway', *Carcinogenesis*, 36: 832-40.

Clark, H Brent, Eric N Burright, Wael S Yunis, Seth Larson, Claire Wilcox, Boyd Hartman, Antoni Matilla, Huda Y Zoghbi, and Harry T Orr. 1997. 'Purkinje Cell Expression of a Mutant Allele of SCA1in Transgenic Mice Leads to Disparate Effects on Motor Behaviors, Followed by a Progressive Cerebellar Dysfunction and Histological Alterations', *Journal of Neuroscience*, 17: 7385-95.

Clements, P. M., C. Breslin, E. D. Deeks, P. J. Byrd, L. Ju, P. Bieganowski, C. Brenner, M. C. Moreira, A. M. Taylor, and K. W. Caldecott. 2004. 'The ataxia-oculomotor apraxia 1 gene product has a role distinct from ATM and interacts with the DNA strand break repair proteins XRCC1 and XRCC4', *DNA Repair (Amst)*, 3: 1493-502.

Concannon, P., and R. A. Gatti. 1997. 'Diversity of ATM gene mutations detected in patients with ataxia-telangiectasia', *Human Mutation*, 10: 100-7.

Cook, Anna A., Eviatar Fields, and Alanna J. Watt. 2020. 'Losing the Beat: Contribution of Purkinje Cell Firing Dysfunction to Disease, and Its Reversal', *Neuroscience*.

Coutinho P, Barbot C, Coutinho P. 2002. 'Ataxia with Oculomotor Apraxia Type 1.' in Ardinger HH Adam MP, Pagon RA, et al. (ed.), *GeneReviews*® (GeneReviews® [Internet]: University of Washington, Seattle).

Crawford, T. O., R. L. Skolasky, R. Fernandez, K. J. Rosquist, and H. M. Lederman. 2006. 'Survival probability in ataxia telangiectasia', *Archives of Disease in Childhood*, 91: 610-11.

De Leon, G. A., W. D. Grover, and D. S. Huff. 1976. 'Neuropathologic changes in ataxia-telangiectasia', *Neurology*, 26: 947-51.

Dell'Orco, James M., Aaron H. Wasserman, Ravi Chopra, Melissa A. C. Ingram, Yuan-Shih Hu, Vikrant Singh, Heike Wulff, Puneet Opal, Harry T. Orr, and Vikram G. Shakkottai. 2015. 'Neuronal Atrophy Early in Degenerative Ataxia Is a Compensatory Mechanism to Regulate Membrane Excitability', *The Journal of Neuroscience*, 35: 11292-307.

Dell'Orco, James M, Stefan M Pulst, and Vikram G Shakkottai. 2017. 'Potassium channel dysfunction underlies Purkinje neuron spiking abnormalities in spinocerebellar ataxia type 2', *Human Molecular Genetics*, 26: 3935-45.

Demaerel, PH, BE Kendall, and D Kingsley. 1992. 'Cranial CT and MRI in diseases with DNA repair defects', *Neuroradiology*, 34: 117-21.

Dineen, Rob A., Felix Raschke, Hannah L. McGlashan, Stefan Pszczolkowski, Lorna Hack, Andrew D. Cooper, Manish Prasad, Gabriel Chow, William P. Whitehouse, and Dorothee P. Auer. 2020. 'Multiparametric cerebellar imaging and clinical phenotype in childhood ataxia telangiectasia', *NeuroImage: Clinical*, 25: 102110.

Du, L., M. E. Jung, R. Damoiseaux, G. Completo, F. Fike, J. M. Ku, S. Nahas, C. Piao, H. Hu, and R. A. Gatti. 2013. 'A new series of small molecular weight compounds induce read through of all three types of nonsense mutations in the ATM gene', *Molecular Therapy*, 21: 1653-60.

983 El-Brolosy, Mohamed A., and Didier Y. R. Stainier. 2017. 'Genetic compensation: A phenomenon in
984 search of mechanisms', *Plos Genetics*, 13: e1006780-e80.
985 Elson, A., Y. Wang, C. J. Daugherty, C. C. Morton, F. Zhou, J. Campos-Torres, and P. Leder. 1996.
986 'Pleiotropic defects in ataxia-telangiectasia protein-deficient mice', *Proceedings of the National*
987 *Academy of Sciences of the United States of America*, 93: 13084-9.
988 Gao, Zhenyu, Boeke J van Beugen, and Chris I De Zeeuw. 2012. 'Distributed synergistic plasticity and
989 cerebellar learning', *Nature Reviews: Neuroscience*, 13: 619-35.
990 Gatti, R. A., and H. V. Vinters. 1985. 'Cerebellar pathology in ataxia-telangiectasia: the significance of
991 basket cells', *Kroc Foundation Series*, 19: 225-32.
992 Genik, P. C., H. Bielefeldt-Ohmann, X. Liu, M. D. Story, L. Ding, J. M. Bush, C. M. Fallgren, and M. M.
993 Weil. 2014. 'Strain background determines lymphoma incidence in Atm knockout mice',
994 *Neoplasia*, 16: 129-36.
995 Germain, Ronald N. 2002. 'T-cell development and the CD4–CD8 lineage decision', *Nature Reviews*
996 *Immunology*, 2: 309-22.
997 Gertsenstein, Marina, Lauryl M. J. Nutter, Tammy Reid, Monica Pereira, William L. Stanford, Janet
998 Rossant, and Andras Nagy. 2010. 'Efficient Generation of Germ Line Transmitting Chimeras from
999 C57BL/6N ES Cells by Aggregation with Outbred Host Embryos', *PloS One*, 5: e11260.
1000 Gilad, Shlomit, Rami Khosravi, Dganit Shkedy, Tamar Uziel, Yael Ziv, Kinneret Savitsky, Galit Rotman,
1001 Sara Smith, Luciana Chessa, Timothy J. Jorgensen, Reli Harnik, Moshe Frydman, Ozden Sanal,
1002 Sima Portnoi, Zipora Goldwicz, N. G. J. Jaspers, Richard A. Gatti, Gilbert Lenoir, Martin F. Lavin,
1003 Kouichi Tatsumi, Rolf D. Wegner, Yosef Shiloh, and Anat Bar-Shira. 1996. 'Predominance of Null
1004 Mutations in Ataxia-Telangiectasia', *Human Molecular Genetics*, 5: 433-39.
1005 Gueven, N., O. J. Becherel, A. W. Kijas, P. Chen, O. Howe, J. H. Rudolph, R. Gatti, H. Date, O. Onodera,
1006 G. Taucher-Scholz, and M. F. Lavin. 2004. 'Aprataxin, a novel protein that protects against
1007 genotoxic stress', *Human Molecular Genetics*, 13: 1081-93.
1008 Guo, Zhi, Sergei Kozlov, Martin F. Lavin, Maria D. Person, and Tanya T. Paull. 2010. 'ATM Activation by
1009 Oxidative Stress', *Science*, 330: 517-21.
1010 Hansel, Christian, and David J. Linden. 2000. 'Long-Term Depression of the Cerebellar Climbing Fiber–
1011 Purkinje Neuron Synapse', *Neuron*, 26: 473-82.
1012 Hansen, Stephen T, Pratap Meera, Thomas S Otis, and Stefan M Pulst. 2013. 'Changes in Purkinje cell
1013 firing and gene expression precede behavioral pathology in a mouse model of SCA2', *Human*
1014 *Molecular Genetics*, 22: 271-83.
1015 Hathcock, K. S., S. Bowen, F. Livak, and R. J. Hodes. 2013. 'ATM influences the efficiency of TCRbeta
1016 rearrangement, subsequent TCRbeta-dependent T cell development, and generation of the pre-
1017 selection TCRbeta CDR3 repertoire', *PloS One*, 8: e62188.
1018 Herzog, Karl-Heinz, Miriam J. Chong, Manuela Kapsetaki, James I. Morgan, and Peter J. McKinnon.
1019 1998. 'Requirement for Atm in Ionizing Radiation-Induced Cell Death in the Developing Central
1020 Nervous System', *Science*, 280: 1089-91.
1021 Hoche, F., K. Seidel, M. Theis, S. Vlaho, R. Schubert, S. Zielen, and M. Kieslich. 2012.
1022 'Neurodegeneration in ataxia telangiectasia: what is new? What is evident?', *Neuropediatrics*, 43:
1023 119-29.
1024 Hourez, Raphael, Laurent Servais, David Orduz, David Gall, Isabelle Millard, Alban de Kerchove
1025 d'Exaerde, Guy Cheron, Harry T Orr, Massimo Pandolfo, and Serge N Schiffmann. 2011.
1026 'Aminopyridines correct early dysfunction and delay neurodegeneration in a mouse model of
1027 spinocerebellar ataxia type 1', *Journal of Neuroscience*, 31: 11795-807.
1028 Hoxha, Eriola, Ilaria Balbo, Maria Concetta Miniaci, and Filippo Tempia. 2018. 'Purkinje Cell Signaling
1029 Deficits in Animal Models of Ataxia', *Frontiers in Synaptic Neuroscience*, 10: 6-6.
1030 Hurlock, Edward C, Anne McMahon, and Rolf H Joho. 2008. 'Purkinje-cell-restricted restoration of Kv3.
1031 3 function restores complex spikes and rescues motor coordination in Kcnc3 mutants', *Journal of*
1032 *Neuroscience*, 28: 4640-48.
1033 Jackson, Thomas J, Gabriel Chow, Mohnish Suri, Philip Byrd, Malcolm R Taylor, and William P
1034 Whitehouse. 2016. 'Longitudinal analysis of the neurological features of ataxia-telangiectasia',
1035 *Developmental Medicine and Child Neurology*, 58: 690-97.

1036 Jayabal, Sriram, Hui Ho Vanessa Chang, Kathleen E Cullen, and Alanna J Watt. 2016. '4-aminopyridine
1037 reverses ataxia and cerebellar firing deficiency in a mouse model of spinocerebellar ataxia type
1038 6', *Scientific Reports*, 6: 1-12.
1039 Kaminsky, Natalie, Ofer Bihari, Sivan Kanner, and Ari Barzilai. 2016. 'Connecting Malfunctioning Glial
1040 Cells and Brain Degenerative Disorders', *Genomics, Proteomics & Bioinformatics*, 14: 155-65.
1041 Kano, Masanobu, and Takaki Watanabe. 2017. 'Type-1 metabotropic glutamate receptor signaling in
1042 cerebellar Purkinje cells in health and disease', *F1000Research*, 6: 416-16.
1043 Kastan, M. B., and J. Bartek. 2004. 'Cell-cycle checkpoints and cancer', *Nature*, 432: 316-23.
1044 Kasumu, Adebimpe, and Ilya Bezprozvanny. 2012. 'Deranged calcium signaling in Purkinje cells and
1045 pathogenesis in spinocerebellar ataxia 2 (SCA2) and other ataxias', *The Cerebellum*, 11: 630-39.
1046 Kim, Jusik, Keeeun Kim, Jung-Soon Mo, and Youngsoo Lee. 2020. 'Atm deficiency in the DNA
1047 polymerase β null cerebellum results in cerebellar ataxia and Itpr1 reduction associated with
1048 alteration of cytosine methylation', *Nucleic Acids Research*, 48: 3678-91.
1049 Krangel, Michael S. 2009. 'Mechanics of T cell receptor gene rearrangement', *Current Opinion in*
1050 *Immunology*, 21: 133-39.
1051 Larivière, Roxanne, Nicolas Sgarioto, Brenda Toscano Márquez, Rébecca Gaudet, Karine Choquet, R
1052 Anne McKinney, Alanna J Watt, and Bernard Brais. 2019. 'Sacs R272C missense homozygous
1053 mice develop an ataxia phenotype', *Molecular Brain*, 12: 1-15.
1054 Lavin, M. F. 2013. 'The appropriateness of the mouse model for ataxia-telangiectasia: neurological
1055 defects but no neurodegeneration', *DNA Repair (Amst)*, 12: 612-9.
1056 Levy, Ariel, and Anthony E. Lang. 2018. 'Ataxia-telangiectasia: A review of movement disorders, clinical
1057 features, and genotype correlations', *Movement Disorders*, 33: 1238-47.
1058 Li, J., Y. R. Han, M. R. Plummer, and K. Herrup. 2009. 'Cytoplasmic ATM in neurons modulates synaptic
1059 function', *Current Biology*, 19: 2091-6.
1060 Li, Jiali, Jianmin Chen, Harry V. Vinters, Richard A. Gatti, and Karl Herrup. 2011. 'Stable Brain
1061 ATM Message and Residual Kinase-Active ATM Protein in Ataxia-Telangiectasia',
1062 *The Journal of Neuroscience*, 31: 7568-77.
1063 Lindahl, T., and D. E. Barnes. 2000. 'Repair of endogenous DNA damage', *Cold Spring Harbor Symposia*
1064 *on Quantitative Biology*, 65: 127-33.
1065 Liu, Jing, Tie-Shan Tang, Huiping Tu, Omar Nelson, Emily Herndon, Duong P Huynh, Stefan M Pulst,
1066 and Ilya Bezprozvanny. 2009. 'Deranged calcium signaling and neurodegeneration in
1067 spinocerebellar ataxia type 2', *Journal of Neuroscience*, 29: 9148-62.
1068 Livák, Ferenc, Michelle Tourigny, David G. Schatz, and Howard T. Petrie. 1999. 'Characterization of TCR
1069 Gene Rearrangements During Adult Murine T Cell Development', *The Journal of Immunology*,
1070 162: 2575-80.
1071 Lorenzetti, Diego, Kei Watase, Bisong Xu, Martin M Matzuk, Harry T Orr, and Huda Y Zoghbi. 2000.
1072 'Repeat instability and motor incoordination in mice with a targeted expanded CAG repeat in the
1073 Sca1 locus', *Human Molecular Genetics*, 9: 779-85.
1074 Marshall, Jean S., Richard Warrington, Wade Watson, and Harold L. Kim. 2018. 'An introduction to
1075 immunology and immunopathology', *Allergy, asthma, and clinical immunology : official journal of*
1076 *the Canadian Society of Allergy and Clinical Immunology*, 14: 49-49.
1077 Matei, I. R., C. J. Guidos, and J. S. Danska. 2006. 'ATM-dependent DNA damage surveillance in T-cell
1078 development and leukemogenesis: the DSB connection', *Immunological Reviews*, 209: 142-58.
1079 Matsuoka, Shuhei, Bryan A. Ballif, Agata Smogorzewska, E. Robert McDonald, Kristen E. Hurov, Ji Luo,
1080 Corey E. Bakalarski, Zhenming Zhao, Nicole Solimini, Yaniv Lerenthal, Yosef Shiloh, Steven P.
1081 Gygi, and Stephen J. Elledge. 2007. 'ATM and ATR Substrate Analysis Reveals Extensive Protein
1082 Networks Responsive to DNA Damage', *Science*, 316: 1160-66.
1083 McKinnon, P. J. 2009. 'DNA repair deficiency and neurological disease', *Nature Reviews: Neuroscience*,
1084 10: 100-12.
1085 Meagher, M., and R. N. Lightowlers. 2014. 'The role of TDP1 and APTX in mitochondrial DNA repair',
1086 *Biochimie*, 100: 121-4.
1087 Micol, R., L. Ben Slama, F. Suarez, L. Le Mignot, J. Beauté, N. Mahlaoui, C. Dubois d'Enghien, A. Laugé,
1088 J. Hall, J. Couturier, L. Vallée, B. Delobel, F. Rivier, K. Nguyen, T. Billette de Villemeur, J. L.

Stephan, P. Bordigoni, Y. Bertrand, N. Aladjidi, J. M. Pedespan, C. Thomas, I. Pellier, M. Koenig, O. Hermine, C. Picard, D. Moshous, B. Neven, F. Lanternier, S. Blanche, M. Tardieu, M. Debré, A. Fischer, and D. Stoppa-Lyonnet. 2011. 'Morbidity and mortality from ataxia-telangiectasia are associated with ATM genotype', *Journal of Allergy and Clinical Immunology*, 128: 382-9.e1.

Monaco, S., E. Nardelli, G. Moretto, T. Cavallaro, and N. Rizzuto. 1988. 'Cytoskeletal pathology in ataxia-telangiectasia', *Clinical Neuropathology*, 7: 44-6.

Moreira, M. C., S. Klur, M. Watanabe, A. H. Németh, I. Le Ber, J. C. Moniz, C. Tranchant, P. Aubourg, M. Tazir, L. Schöls, M. Pandolfo, J. B. Schulz, J. Pouget, P. Calvas, M. Shizuka-Ikeda, M. Shoji, M. Tanaka, L. Izatt, C. E. Shaw, A. M'Zahem, E. Dunne, P. Bomont, T. Benhassine, N. Bouslam, G. Stevanin, A. Brice, J. Guimarães, P. Mendonça, C. Barbot, P. Coutinho, J. Sequeiros, A. Dürr, J. M. Warter, and M. Koenig. 2004. 'Senataxin, the ortholog of a yeast RNA helicase, is mutant in ataxia-ocular apraxia 2', *Nature Genetics*, 36: 225-7.

Morrell, Daphne, Elizabeth Cromartie, and Michael Swift. 1986. 'Mortality and cancer incidence in 263 patients with ataxia-telangiectasia', *Journal of the National Cancer Institute*, 77: 89-92.

Paula-Barbosa, M. M., C. Ruela, M. A. Tavares, C. Pontes, A. Saraiva, and C. Cruz. 1983. 'Cerebellar cortex ultrastructure in ataxia-telangiectasia', *Annals of Neurology*, 13: 297-302.

Perkins, Emma M, Yvonne L Clarkson, Nancy Sabatier, David M Longhurst, Christopher P Millward, Jennifer Jack, Junko Toraiwa, Mitsunori Watanabe, Jeffrey D Rothstein, and Alastair R Lyndon. 2010. 'Loss of β-III spectrin leads to Purkinje cell dysfunction recapitulating the behavior and neuropathology of spinocerebellar ataxia type 5 in humans', *Journal of Neuroscience*, 30: 4857-67.

Petersen, Andrew J., Stacey A. Rimkus, and David A. Wassarman. 2012. 'ATM kinase inhibition in glial cells activates the innate immune response and causes neurodegeneration in Drosophila', *Proceedings of the National Academy of Sciences*, 109: E656-E64.

Pizzamiglio, L., E. Focchi, and F. Antonucci. 2020. 'ATM Protein Kinase: Old and New Implications in Neuronal Pathways and Brain Circuitry', *Cells*, 9.

Quarantelli, Mario, Giuliana Giardino, Anna Prinster, Giuseppina Aloj, Barbara Carotenuto, Emilia Cirillo, Angela Marsili, Elena Salvatore, Ennio Del Giudice, and Claudio Pignata. 2013. 'Steroid treatment in Ataxia-Telangiectasia induces alterations of functional magnetic resonance imaging during prono-supination task', *European Journal of Paediatric Neurology*, 17: 135-40.

Quek, Hazel, John Luff, KaGeen Cheung, Sergei Kozlov, Magtouf Gatei, C. Soon Lee, Mark C. Bellingham, Peter G. Noakes, Yi Chieh Lim, Nigel L. Barnett, Steven Dingwall, Ernst Wolvetang, Tomoji Mashimo, Tara L. Roberts, and Martin F. Lavin. 2016. 'A rat model of ataxia-telangiectasia: evidence for a neurodegenerative phenotype', *Human Molecular Genetics*, 26: 109-23.

Rashi-Elkeles, S., R. Elkon, N. Weizman, C. Linhart, N. Amariglio, G. Sternberg, G. Rechavi, A. Barzilai, R. Shamir, and Y. Shiloh. 2006. 'Parallel induction of ATM-dependent pro- and antiapoptotic signals in response to ionizing radiation in murine lymphoid tissue', *Oncogene*, 25: 1584-92.

Rass, Ulrich, Ivan Ahel, and Stephen C. West. 2007. 'Defective DNA Repair and Neurodegenerative Disease', *Cell*, 130: 991-1004.

Rogers, D. C., E. M. Fisher, S. D. Brown, J. Peters, A. J. Hunter, and J. E. Martin. 1997. 'Behavioral and functional analysis of mouse phenotype: SHIRPA, a proposed protocol for comprehensive phenotype assessment', *Mammalian Genome*, 8: 711-3.

Rothblum-Oviatt, Cynthia, Jennifer Wright, Maureen A. Lefton-Greif, Sharon A. McGrath-Morrow, Thomas O. Crawford, and Howard M. Lederman. 2016. 'Ataxia telangiectasia: a review', *Orphanet Journal of Rare Diseases*, 11: 159.

Sahama, Ishani, Kate Sinclair, Simona Fiori, James Doecke, Kerstin Pannek, Lee Reid, Martin Lavin, and Stephen Rose. 2015. 'Motor pathway degeneration in young ataxia telangiectasia patients: A diffusion tractography study', *NeuroImage: Clinical*, 9: 206-15.

Sahama, Ishani, Kate Sinclair, Kerstin Pannek, Martin Lavin, and Stephen Rose. 2014. 'Radiological imaging in ataxia telangiectasia: a review', *The Cerebellum*, 13: 521-30.

Sandoval, N., M. Platzer, A. Rosenthal, T. Dork, R. Bendix, B. Skawran, M. Stuhrmann, R. D. Wegner, K. Sperling, S. Banin, Y. Shiloh, A. Baumer, U. Bernthaler, H. Sennefelder, M. Brohm, B. H.

Weber, and D. Schindler. 1999. 'Characterization of ATM gene mutations in 66 ataxia telangiectasia families', *Human Molecular Genetics*, 8: 69-79.

Sanghez, Valentina, Anna Luzzi, Don Clarke, Dustin Kee, Steven Beuder, Danielle Rux, Mitsujiro Osawa, Joaquín Madrenas, Tsui-Fen Chou, Michael Kyba, and Michelina Iacovino. 2017. 'Notch activation is required for downregulation of HoxA3-dependent endothelial cell phenotype during blood formation', *PloS One*, 12: e0186818.

Savitsky, K., A. Bar-Shira, S. Gilad, G. Rotman, Y. Ziv, L. Vanagaite, D. A. Tagle, S. Smith, T. Uziel, S. Sfez, M. Ashkenazi, I. Pecker, M. Frydman, R. Harnik, S. R. Patanjali, A. Simmons, G. A. Clines, A. Sartiel, R. A. Gatti, L. Chessa, O. Sanal, M. F. Lavin, N. G. Jaspers, A. M. Taylor, C. F. Arlett, T. Miki, S. M. Weissman, M. Lovett, F. S. Collins, and Y. Shiloh. 1995. 'A single ataxia telangiectasia gene with a product similar to PI-3 kinase', *Science*, 268: 1749-53.

Schellenberg, M. J., P. P. Tumbale, and R. S. Williams. 2015. 'Molecular underpinnings of Aprataxin RNA/DNA deadenylase function and dysfunction in neurological disease', *Progress in Biophysics and Molecular Biology*, 117: 157-65.

Schubert, R., J. Reichenbach, and S. Zielen. 2002. 'Deficiencies in CD4+ and CD8+ T cell subsets in ataxia telangiectasia', *Clinical and Experimental Immunology*, 129: 125-32.

Sedghi, Maryam, Mehri Salari, Ali-Reza Moslemi, Ariana Kariminejad, Mark Davis, Hayley Goullée, Björn Olsson, Nigel Laing, and Homa Tajsharghi. 2018. 'Ataxia-telangiectasia-like disorder in a family deficient for MRE11A, caused by a MRE11 variant', *Neurology Genetics*, 4: e295.

Shakkottai, Vikram G, Maria do Carmo Costa, James M Dell'Orco, Ananthakrishnan Sankaranarayanan, Heike Wulff, and Henry L Paulson. 2011a. 'Early changes in cerebellar physiology accompany motor dysfunction in the polyglutamine disease spinocerebellar ataxia type 3', *Journal of Neuroscience*, 31: 13002-14.

Shakkottai, Vikram G, Maolei Xiao, Lin Xu, Michael Wong, Jeanne M Nerbonne, David M Ornitz, and Kelvin A Yamada. 2009. 'FGF14 regulates the intrinsic excitability of cerebellar Purkinje neurons', *Neurobiology of Disease*, 33: 81-88.

Shakkottai, Vikram G., Maria do Carmo Costa, James M. Dell'Orco, Ananthakrishnan Sankaranarayanan, Heike Wulff, and Henry L. Paulson. 2011b. 'Early Changes in Cerebellar Physiology Accompany Motor Dysfunction in the Polyglutamine Disease Spinocerebellar Ataxia Type 3', *The Journal of Neuroscience*, 31: 13002-14.

Shiloh, Yosef. 2020. 'The cerebellar degeneration in ataxia-telangiectasia: A case for genome instability', *DNA Repair*, 95: 102950.

Shiloh, Yosef, and Yael Ziv. 2013. 'The ATM protein kinase: regulating the cellular response to genotoxic stress, and more', *Nature Reviews Molecular Cell Biology*, 14: 197-210.

Solitare, G. B. 1968. 'Louis-Bar's syndrome (ataxia-telangiectasia). Anatomic considerations with emphasis on neuropathologic observations', *Neurology*, 18: 1180-6.

Solitare, G. B., and V. F. Lopez. 1967. 'Louis-bar's syndrome (ataxia-telangiectasia). Neuropathologic observations', *Neurology*, 17: 23-31.

Spring, K., S. Cross, C. Li, D. Watters, L. Ben-Senior, P. Waring, F. Ahangari, S. L. Lu, P. Chen, I. Misko, C. Paterson, G. Kay, N. I. Smorodinsky, Y. Shiloh, and M. F. Lavin. 2001. 'Atm knock-in mice harboring an in-frame deletion corresponding to the human ATM 7636del9 common mutation exhibit a variant phenotype', *Cancer Research*, 61: 4561-8.

Staples, E. R., E. M. McDermott, A. Reiman, P. J. Byrd, S. Ritchie, A. M. Taylor, and E. G. Davies. 2008. 'Immunodeficiency in ataxia telangiectasia is correlated strongly with the presence of two null mutations in the ataxia telangiectasia mutated gene', *Clinical and Experimental Immunology*, 153: 214-20.

Stoyas, Colleen A, David D Bushart, Pawel M Switonski, Jacqueline M Ward, Akshay Alaghatta, Mi-bo Tang, Chenchen Niu, Mandheer Wadhwa, Haoran Huang, and Alex Savchenko. 2020. 'Nicotinamide pathway-dependent Sirt1 activation restores calcium homeostasis to achieve neuroprotection in spinocerebellar ataxia type 7', *Neuron*, 105: 630-44. e9.

Strich, Sabina J. 1966. 'Pathological findings in three cases of ataxia-telangiectasia', *Journal of Neurology, Neurosurgery, and Psychiatry*, 29: 489.

1193 Swift, M., D. Morrell, E. Cromartie, A. R. Chamberlin, M. H. Skolnick, and D. T. Bishop. 1986. 'The
1194 incidence and gene frequency of ataxia-telangiectasia in the United States', *American Journal of*
1195 *Human Genetics*, 39: 573-83.
1196 Sykora, Peter, Deborah L. Croteau, Vilhelm A. Bohr, and David M. Wilson, 3rd. 2011. 'Aprataxin localizes
1197 to mitochondria and preserves mitochondrial function', *Proceedings of the National Academy of*
1198 *Sciences of the United States of America*, 108: 7437-42.
1199 Takashima, H., C. F. Boerkoel, J. John, G. M. Saifi, M. A. Salih, D. Armstrong, Y. Mao, F. A. Quiocho, B.
1200 B. Roa, M. Nakagawa, D. W. Stockton, and J. R. Lupski. 2002. 'Mutation of TDP1, encoding a
1201 topoisomerase I-dependent DNA damage repair enzyme, in spinocerebellar ataxia with axonal
1202 neuropathy', *Nature Genetics*, 32: 267-72.
1203 Tal, Efrat, Marina Alfo, Shan Zha, Ari Barzilai, Chris I. De Zeeuw, Yael Ziv, and Yosef Shiloh. 2018.
1204 'Inactive Atm abrogates DSB repair in mouse cerebellum more than does Atm loss, without
1205 causing a neurological phenotype', *DNA Repair*, 72: 10-17.
1206 Tavani, F., R. A. Zimmerman, G. T. Berry, K. Sullivan, R. Gatti, and P. Bingham. 2003. 'Ataxia-
1207 telangiectasia: the pattern of cerebellar atrophy on MRI', *Neuroradiology*, 45: 315-19.
1208 Taylor, A. M., Z. Lam, J. I. Last, and P. J. Byrd. 2015. 'Ataxia telangiectasia: more variation at clinical and
1209 cellular levels', *Clinical Genetics*, 87: 199-208.
1210 Terplan, K. L., and R. F. Krauss. 1969. 'Histopathologic brain changes in association with ataxia-
1211 telangiectasia', *Neurology*, 19: 446-54.
1212 Tsutsumi, S., M. Yamazaki, T. Miyazaki, M. Watanabe, K. Sakimura, M. Kano, and K. Kitamura. 2015.
1213 'Structure-function relationships between aldolase C/zebrin II expression and complex spike
1214 synchrony in the cerebellum', *Journal of Neuroscience*, 35: 843-52.
1215 Tumbale, Percy, Matthew J Schellenberg, Geoffrey A Mueller, Emma Fairweather, Mandy Watson,
1216 Jessica N Little, Juno Krahn, Ian Waddell, Robert E London, and R Scott Williams. 2018.
1217 'Mechanism of APTX nicked DNA sensing and pleiotropic inactivation in neurodegenerative
1218 disease', *The EMBO Journal*, 37: e98875.
1219 Vacchio, Melanie S., Alexandru Olaru, Ferenc Livak, and Richard J. Hodes. 2007. 'ATM deficiency
1220 impairs thymocyte maturation because of defective resolution of T cell receptor α locus coding
1221 end breaks', *Proceedings of the National Academy of Sciences*, 104: 6323-28.
1222 Vail, Graham, Aifang Cheng, Yu Ray Han, Teng Zhao, Shengwang Du, Michael M. T. Loy, Karl Herrup,
1223 and Mark R. Plummer. 2016. 'ATM protein is located on presynaptic vesicles and its deficit leads
1224 to failures in synaptic plasticity', *Journal of Neurophysiology*, 116: 201-09.
1225 Valentin-Vega, Y. A., and M. B. Kastan. 2012. 'A new role for ATM: regulating mitochondrial function and
1226 mitophagy', *Autophagy*, 8: 840-1.
1227 van der Burgt, I, K H Chrzanowska, D Smeets, and C Weemaes. 1996. 'Nijmegen breakage syndrome',
1228 *Journal of Medical Genetics*, 33: 153-56.
1229 Verhagen, Mijke M.M., Jean-Jacques Martin, Marcel van Deuren, Chantal Ceuterick-de Groote, Corry
1230 M.R. Weemaes, Berry H.P.H. Kremer, Malcolm A.R. Taylor, Michèl A.A.P. Willemsen, and Martin
1231 Lammens. 2012. 'Neuropathology in classical and variant ataxia-telangiectasia', *Neuropathology*,
1232 32: 234-44.
1233 Voogd, Jan, and Mitchell Glickstein. 1998. 'The anatomy of the cerebellum', *Trends in Neurosciences*,
1234 21: 370-75.
1235 Wakasugi, M., T. Sasaki, M. Matsumoto, M. Nagaoka, K. Inoue, M. Inobe, K. Horibata, K. Tanaka, and
1236 T. Matsunaga. 2014. 'Nucleotide excision repair-dependent DNA double-strand break formation
1237 and ATM signaling activation in mammalian quiescent cells', *Journal of Biological Chemistry*, 289:
1238 28730-7.
1239 Wallis, LI, PD Griffiths, SJ Ritchie, CAJ Romanowski, G Darwent, and ID Wilkinson. 2007. 'Proton
1240 spectroscopy and imaging at 3T in ataxia-telangiectasia', *American journal of neuroradiology*, 28:
1241 79-83.
1242 Walter, Joy T, Karina Alvina, Mary D Womack, Carolyn Chevez, and Kamran Khodakhah. 2006.
1243 'Decreases in the precision of Purkinje cell pacemaking cause cerebellar dysfunction and ataxia',
1244 *Nature Neuroscience*, 9: 389-97.

Weyemi, Urbain, Christophe E. Redon, Towqir Aziz, Rohini Choudhuri, Daisuke Maeda, Palak R. Parekh, Michael Y. Bonner, Jack L. Arbiser, and William M. Bonner. 2015. 'NADPH oxidase 4 is a critical mediator in Ataxia telangiectasia disease', *Proceedings of the National Academy of Sciences*, 112: 2121-26.

Xu, Y., and D. Baltimore. 1996. 'Dual roles of ATM in the cellular response to radiation and in cell growth control', *Genes and Development*, 10: 2401-10.

Yamasaki, Miwako, Kouichi Hashimoto, and Masanobu Kano. 2006. 'Miniature Synaptic Events Elicited by Presynaptic Ca²+ Rise Are Selectively Suppressed by Cannabinoid Receptor Activation in Cerebellar Purkinje Cells', *The Journal of Neuroscience*, 26: 86-95.

Zhou, Haibo, Zhanmin Lin, Kai Voges, Chiheng Ju, Zhenyu Gao, Laurens W. J. Bosman, Tom J. H. Ruigrok, Freek E. Hoebeek, Chris I. De Zeeuw, and Martijn Schonewille. 2014. 'Cerebellar modules operate at different frequencies', *Elife*, 3: e02536.

Zhu, L., B. Scelfo, F. Tempia, B. Sacchetti, and P. Strata. 2006. 'Membrane excitability and fear conditioning in cerebellar Purkinje cell', *Neuroscience*, 140: 801-10.

1260 # 8.0 Figure Legends

1261 **Figure 1. New A-T mouse models expressing clinically related PTCs. A)** The *Atm* gene locus was
1262 targeted by homologous recombination of a targeting vector containing a modified NorCOMM cassette
1263 in intron one and the corresponding A-T PTC mutation in exon 3 to create the targeted Atm^{R35X} and
1264 Atm^{Q35X} ES cell lines. Following germline transmission of these alleles in mice, the floxed NorCOMM
1265 cassette was removed by Cre excision *in vivo* to produce the final Atm^{R35X} and Atm^{Q35X} mouse lines. **B)**
1266 Genotyping of A-T mouse models. PCR agarose gel of mouse DNA shows 151 bp wildtype (Wt) allele
1267 band and 241 bp Cre-excised targeted allele band. **C)** ATM levels were examined using immunoblot
1268 analyses of the spleen due to its high expression density in this tissue. Exemplar blots illustrate a gene
1269 dose effect of ATM protein expression in samples harvested from wildtype (Wt), heterozygous (het), and
1270 homozygous Atm^{R35x} and Atm^{Q35X} mice as indicated. **D)** Breeding scheme schematic for double mutant
1271 and control mice for this study. **E)** $Atm^{R35X/R35X}$; $Aptx^{-/-}$ mice develop an ataxia that at late stages results
1272 in a severe loss of motor coordination and ability to ambulate (see Videos S1-S4). Abbreviations for
1273 panel **1**: **hβA**-human beta Actin promotor; **ΔTK1-**delta TK1, inactivated Thymidine Kinase 1; **T2A**-self-
1274 cleaving peptide sequence; **Neo**-Neomycin gene; **PGKpA**-Phosphoglycerate kinase poly A tail; **loxP**-
1275 recombination elements are show as a blue triangle; orientation of the Gateway **attB** recombination
1276 elements by an orange arrow; orientation of the genotyping **F** and **R** primers is shown by green and blue
1277 arrows respectively; and engineered PTC sites are shown in exon 3 by a red circle.

1278 **Figure 2. Health and survivability of single and double mutant mice. A) Left:** The line color and
1279 symbol for each genotype is denoted and is consistent across all figures (1-8). **Right:** $Atm^{R35X/R35X}$; $Aptx^{-}$
1280 $^{/-}$ mice weighed significantly less than all control genotypes as indicated by the growth curves (± 95%
1281 confidence interval; dotted lines). Growth curve ($Atm^{R35X/R35X}$; $Aptx^{-/-}$ *vs.* controls): Male $k = 0.024$ *vs.*
1282 0.011-0.019, $Y_{max} = 21.8$ *vs.* 32.9-41.0 g, ($n = 3$ to 18); Female $k = 0.030$ *vs.* 0.017-0.022, $Y_{max} = 16.9$ *vs.*
1283 23.3-31.3, ($n = 2$ to 19). Sum of squares F-test run across all curves: Male $F_{(12, 364)} = 30.5$, ****$p<0.0001$,
1284 Female $F_{(12, 339)} = 28.3$, ****$p<0.0001$. **B)** ATM deficient mice, regardless of APTX expression, displayed
1285 significantly lower survivability with ~55% of mice deceased by P400. No statistical differences between

1286 ATM deficient mice were detected. Moreover, a single wildtype copy of the *Atm* gene was sufficient to
1287 prevent premature death (no statistical difference detected between *Atm*$^{R35X/Wt}$; *Aptx*$^{-/-}$ and *Atm*$^{Wt/Wt}$;
1288 *Aptx*$^{+/+}$ mice). Log-rank (Mantel-Cox) tests across all ($\chi^2_{(6, 217)} = 48.4$, ****$p<0.0001$), just the ATM
1289 deficient ($\chi^2_{(2, 217)} = 1.06$, $p=0.6$), and single comparisons to wildtype (see figure) were conducted. Total
1290 number of animals indicated in panel **C**. **C)** Pie charts illustrating that ATM deficient mice displayed a
1291 high prevalence of thymomas based on postmortem necropsies. "Other" probable causes of death
1292 included enlarged livers, and obstructed kidneys. "Missing" mice were presumed dead and cannibalized
1293 by cage mates, cause of death unknown. **Figure 2-figure supplement 1, Figure 2-source data**

1294 **Figure 3. *Atm*$^{R35X/R35X}$; *Aptx*$^{-/-}$ mice develop a progressive loss in motor coordination. A)**
1295 *Atm*$^{R35X/R35X}$; *Aptx*$^{-/-}$ mice take a similar amount of time to descend a vertical pole at P45, 120, and 210,
1296 but significantly longer at P400. These overall results were found to be similar for both male (left, $n = 2$
1297 to 12) and female (right, $n=4$ to 12) mice. **B)** Consistent with the vertical pole test, the gait of *Atm*$^{R35X/R35X}$;
1298 *Aptx*$^{-/-}$ mice measured during ambulation on a Catwalk gait analysis system was significantly different to
1299 controls by P400, but not before P210. This includes the percent of time a mouse spends with 3 *vs.* 1, 2,
1300 or 4 paws on the ground and the speed and cadence during each run across the platform. The effects of
1301 the two null mutations were generally similar between males (left, $n = 4$ to 21) and females (right, $n = 3$
1302 to 18). **C)** Behavioral data for male (blue) and female (pink) *Atm*$^{R35X/R35X}$; *Aptx*$^{-/-}$ (dark purple, left) and
1303 *Atm*$^{Wt/Wt}$; *Aptx*$^{+/+}$ (orange, right) mice are plotted at P30 (left 2 columns) and 400 (right 2 columns). Left-
1304 right asymmetries of the horizontal bars indicate a difference in performance between genotypes for the
1305 behavioral test listed in a column on the far left. A significant difference in the time to right during the
1306 righting reflex at P8 was observed in both Male and Female mice (bottom). **A** and **B** were examined via
1307 two-way ANOVA with age and genotype as factors followed by *potshot* Tukey's multiple comparison tests
1308 between *Atm*$^{R35X/R35X}$; *Aptx*$^{-/-}$ and each of the control genotypes. Behavioral tests in **C** were examined
1309 using a non-parametric Kruskal Wallace followed by *postdocs* Dunn's multiple comparisons tests.
1310 Symbol/color key: *Atm*$^{Wt/Wt}$; *Aptx*$^{+/+}$ (purple circle), *Atm*$^{Wt/Wt}$; *Aptx*$^{-/-}$ (blue diamond), *Atm*$^{R35X/R35X}$; *Aptx*$^{+/+}$

(green triangle), *Atm*$^{R35X/R35X}$; *Aptx*$^{-/-}$ (orange square), *Atm*$^{Wt/R35X}$; *Aptx*$^{-/-}$ (red inverted triangle) **Figure 3-figure supplement 1, Figure 3-source data**

Figure 4. The biophysical properties of PNs are significantly perturbed in *Atm*$^{R35X/R35X}$; *Aptx*$^{-/-}$ mice. A) Schematic diagram of intracellular recording from a single Purkinje neuron (PN) in an acute cerebellar tissue slice preparation used to examine their biophysical properties. **B) Left:** Voltage clamp measurements of PN neuron membrane properties were made from a $1\ \mathrm{s}$, $-5\ \mathrm{mV}$ step pulse as illustrated. **Right:** The membrane input resistance (R_m), time constant (τ), and capacitance (C_m) were perturbed in *Atm*$^{R35X/R35X}$; *Aptx*$^{-/-}$ compared to wildtype mice. **C)** Current clamp recordings of PN action potentials (AP) after $2\ \mathrm{nA}$ step pulses from a $-70\ \mathrm{mV}$ holding potential. PN action potentials recorded from *Atm*$^{R35X/R35X}$; *Aptx*$^{-/-}$ fail to maintain constant firing and summary plots show that they have lower 1st AP amplitudes, firing threshold, and area under the curve. **D) Top:** Example mEPSC recordings taken from a PN under voltage clamp at a $-80\ \mathrm{mV}$ holding potential. **Bottom:** Median frequency and amplitude data, along with the overall probability distribution function are plotted for both *Atm*$^{Wt/Wt}$; *Aptx*$^{+/+}$ ($n = 11$) and *Atm*$^{R35X/R35X}$; *Aptx*$^{-/-}$ ($n = 11$) mice. The frequency, but not amplitude of PNs recorded in *Atm*$^{R35X/R35X}$; *Aptx*$^{-/-}$ mice was found to be perturbed. **E and F) Left:** Example traces of evoked EPSCs recorded from PNs as a result of a 2-pulse stimulation ($50\ \mathrm{ms}$ interval) of either parallel (**G**) or climbing (**H**) axon fibers. Traces illustrate the first (A_1) and second (A_2) amplitude (normalized) and time course of first decay (blue fitted line) of each synaptic response. **Right:** Summary plots of the paired pulse ratio. While parallel fiber paired pulse facilitation was normal in *Atm*$^{R35X/R35X}$; *Aptx*$^{-/-}$ mice, climbing fiber paired pulse depression and halfwidth was significantly perturbed compared to *Atm*$^{Wt/Wt}$; *Aptx*$^{+/+}$ mice. Data in **B** were compared using an ANOVA (Kruskal-Wallis) followed by Dunn's multiple comparisons test while data in **D to F** were compared via Welch's *t*-test. Symbol/color key: *Atm*$^{Wt/Wt}$; *Aptx*$^{+/+}$ (purple circle), *Atm*$^{R35X/R35X}$; *Aptx*$^{-/-}$ (orange square) **Figure 4-figure supplement 1**

Figure 5. Cerebellar atrophy is associated with a progressive reduction in PN neural action potential firing frequency and PN dendritic length. A) Schematic diagram of extracellular recording

1336 from a single Purkinje neuron (PN) in an acute cerebellar tissue slice preparation. Example
1337 electrophysiological traces for *Atm*$^{Wt/Wt}$; *Aptx*$^{+/+}$ (purple, top) and *Atm*$^{R35X/R35X}$; *Aptx*$^{-/-}$ (orange, bottom) PNs
1338 in the medial (vermis) area of the cerebellum. **B)** *Atm*$^{R35X/R35X}$; *Aptx*$^{-/-}$ PN action potential firing frequency
1339 progressively decreased with age and was significantly slower in comparison to all control genotypes
1340 expressing at least one copy of the *Atm* or *Aptx* gene. [*Atm*$^{Wt/Wt}$; *Aptx*$^{+/+}$ (n=52 to 59), *Atm*$^{Wt/Wt}$; *Aptx*$^{-/-}$ (n
1341 = 51 to 64), *Atm*$^{R35X/R35X}$; *Aptx*$^{+/+}$ (n = 39 to 52), *Atm*$^{R35X/R35X}$; *Aptx*$^{-/-}$ (n = 24 to 71), *Atm*$^{Wt/R35X}$; *Aptx*$^{-/-}$ (n =
1342 69)] **C)** Cartoon image of the brain highlighting the dorsal forebrain and cerebellar surface. 2-dimensional
1343 area estimates from dorsal images of the brain were used to determine the cerebellum to forebrain ratio
1344 allowing us to control for any differences in overall size of the brain. We found the cerebellum decreased
1345 in size over age in *Atm*$^{R35X/R35X}$; *Aptx*$^{-/-}$(n = 5 to 10), but not control mice [*Atm*$^{Wt/Wt}$; *Aptx*$^{+/+}$ (n = 4 to 20),
1346 *Atm*$^{Wt/Wt}$; *Aptx*$^{-/-}$ (n = 4 to 12), *Atm*$^{R35X/R35X}$; *Aptx*$^{+/+}$ (n = 6 to 16), *Atm*$^{Wt/R35X}$; *Aptx*$^{-/-}$ (n = 6)]. **D)**
1347 Immunofluorescent images of *Atm*$^{Wt/Wt}$; *Aptx*$^{+/+}$ (top) and *Atm*$^{R35X/R35X}$; *Aptx*$^{-/-}$ (bottom) at P400 (medial
1348 cerebellar lobule VIII). Scale bar = 50 μm **E)** The width of the molecular layer, but not the granule cell
1349 layer progressively declined over age (n = 5 to 7). Statistical significances were assessed via 2-way
1350 ANOVA with age and genotype as factors followed by *posthoc* Holm-Sidak (**B**, **C**, and **E (top)**) or Sidak
1351 (**E bottom**) pairwise multiple comparisons test. **Figure 5-figure supplements 1-5, Figure 5-source data**

1352 **Figure 6. T-cell deficits are found in the blood of *Atm*$^{R35X/R35X}$; *Aptx*$^{-/-}$ mice. A)** Representative flow
1353 cytometric profiles of T-cell glycoprotein marker CD3 and summary plots indicate ATM and/or APTX
1354 deficient mice have decreased proportions of CD3^{+} T-cells in the blood. **B)** Representative flow cytometric
1355 profiles of T-cell glycoprotein markers CD4 and CD8 gated on CD3^{+} cells and summary plots for CD8
1356 and CD4 single positive cell proportions. ATM deficient mice had reduced CD4^{+} proportions compared
1357 to mice with at least one copy of the *Atm* gene. Statistical significances were assessed via 1-way ANOVA
1358 followed by *posthoc* Tukey's pairwise multiple comparisons tests. Number of animals denoted at bottom
1359 of bar. Symbol/color key: *Atm*$^{Wt/Wt}$; *Aptx*$^{+/+}$ (purple circle), *Atm*$^{R35X/R35X}$; *Aptx*$^{+/+}$ (green triangle), *Atm*$^{Wt/R35X}$;
1360 *Aptx*$^{-/-}$ (red inverted triangle), *Atm*$^{R35X/R35X}$; *Aptx*$^{-/-}$ (orange square) **Figure 6/7-source data**

1361 **Figure 7. ATM and APTX deficiency confer deficits in T-cell expression, but at different**
1362 **developmental stages. A)** Representative flow cytometric profiles of T-cell glycoprotein markers CD44
1363 and CD25 gated on $CD4^{-}CD8^{-}$ double negative (DN) cells. Summary plots show proportions of
1364 thymocytes at DN stages 1-4 (left to right). APTX deficient mice display increased proportions for DN1-3
1365 and decreased proportion at DN4 consistent with a deficit in ontogeny from DN3 to DN4. **B)**
1366 Representative flow cytometric profiles of T-cell glycoprotein markers CD4 and CD8 gated. ATM deficient
1367 mice display decreased proportions for CD4 and CD8 single positive cells consistent with a deficit in
1368 ontogeny from $CD4^{+}CD8^{+}$ double positive to $CD4^{+}$ and $CD8^{+}$ single positive fates. Statistical significances
1369 were assessed via 1-way ANOVA followed by *posthoc* Tukey's pairwise multiple comparisons tests.
1370 Number of animals denoted at bottom of bars. Symbol/color key: $Atm^{Wt/Wt}$; $Aptx^{+/+}$ (purple circle),
1371 $Atm^{R35X/R35X}$; $Aptx^{+/+}$ (green triangle), $Atm^{Wt/R35X}$; $Aptx^{-/-}$ (red inverted triangle), $Atm^{R35X/R35X}$; $Aptx^{-/-}$ (orange
1372 square)

1373 **Figure 8. ATM protein expression is restored after readthrough compound exposure in explant**
1374 **tissues from $Atm^{R35X/R35X}$ and $Atm^{Q35X/Q35X}$.** Spleen and cerebellar explant tissue from $Atm^{R35X/R35X}$ and
1375 $Atm^{Wt/Wt}$ mice were treated with vehicle, the readthrough compounds G418 (100 μM), or GJ103 (100
1376 μM) for 72 hrs. ATM immunoblots show recovery of ATM (MW 350 kDa) production in both the spleen (n
1377 = 2) and cerebellum (n = 3). Equal loading was assessed via housekeeping genes (Actin or GAPDH)
1378 and ponceau staining. **Figure 8-source data**

9.0 Figures

Fig. 1

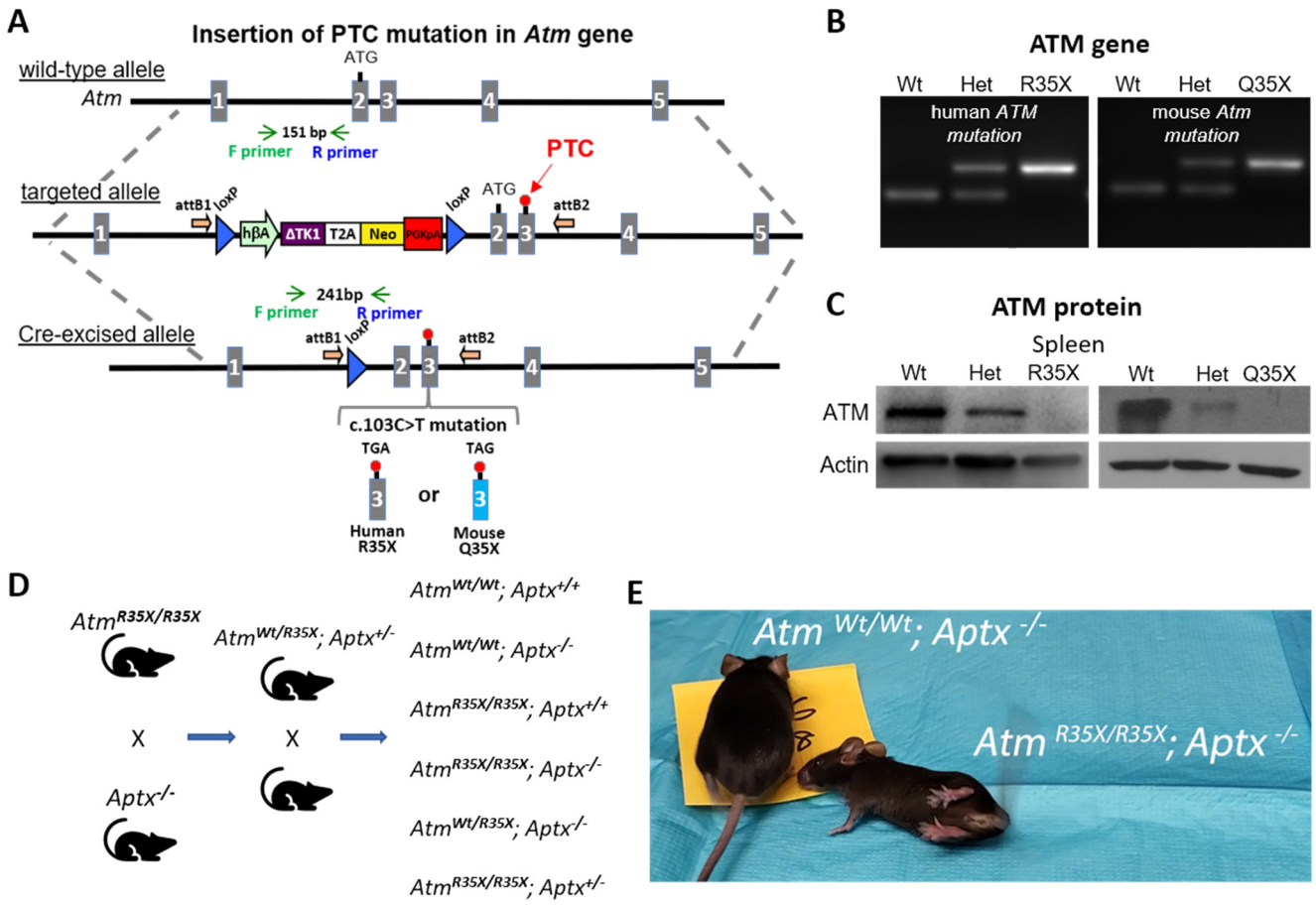

Fig. 2

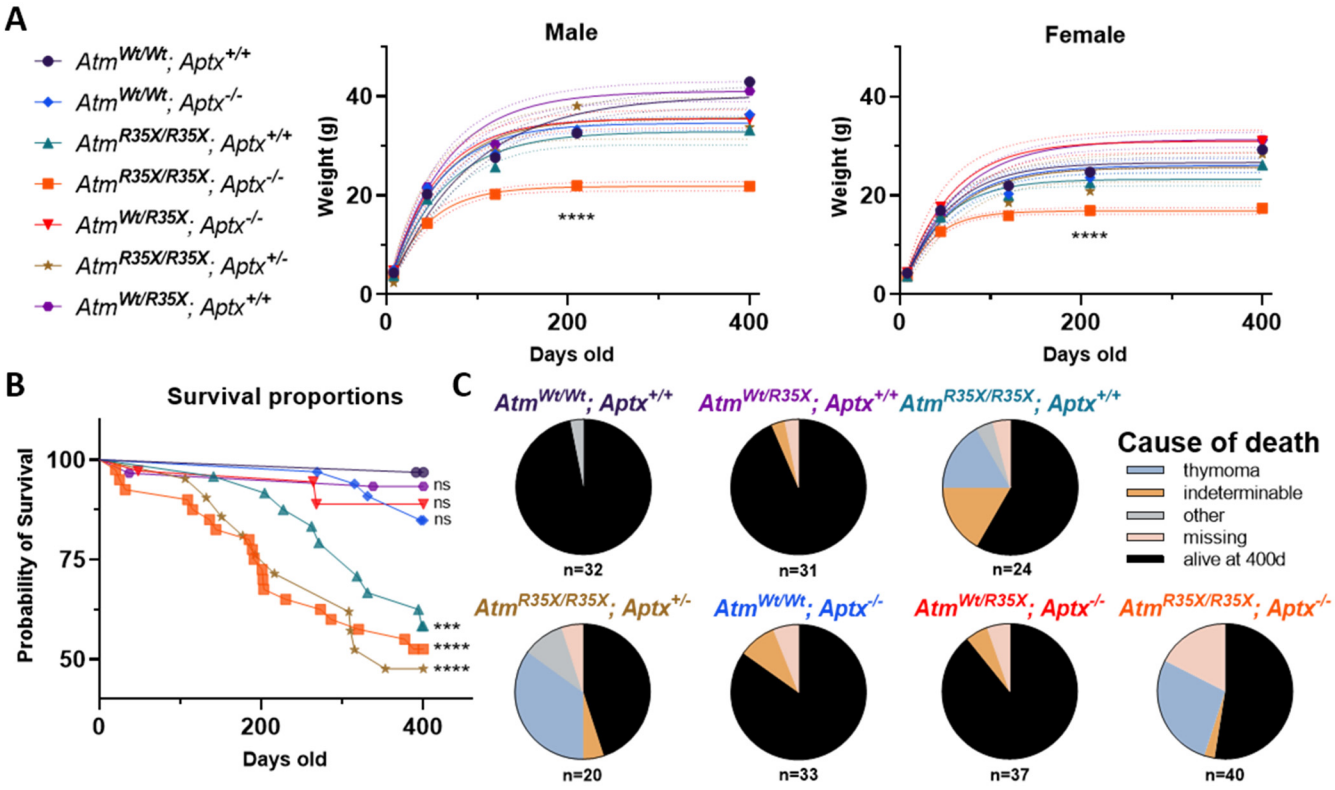
A
Atm Wt/Wt; Aptx +/+
Atm Wt/Wt; Aptx -/-
Atm R35X/R35X; Aptx +/+
Atm R35X/R35X; Aptx -/-
Atm Wt/R35X; Aptx -/-
Atm R35X/R35X; Aptx +/-
Atm Wt/R35X; Aptx +/+
Male
Female
Weight (g)
Days old
****
B
Survival proportions
Probability of Survival
ns
***
C
Cause of death
thymoma
indeterminable
other
missing
alive at 400d
n=32
n=31
n=24
n=20
n=33
n=37
n=40

Fig. 3

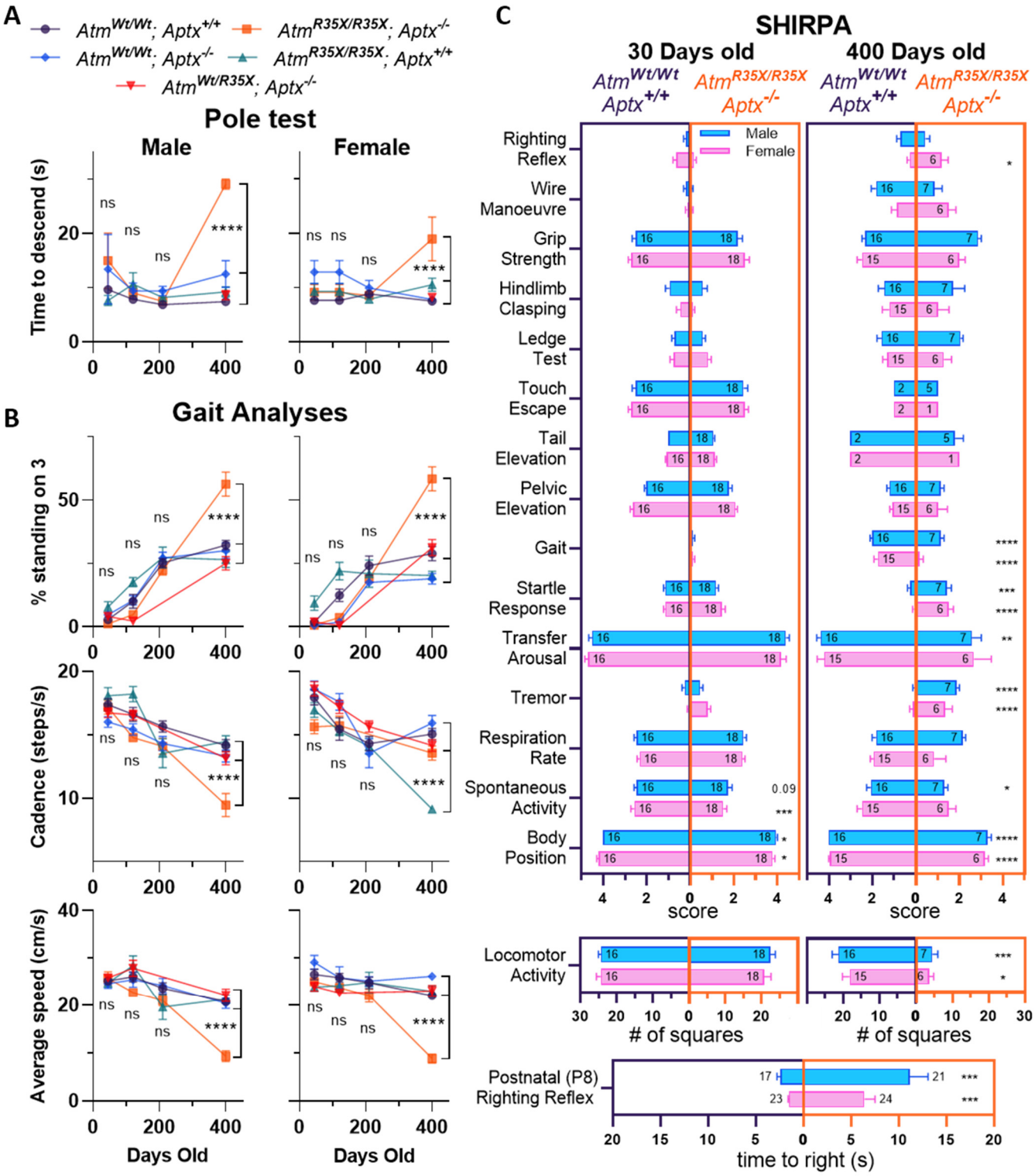

1384

1385

Fig. 4

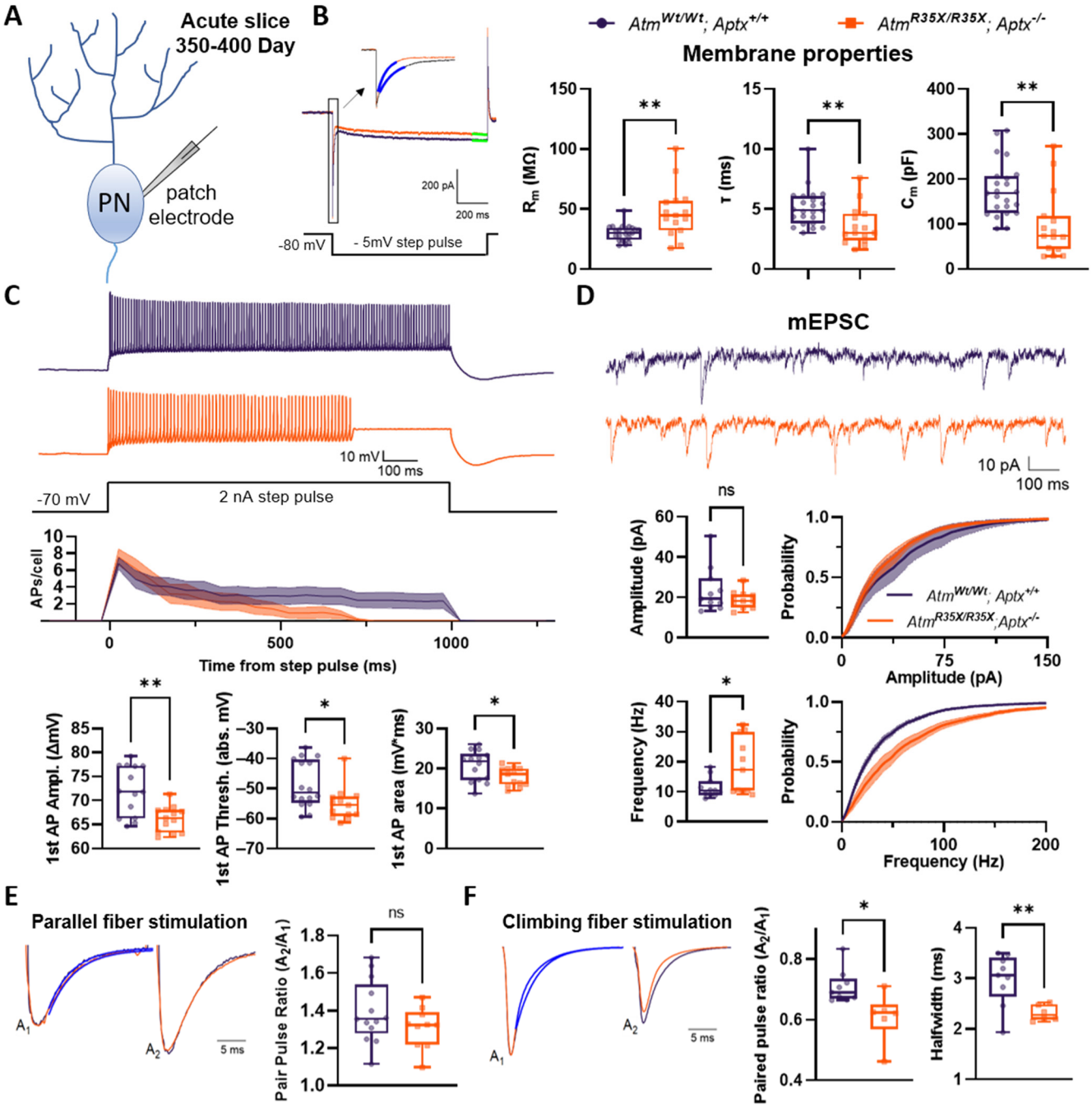

1386

1387

Fig. 5

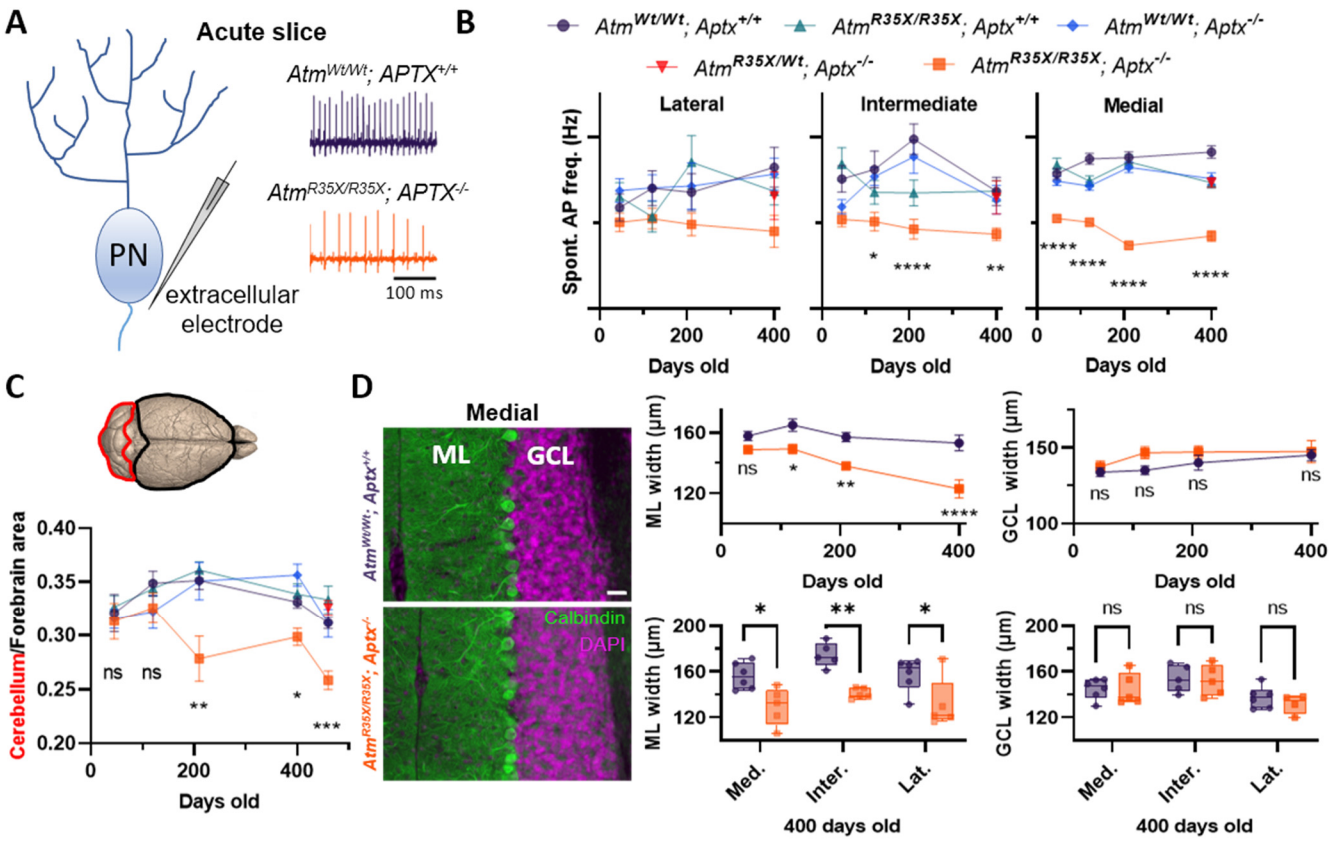
A
Acute slice
PN
extracellular electrode
Atm^Wt/Wt; APTX^+/+
Atm^R35X/R35X; APTX^-/-
100 ms
B
Atm^Wt/Wt; Aptx^+/+
Atm^R35X/R35X; Aptx^+/+
Atm^Wt/Wt; Aptx^-/-
Atm^R35X/Wt; Aptx^-/-
Atm^R35X/R35X; Aptx^-/-
Lateral
Intermediate
Medial
Spont. AP freq. (Hz)
Days old
C
Cerebellum/Forebrain area
Days old
D
Medial
ML
GCL
Calbindin
DAPI
ML width (µm)
GCL width (µm)
Days old
Med.
Inter.
Lat.
400 days old

1388

Fig. 6

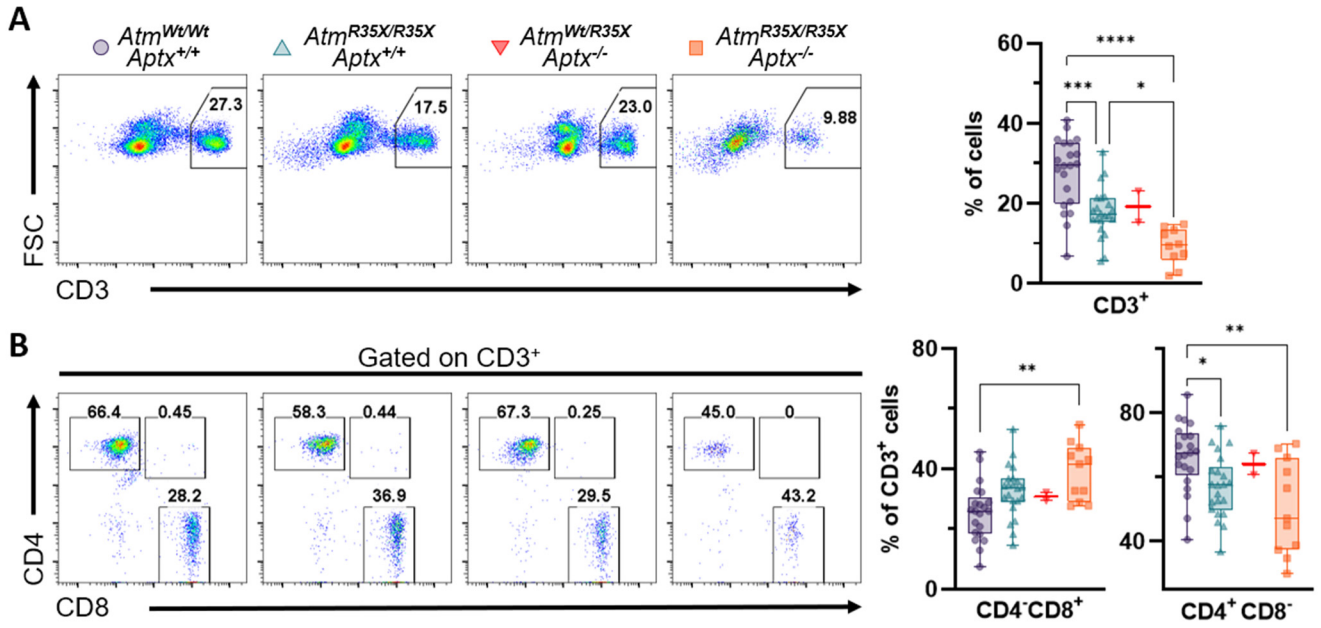
A
Atm Wt/Wt Aptx +/+
Atm R35X/R35X Aptx +/+
Atm Wt/R35X Aptx -/-
Atm R35X/R35X Aptx -/-
27.3
17.5
23.0
9.88
FSC
CD3
% of cells
CD3+
B
Gated on CD3+
66.4
0.45
28.2
58.3
0.44
36.9
67.3
0.25
29.5
45.0
0
43.2
CD4
CD8
% of CD3+ cells
CD4-CD8+
CD4+ CD8-

1389

Fig. 7

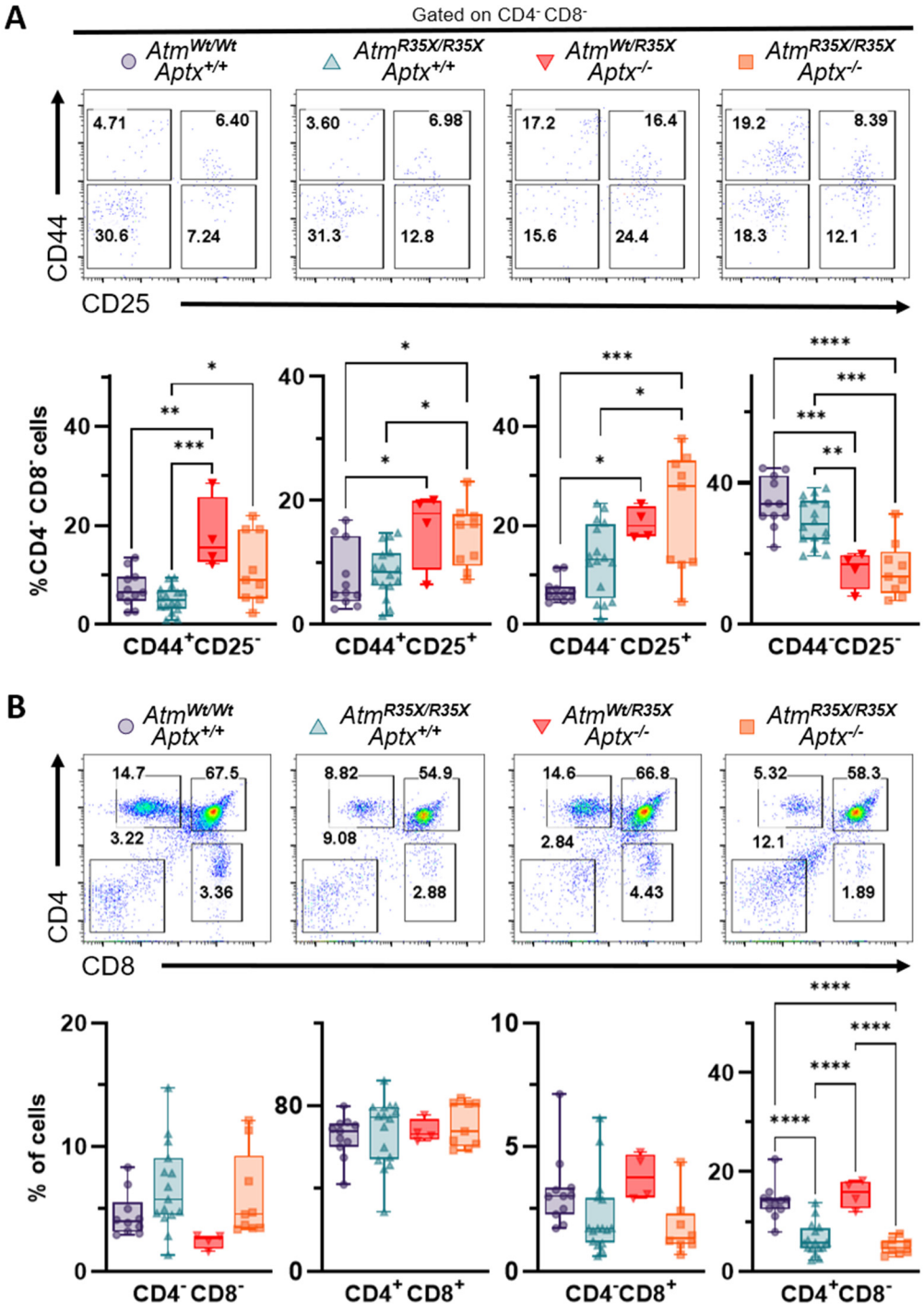

1390

1391

Fig. 8

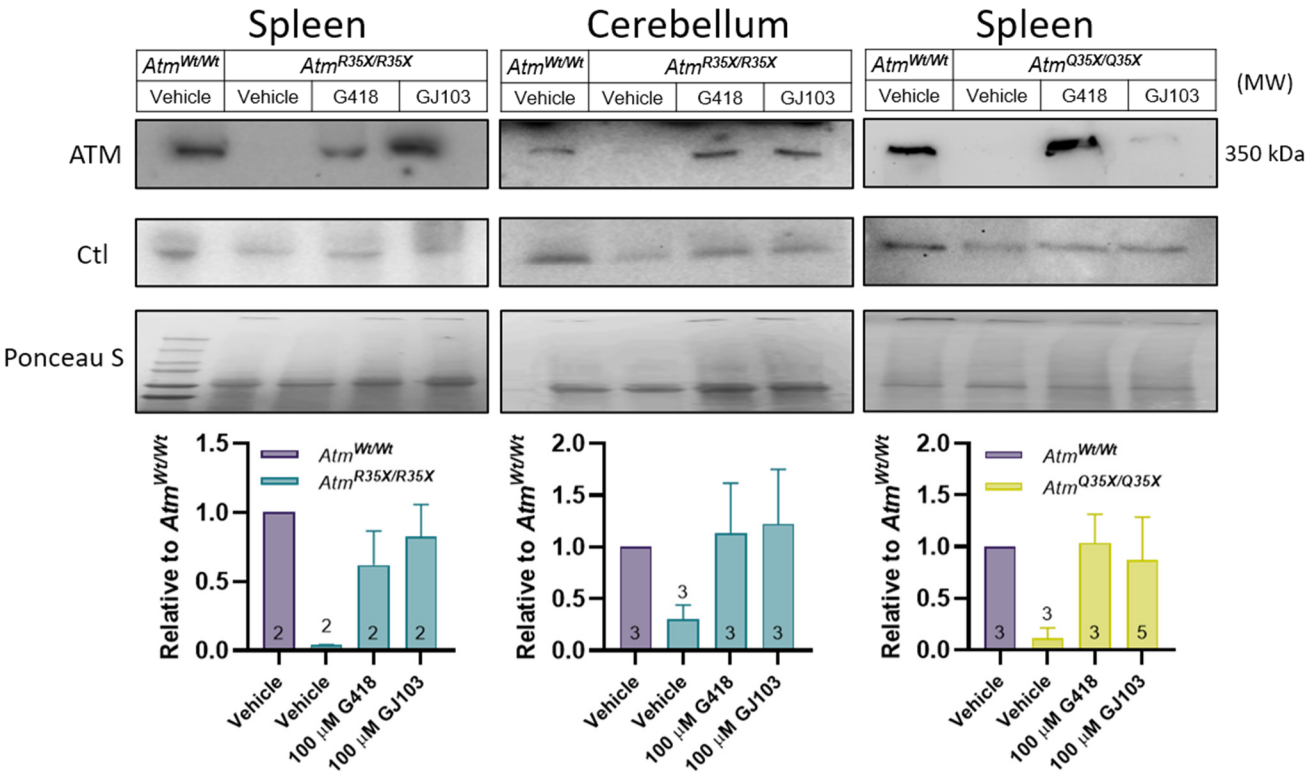
Spleen
Cerebellum
Spleen
Atm Wt/Wt
Atm R35X/R35X
Atm Q35X/Q35X
Vehicle
Vehicle
G418
GJ103
(MW)
ATM
350 kDa
Ctl
Ponceau S
Relative to Atm Wt/Wt
Atm Wt/Wt
Atm R35X/R35X
Atm Q35X/Q35X
Vehicle
Vehicle
100 μM G418
100 μM GJ103

1392

10.0 Figure Supplements

Figure 2-figure supplement 1

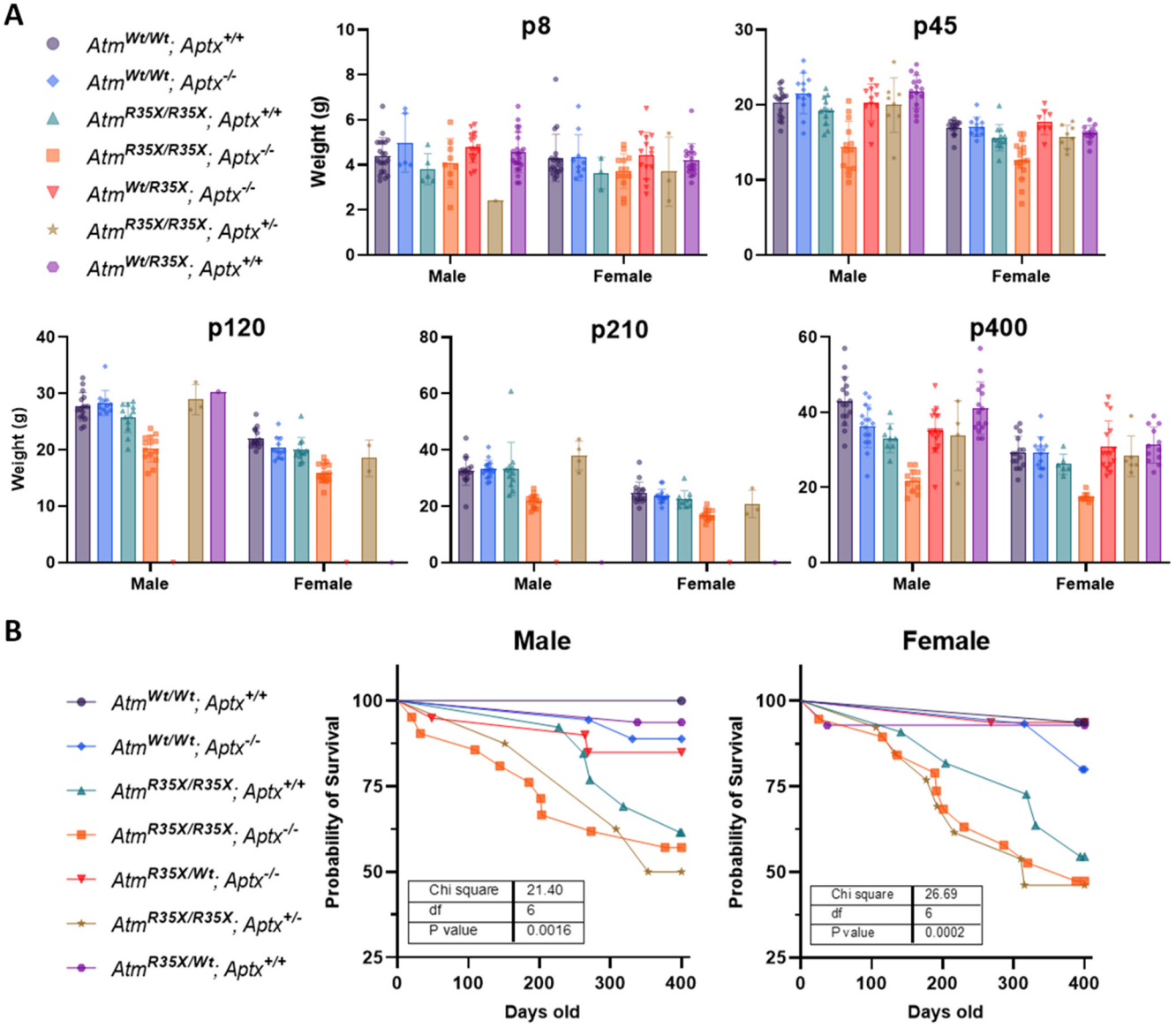

Figure 1-figure supplement 1. Animal weight for each time point and genotype. A) The average weights are plotted for each genotype at each of the indicated time points. Growth curves without experimental, 2-way ANOVA with age and genotype as factors. Male: $F_{(10, 226)}= 5.6$, $p<0.0001$; Female: $F_{(10, 197)}= 7.3$, $p<0.0001$. **B)** The survivability of each genotype of mice are plotted for male and female individually.

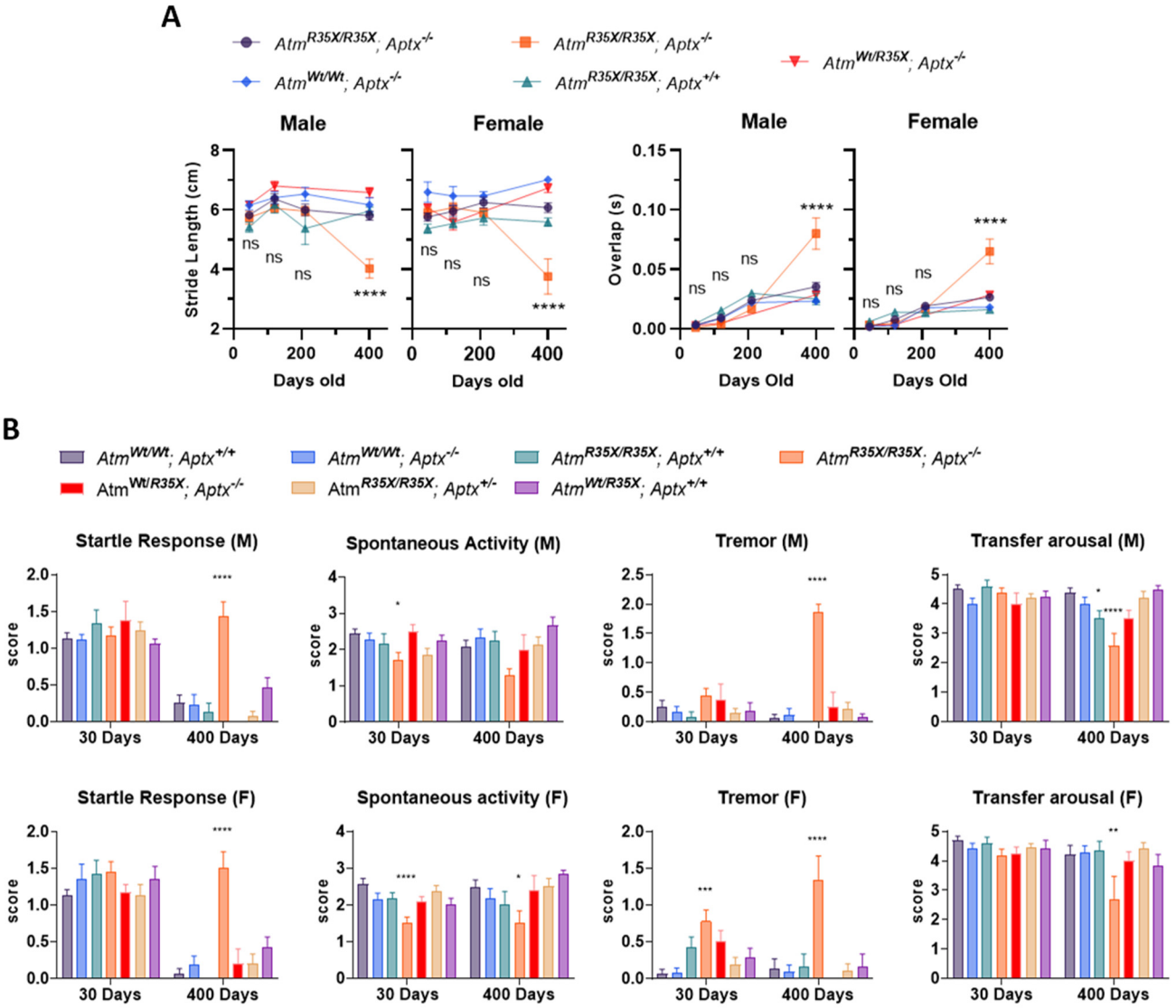

Figure 3-figure supplement 1. *Atm*$^{R35X/R35X}$; *Aptx*$^{-/-}$ mice develop progressive ataxia. A) *Atm*$^{R35X/R35X}$; *Aptx*$^{-/-}$ mice develop an ataxia that at late stages results in a severe loss of coordination and ability to ambulate. **B)** Additional gait analyses measuring stride length and time of overlap of the hindlimbs. Examined via two-way ANOVA with age and genotype as factors followed by *potshot* Tukey's multiple comparison tests between *Atm*$^{R35X/R35X}$; *Aptx*$^{-/-}$ and each of the control genotypes. **C)** Behavioral deficits are seen only in *Atm*$^{R35X/R35X}$; *Aptx*$^{-/-}$ mice across all behavioral tests and sexes. Behavioral tests were examined using a non-parametric Kruskal Wallace followed by *posthoc* Dunn's multiple comparisons tests.

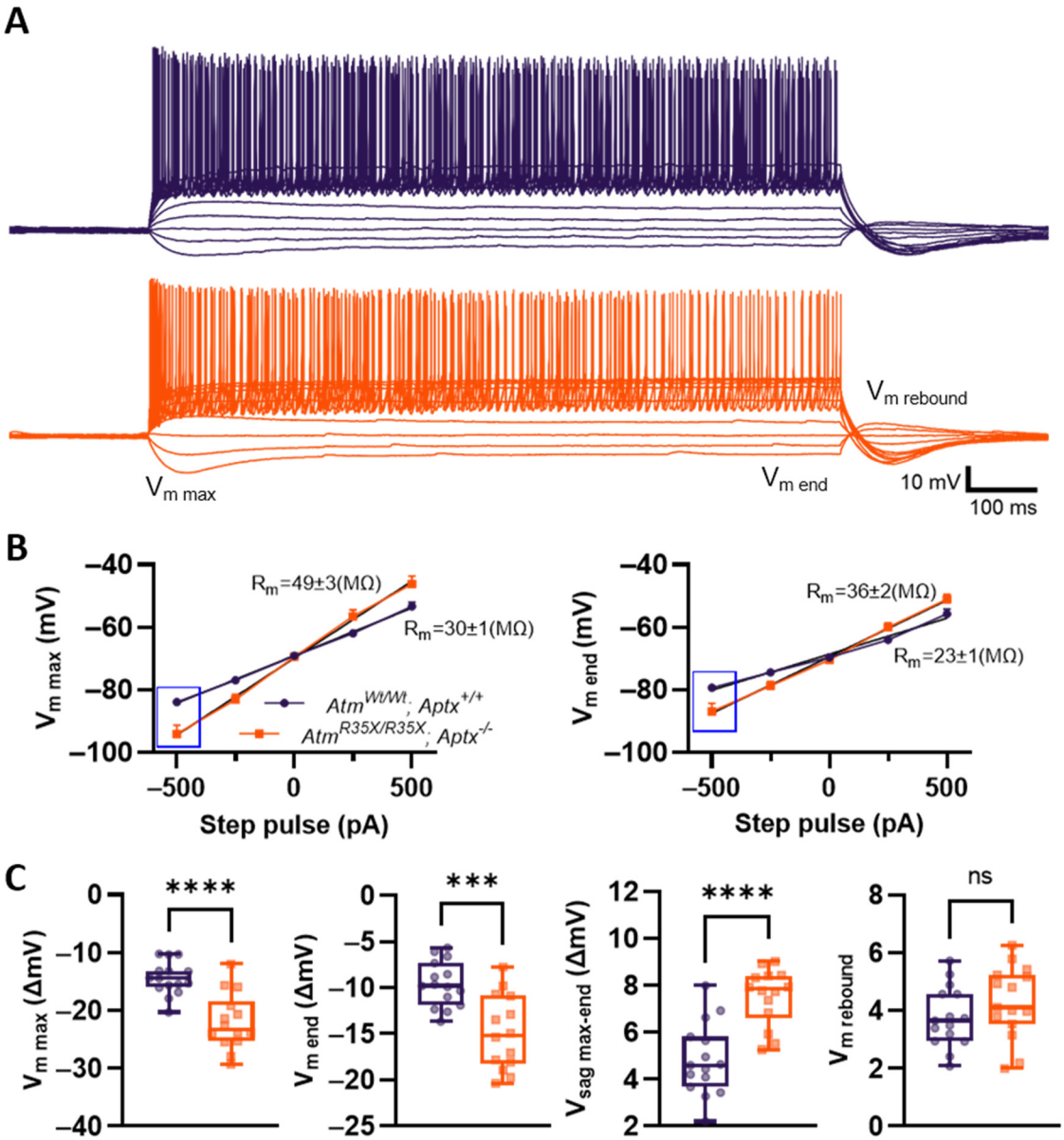

Figure 4-figure supplement 1. Current *vs.* voltage responses significantly differ between *Atm*$^{Wt/Wt}$; *Aptx*$^{+/+}$ and *Atm*$^{R35X/R35X}$; *Aptx*$^{-/-}$ mice. A) PN voltage responses to various current steps between -500 and 2250 pA (250 pA steps) from a -70 mV holding current in *Atm*$^{Wt/Wt}$; *Aptx*$^{+/+}$ (top, purple) and *Atm*$^{R35X/R35X}$; *Aptx*$^{-/-}$ (bottom, orange) mice. **(B)** I–V curves calculated from either max deflection ($V_{m\ max}$) or steady state ($V_{m\ end}$) for *Atm*$^{Wt/Wt}$; *Aptx*$^{+/+}$ (purple) and *Atm*$^{R35X/R35X}$; *Aptx*$^{-/-}$ (orange) mice. **C)** Various measurements of the voltage response to -500 pA step pulse (blue box in **B**) in *Atm*$^{Wt/Wt}$; *Aptx*$^{+/+}$ (purple) and *Atm*$^{R35X/R35X}$; *Aptx*$^{-/-}$ (orange) mice. Significance was tested using a non-parametric Mann Whitney test.

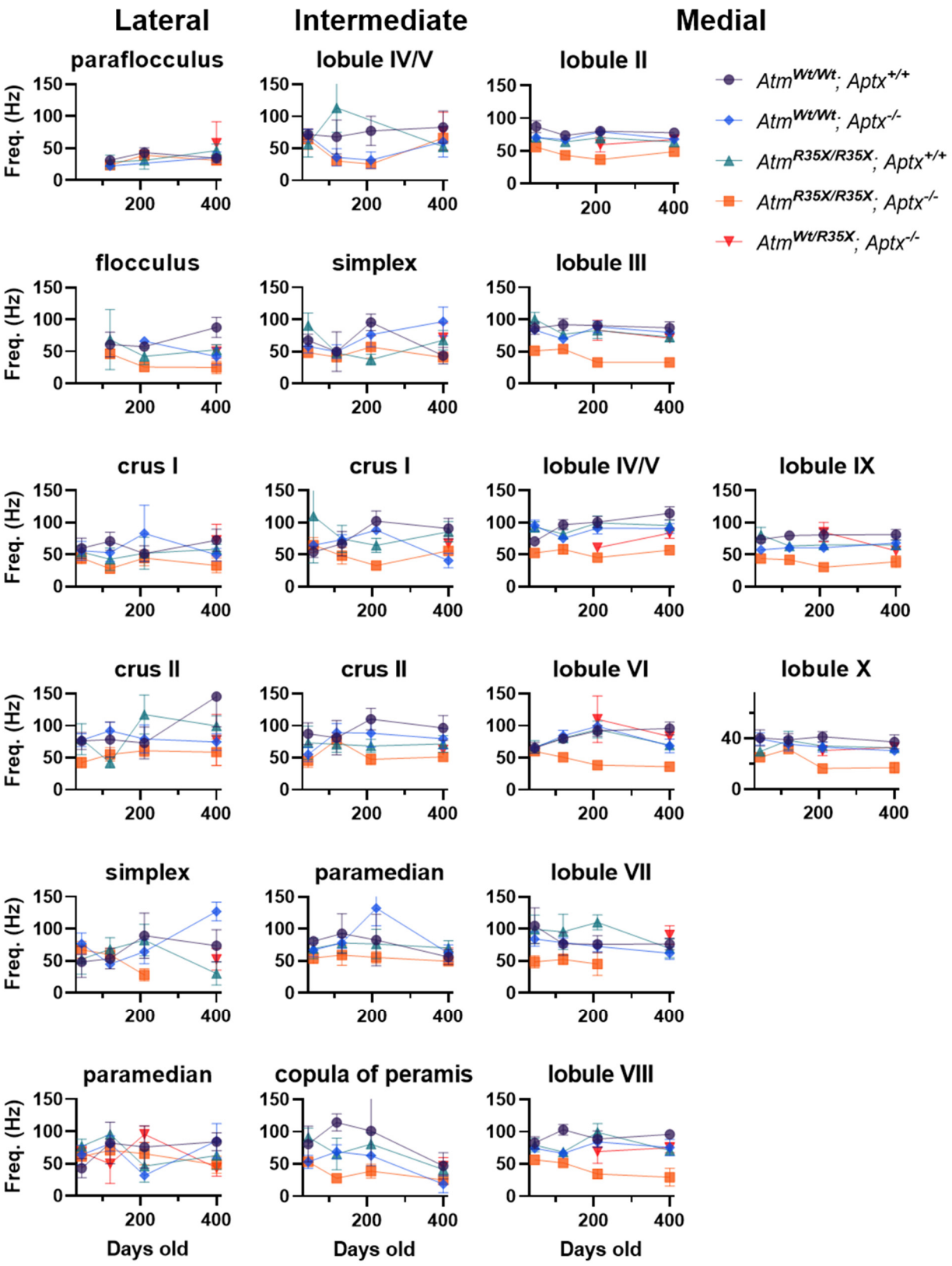

Figure 5-figure supplement 1. Mean variation between PN firing intervals across the cerebellum. Average CV2 of PN firing frequency is plotted across the indicated locations at P45, 120, 210, and 400.

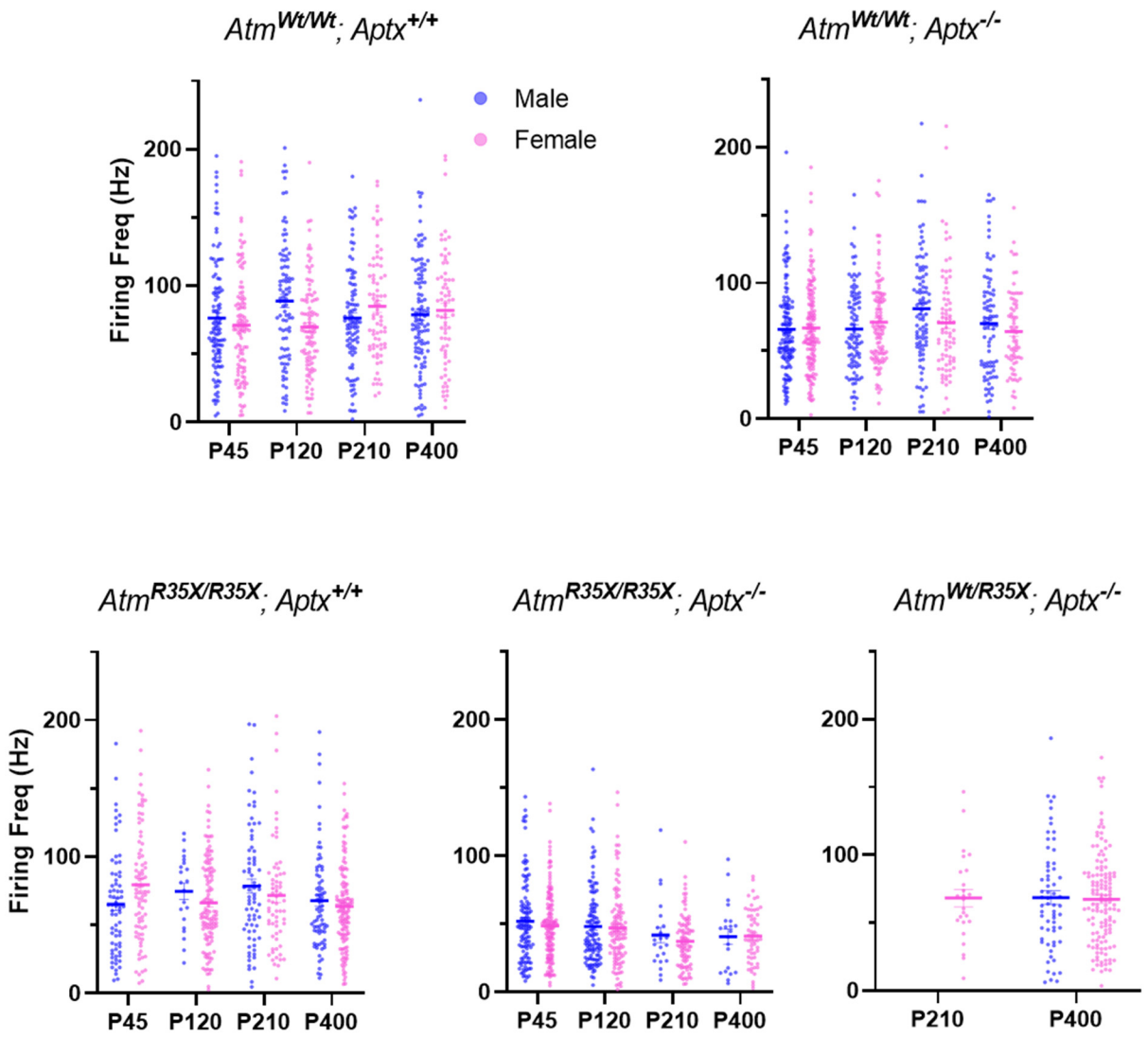

1424

1425 **Figure 5-figure supplement 2. Mean PN firing frequency across genotype and sex.** Average PN
1426 firing frequency for all cells recorded from male and female mice is plotted for the indicated genotype. No
1427 significant differences were observed between sex. 2-Way ANOVA with age and sex as factors, *Atm*$^{Wt/Wt}$*;*
1428 *Aptx*$^{+/+}$ ($F_{(1, 751)} = 1.15$, p=0.3), *Atm*$^{Wt/Wt}$*; Aptx*$^{-/-}$ ($F_{(1, 797)} = 1.10$, p=0.3), *Atm*$^{R35X/R35X}$*; Aptx*$^{+/+}$ ($F_{(1, 630)} = 0.17$,
1429 p=0.7), *Atm*$^{R35X/R35X}$*; Aptx*$^{-/-}$ ($F_{(1, 666)} = 1.10$, p=0.4), *t*-test for P400 *Atm*$^{Wt/R35X}$*; Aptx*$^{-/-}$ (p=0.9)

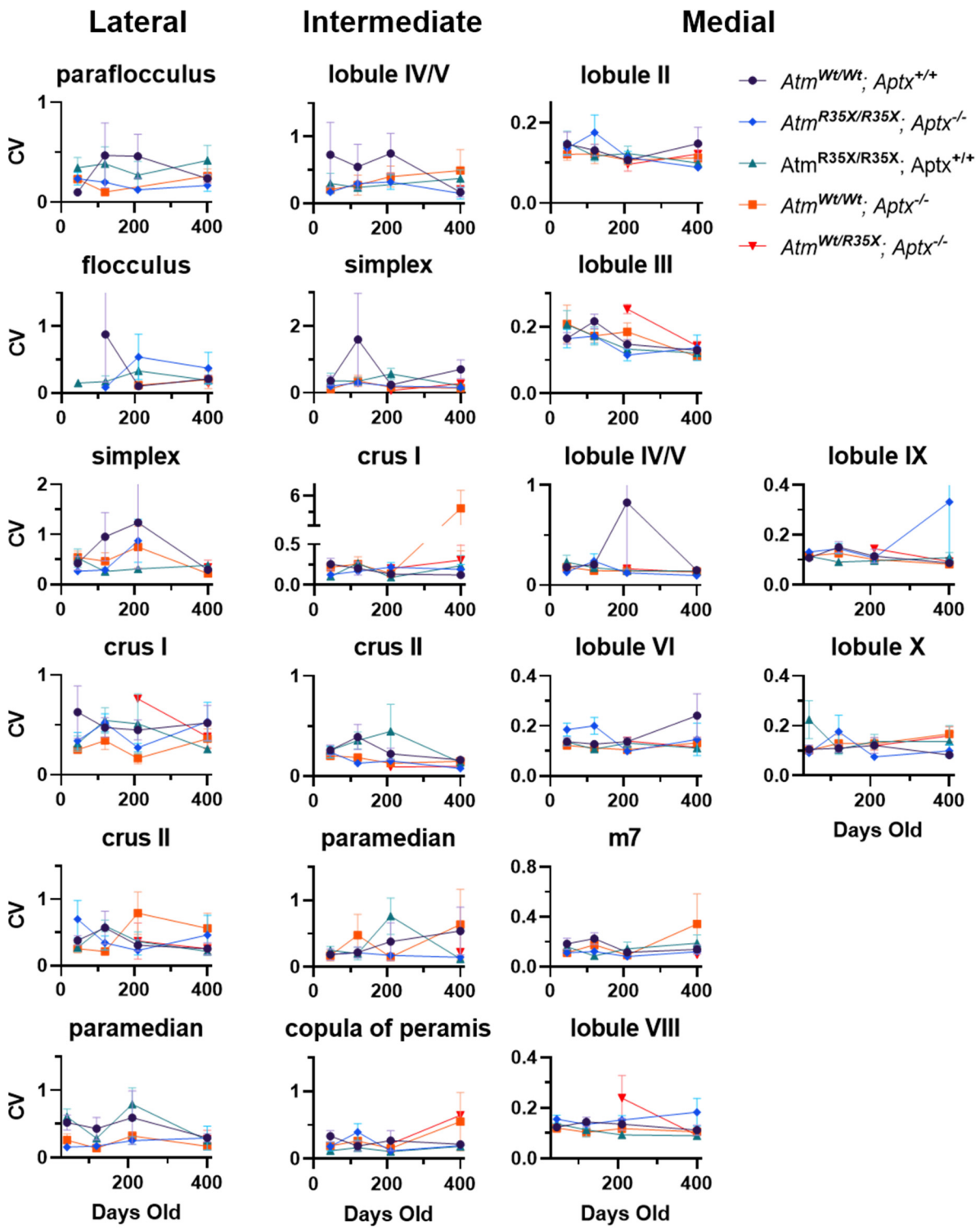

Figure 5-figure supplement 3. Coefficient of Variation of PN firing frequency across the cerebellum. Average CV of PN firing frequency is plotted across the indicated locations at P45, 120, 210, and 400. No significant differences ($p<0.5$) were detected across all areas using 2-way ANOVA with age and genotype as factors.

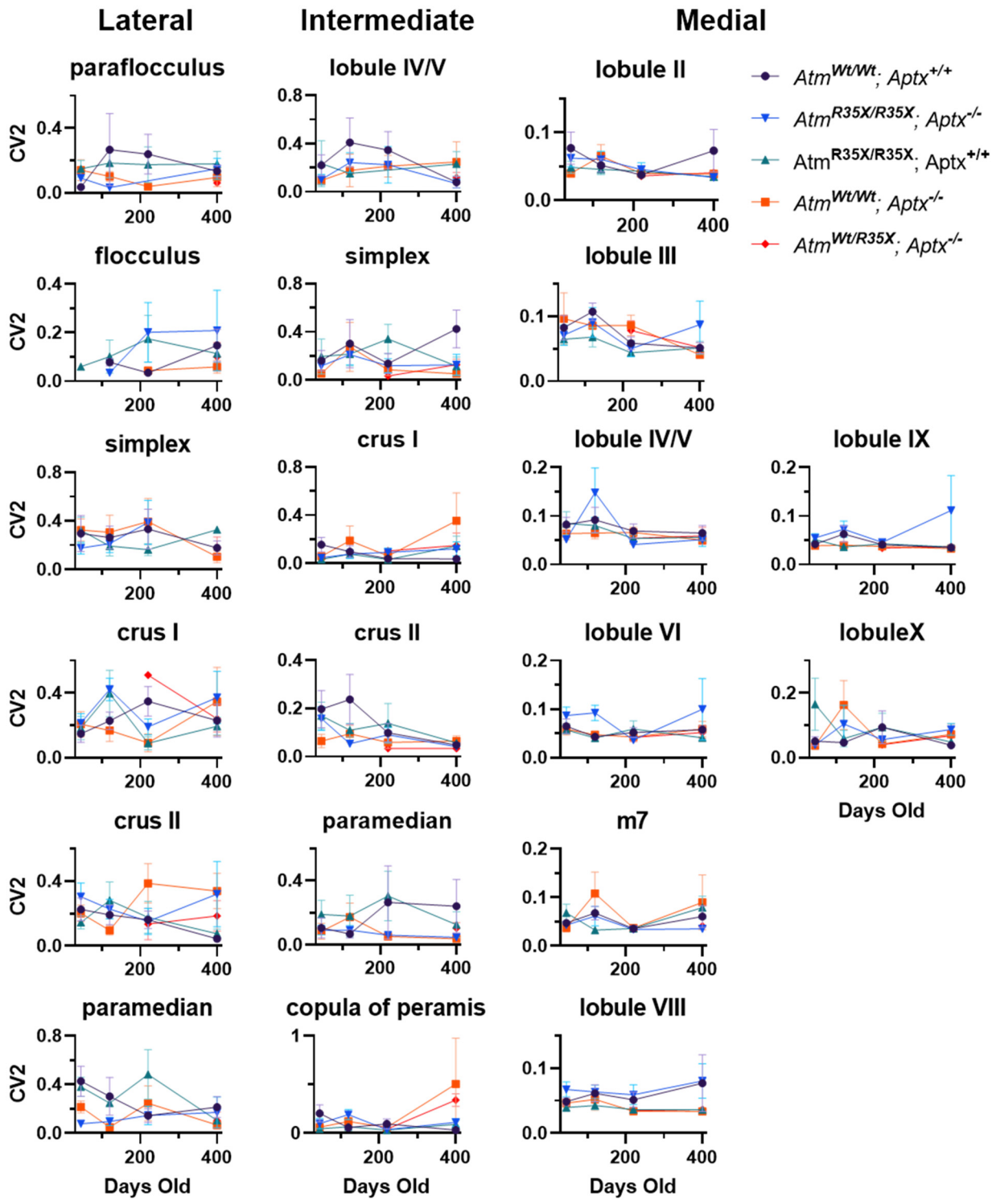

Figure 5-figure supplement 4. Mean variation between PN firing intervals across the cerebellum. Average CV2 of PN firing frequency is plotted across the indicated locations at P45, 120, 210, and 400. No significant differences ($p<0.5$) were detected across all areas using 2-way ANOVA with age and genotype as factors.

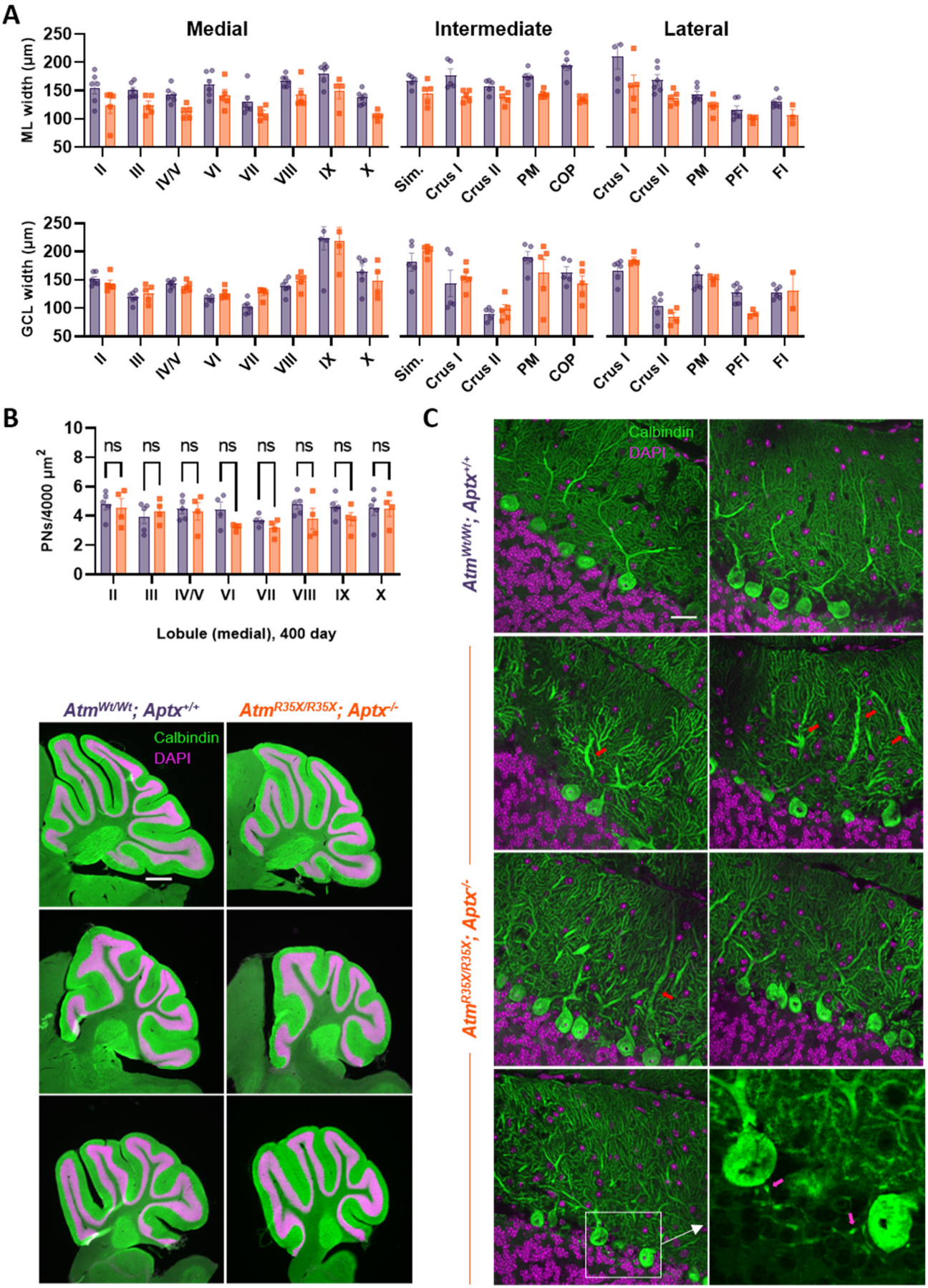
A
Medial
Intermediate
Lateral
ML width (µm)
GCL width (µm)
250
200
150
100
50
II
III
IV/V
VI
VII
VIII
IX
X
Sim.
Crus I
Crus II
PM
COP
PFl
Fl
B
PNs/4000 µm²
ns
Lobule (medial), 400 day
C
Calbindin
DAPI
Atm^Wt/Wt; Aptx^+/+
Atm^R35X/R35X; Aptx^-/-

1441 **Figure 5-figure supplement 5. Histopathological effects of ATM and ATPX deficiency. A)** Width
1442 measurements of the molecular and granule cell layer (ML and GCL respectively) for each folia across
1443 the medial intermediate and lateral areas of the cerebellum. **B) (Top)** Summary plot indicates no
1444 significant differences in the 2D linear density of PNs across each folia in *Atm*$^{R35X/R35X}$*; Aptx*$^{-/-}$ *vs. Atm*$^{Wt/Wt}$*;*
1445 *Aptx*$^{+/+}$. **(Bottom)** Images of parasagittal cerebellar slices (2.5X) illustrating the lack of significant gaps in
1446 PN (green, Calbindin) or granule cell layers (magenta, DAPI). Scale bar = 0.5 mm **(C)** Images of
1447 parasagittal sections from *Atm*$^{Wt/Wt}$*; Aptx*$^{+/+}$ (top row) and *Atm*$^{R35X/R35X}$*; Aptx*$^{-/-}$ (bottom rows) mice (63X).
1448 PNs (green, Calbindin) were found to have a larger diameter than those found in *Atm*$^{Wt/Wt}$*; Aptx*$^{+/+}$ cells
1449 (red arrows). PN axonal swellings were also observed in *Atm*$^{R35X/R35X}$*; Aptx*$^{-/-}$ sections (magenta arrows).
1450 Scale bar = 50 μm

1451 11.0 Source files

1452 **Figure 2- source data. Weight, age of death, and probable cause of death**

1453 **Figure 3-source data. Raw behavior data**

1454 **Figure 4-source data. Electrophysiological data**

1455 **Figure 5- source data. Individual average firing frequencies for each recorded cell; Individual CV**
1456 **for each recorded cell; Brain area**

1457 **Figure 6/7- source data. Tables of FACs data**

1458 **Figure 8-source data. Western blot measurements**

1459 12.0 Rich Media

1460 **Video S1. Pole test, *Atm*$^{Wt/Wt}$ *vs. Atm*$^{R35X/R35X}$.** *Atm*$^{R35X/R35X}$ do not display an ataxic phenotype at
1461 P460.

1462 **Video S2. Pole test, *Aptx*$^{+/+}$ *vs. Aptx*$^{-/-}$.** *Aptx*$^{-/-}$ mice do not display an ataxic phenotype at P460.

1463 **Video S3. Pole test, *Atm*$^{Wt/Wt}$*; Aptx*$^{+/+}$ *vs. Atm*$^{R35X/R35X}$*; Aptx*$^{-/-}$.** *Atm*$^{R35X/R35X}$*; Aptx*$^{-/-}$ have considerable
1464 motor disability at P460.

1465 **Video S4. Open field, *Atm*$^{Wt/Wt}$*; Aptx*$^{+/+}$ *vs. Atm*$^{R35X/R35X}$*; Aptx*$^{-/-}$.** *Atm*$^{R35X/R35X}$*; Aptx*$^{-/-}$ display a clear
1466 inability to ambulate in the open field at P460.

1467

1468

1469

1470